CORRELATION OF SHORT-TERM TO LONG-TERM OXIDATION TESTING FOR ALUMINA FORMING ALLOYS AND COATINGS

by

Matthew J. Stiger

BS, University of Pittsburgh, 1997

Submitted to the Graduate Faculty of

School of Engineering in partial fulfillment

of the requirements for the degree of

Doctor of Philosophy

University of Pittsburgh

2004

UNIVERSITY OF PITTSBURGH

SCHOOL OF ENGINEERING

This dissertation was presented

by

Matthew J. Stiger

It was defended on

June 8, 2004

and approved by

J. L. Beuth, Professor, Mechanical Engineering Department, Carnegie Mellon University

J. R. Blachère, Associate Professor Emeritus, Materials Science and Engineering Department

I. Nettleship, Professor, Materials Science and Engineering Department

Dissertation Director: G. H. Meier, Professor, Materials Science and Engineering Department

Dissertation Director: F. S. Pettit, Professor, Materials Science and Engineering Department

CORRELATION OF SHORT-TERM TO LONG-TERM OXIDATION TESTING FOR ALUMINA FORMING ALLOYS AND COATINGS

Matthew J. Stiger, PhD

University of Pittsburgh, 2004

Engineering long cyclic oxidation life of high temperature materials requires success on two fronts. First a slow growing protective oxide scale must form during the elevated temperature exposure. To satisfy this aspect, alumina-forming alloys and coatings are widely accepted as leading materials for use in this environment and are the focus of this discussion. The second aspect is the formation of an adherent oxide that resists spallation during thermal cycling. The driving force for spallation is the stored elastic strain energy that develops from stresses in the oxide scale. Once this stored elastic strain energy exceeds the oxide-substrate interfacial toughness, cracking and subsequent spallation occurs followed by rapid oxidation of the substrate. With advances in alloy and coating development resulting in higher operating temperatures and increased service lives, researchers are faced with excessive laboratory time and cost required to perform a long-term cyclic oxidation test.

The challenge is to predict long-term oxidation behavior from short-term experiments. Since the rate limiting step to high temperature oxidation is a thermally activated process, previous investigations were performed at increased exposure temperatures for rapid degradation of the alloys and coatings to rank material performance. Others have mechanically induced oxide spallation to give insight on the adherence of oxide scales prior to spontaneous failure. In this

investigation, short-term testing is employed to gain insight on long-term performance and to determine inputs into a cyclic oxidation model for life-time prediction.

This model operates in an iterative process where one iteration is a thermal cycle. The amount of oxide formed during the high temperature segment is calculated followed by the amount that is lost due to scale spallation during cooling. Retained oxide at the end of this cycle is used as the starting point for the following iteration. The two inputs into this model are the oxide scale growth and spallation behavior. Scale growth behavior corresponds to the isothermal growth kinetics that are experimentally determined by thermogravimetric analysis. Oxide scale spallation behavior is quantified by two short-term experiments of a novel acoustic emission experiment during a 24 hour exposure and the stress measurement of the scale after an exposure to the temperature of interest. Results from these short-term tests and modeled cyclic oxidation are compared to life-times from long-term cyclic oxidation tests.

TABLE OF CONTENTS

LIST OF TABLES

LIST OF FIGURES

PREFACE

This research was made possible with the financial support provided by the National Science Foundation and the United States Department of Energy. Additionally, I would like to acknowledge the Howmet Corporation for donating N5 nickel-base superalloy and aluminide coatings and Pratt & Whitney for donating PWA 1484 nickel-base superalloy.

This research could not have been possible without the support and assistance from a number of individuals. I would like to express my gratitude to the members of my thesis committee, Profs. J. Beuth, I. Nettleship and J. Blachere for their time and involvement and the technical staff at the Materials Science and Engineering Department at the University of Pittsburgh particularly G. M. McManus and A. Stewart for sharing their expertise. I would like to thank all of the members of the High Temperature Group I have worked with during my attendance at the university, particularly M. Maris-Jakubowski for all her help with cyclic oxidation testing and E. Hewitt for his proficiency in experimental design. I would especially like to express my heartfelt thanks to my thesis advisors Prof. F. S. Pettit and Prof. G. H. Meier for their advice, their guidance and the freedom to pursue this project. It was an honor to learn from and work with great pioneers in the field of high temperature oxidation.

Finally, I must thank my parents, Joseph and Regina, and the rest of my family for all the support they have provided, but my deepest appreciation goes to my wonderful wife, Susan. With her support, encouragement and sacrifices, I was able to pursue and complete this challenge. For this, I am forever indebted to her.

1.0 INTRODUCTION

Since the advent of the gas turbine engine, superalloys have been the material of choice for such a demanding application. Their designed high temperature strength and resistance to oxidation are required properties for use in these extreme conditions. Development of new engines and materials are driven by the desire to increase the operating temperatures for the increase in engine performance and efficiency. Progress in alloy development over the past 50 years has increased alloy operating temperature by 200°C, see Figure 1[1]. This increases a conflict of interest between the two requirements of the superalloy. High temperature strength is generally optimized at the expense of resistance to environmental attack in an environment where greater oxidation resistance is mandatory.

These alloys and coatings resist oxidation by the formation and maintenance of an oxide layer. This oxide layer is the product of the reaction of the metal and the oxygen in the gas. The oxide layer scale should be adherent to the metal and form a protective barrier that separates the reactants from further reaction and alloy consumption. Scale adherence and durability are issues that need to be maximized for the optimum performance. If the scale has poor adherence, evaporates at a high rate or continues to crack, the underlying metal can be exposed to further rapid oxidation. It is also the alloy's ability to reform this scale in the event of scale spallation that determines the life of a component.

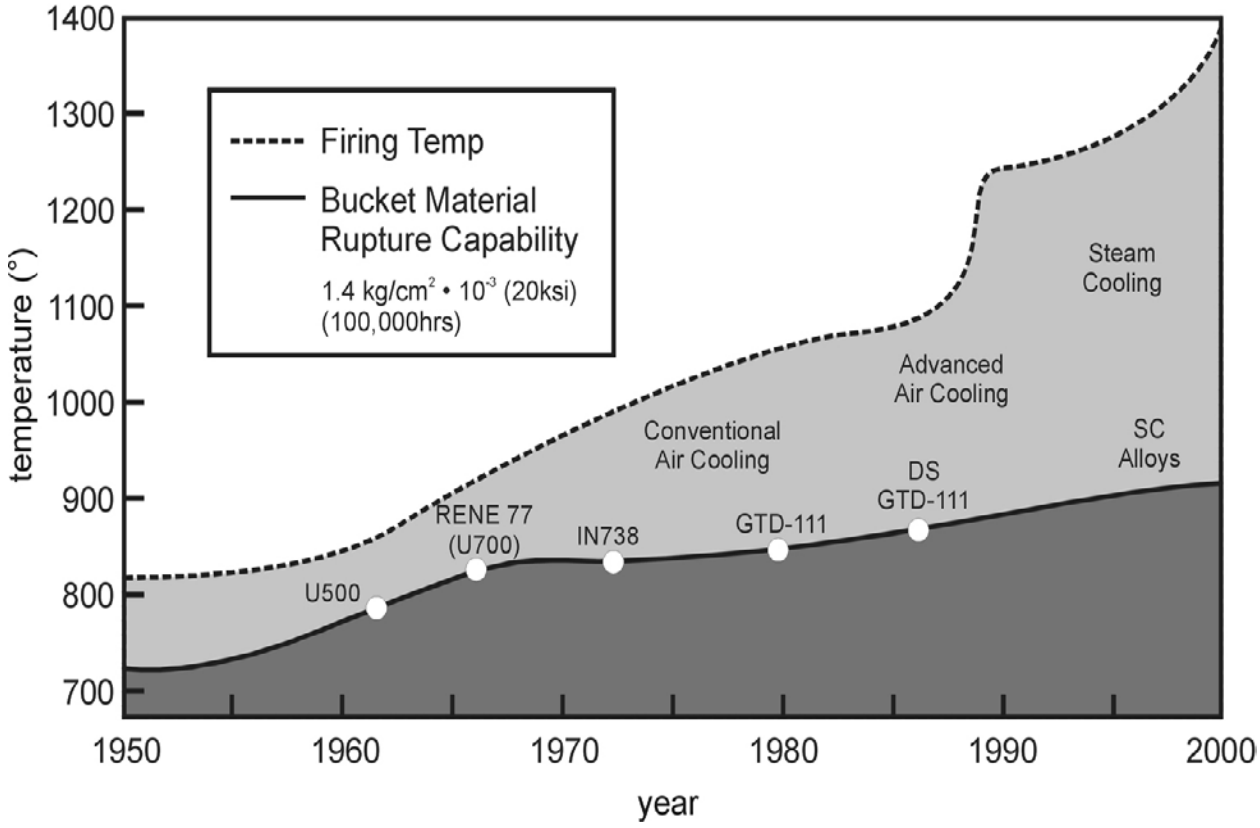

Figure 1. A plot of the increase in operating temperature of superalloys over the past 50 years.

Testing of modern superalloys and coatings to rank their performance brings about an interesting challenge. As material performance increases, so do the service lives which approach thousands of hours at engine operating temperatures. This results in excessive laboratory time and prohibitive costs to perform a simulated service test. Many methods exist to accelerate the oxidation of alloys. One popular method is to increase the exposure temperature. This increases the scale growth rate since the rate controlling step of oxidation, diffusion through the oxide scale, is a thermally activated process. Therefore, an increase in temperature will thicken the scale faster than lower temperature exposures resulting in quicker degradation and wastage of the alloy or coating. Although this is an attractive method to observe oxidation behavior by this acceleration technique, complications occur due to alternative mechanisms of degradation when compared to service conditions.

The challenge is to predict long-term oxidation behavior from short-term experiments by monitoring the mode of degradation at the temperature of interest without complications from accelerated methods. In this investigation, short-term testing is developed to gain insight on long-term performance by determining inputs into a cyclic oxidation model for life-time prediction. This model operates in an iterative process where one iteration is a thermal cycle. The amount of oxide formed during the high temperature segment is calculated followed by the amount that is lost due to scale spallation during cooling. Retained oxide at the end of this cycle is used as the starting point for the following iteration. The two inputs into this model are the oxide scale growth and spallation behavior. Scale growth behavior is the isothermal growth kinetics that are experimentally determined by thermogravimetric analysis. Oxide scale

spallation behavior is quantified by two short-term experiments of a novel acoustic emission experiment during a 24 hour exposure and the stress measurement of the scale after an exposure to the temperature of interest. Results from these short-term tests and modeled cyclic oxidation are compared to life-times from long-term cyclic oxidation tests

2.0 BACKGROUND

2.1 GENERAL MATERIALS DESCRIPTION

Superalloys are generally considered to be a Ni, Co or Fe based alloy that can maintain significant strength and toughness from room temperature up to 80% of the alloy's melting temperature. Other high temperature properties include environmental stability, low creep rate, high creep rupture strength, low thermal fatigue and low coefficient of thermal expansion. With these types of mechanical properties, superalloys have been incorporated for use in the most demanding applications such as power generation, petroleum refineries, gas turbines (land, marine and air), rocket engines and nuclear power plants. In addition to such robust mechanical properties, engineering of superalloys has also allowed for their use in corrosive environments. Small additions of Al and Cr, allow self passivation in oxidative environments by formation of Al_2O_3 or Cr_2O_3 layers, respectively.

Ni-base superalloys have been regarded as the most advanced of all superalloys with the most complex, subtle and sophisticated metallurgy. The complexity of Ni-base superalloys is founded in the chemical composition and microstructure. This material usually consists of 13 alloying elements and 12 impurity tramp elements. Close control of C, S, Mn, Si, P, O and N is required to minimize their deleterious effects. Microstructure of these alloys consists of a gamma (γ) matrix and gamma prime (γ') precipitates that form a coherent interface with the matrix. It is the

thermal stability of this microstructure that results in the high strength at elevated temperatures. The γ matrix is a FCC austenite usually alloyed with Co, Mo, Cr, Ta, W, Ti, and Al for solid solution strengthening. γ' precipitates, of the Ni_3Al structure are tailored for maximum interphase interfacial surface area as a strengthening mechanism. In polycrystalline alloys, carbon additions are used to form grain boundary carbides to limit grain boundary sliding for increased creep resistance. Additions of boron are also used to increase the cohesive bonding to limit intergranular fracture under creep rupture failure. Development of sophisticated casting techniques has lead to production of single crystal superalloy components and eliminated deleterious grain boundary effects. Such benefits exist since polycrystalline materials exhibit higher creep rates due to shorter diffusion distances and grain boundary sliding as compared to single crystals. Furthermore, other benefits worth noting about the superior performance of single crystal components is the reduction of carbon and boron additions which led to stabilization of the γ' precipitates, and limiting the effects of overaging and allowing higher heat treating temperatures. Furthermore, elimination of grain boundaries has also produced profound improvements on the mechanical properties by increasing toughness.

Through the engineering of optimum mechanical properties, environmental stability has become the limiting factor of the components service life. Achievement of such mechanical properties cannot accommodate chemical requirements for oxidation resistance. Thus, metallurgical coatings (a material with superior oxidation resistance yet somewhat poorer mechanical properties) are used to protect the underlying superalloy substrate. Two classes of coatings are used on Ni-base alloys. The first are the aluminide coatings where aluminum is deposited on the surface of the alloy and interdiffuses with Ni, from the superalloy, to form the NiAl coating. A

Pt-modified nickel aluminide coating is produced by the initial deposition of a thin (~7μm) platinum layer followed by the aluminization process described above. These Pt-modified diffusion aluminide (Pt-Al) coatings have superior oxidation resistance compared to the straight aluminide (st-Al) coatings. Overlay coatings are the second type of coating used with a general composition of MCrAlY, where M = Ni, Co or Ni + Co. Overlay coatings are applied by thermal spraying or electron-beam physical vapor deposition. The singular purpose of these coatings is to increase the oxidation life of the component by preventing the exposure of the substrate to oxidative environments.

2.2 OXIDATION THEORY

2.2.1 Thermodynamics

Metals in general are not stable in an environment containing oxygen. A few exceptions exist for gold and silver at moderately low temperatures. For most metallic elements, a general reaction between the metal (*M*) and oxygen (*O*)in the gas can be written as

$$aM + {}^{b}\!/_{2}\, O_2 = M_a O_b \qquad (1)$$

The Gibb's Free Energy (ΔG) associated with such a reaction is generally negative. A convenient way to graphically display the relative stabilities of these reactions for various types of elements is to use a Richardson/Ellingham diagram as shown in Figure 2. From this diagram, such elements as aluminum, silicon and chromium are near the bottom for unit activity of the

metal, which shows the oxides of these metals are more stable than the oxides of the elements above them and it is this large affinity for oxygen that makes them the desired alloying element for oxide scale formation.

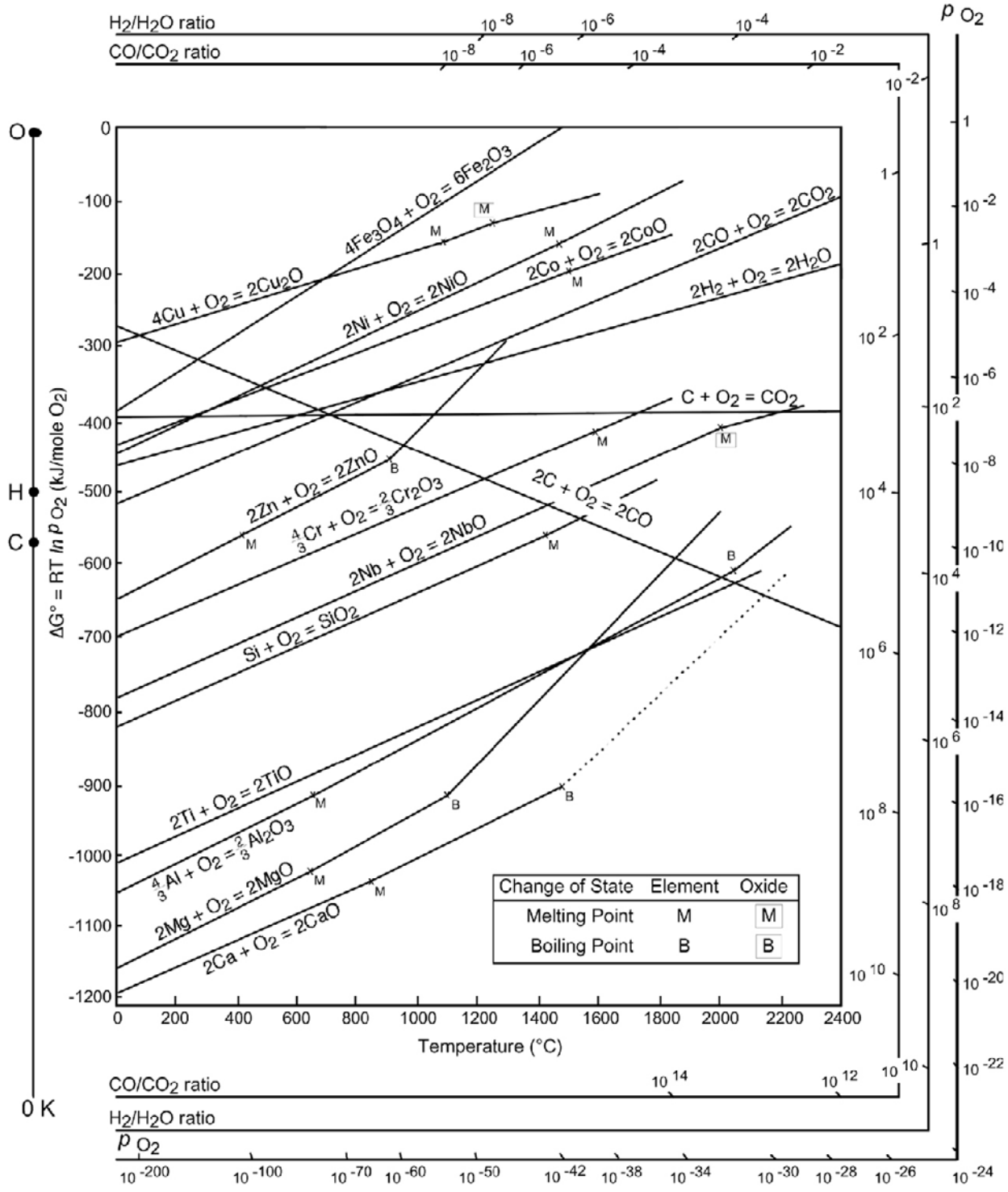

Figure 2. Richardson-Ellingham diagram for oxides.

2.2.2 Oxidation Product

The above section gives insight to which element in the alloy will form the stable oxide, but the morphology of the product is important to form a protective barrier. Upon exposure to oxidizing conditions, the surface elements will react with the oxidant to produce the oxide scale. This product should form a dense continuous scale to separate the two reactants (metal and oxygen). The single purpose of the scale is to act as a diffusion barrier and limit the transport of metal and oxygen atoms from further reaction. The integrity of this oxide scale must be maintained through changes in environment such as thermal cycling and exposures to oxidizing atmospheres with fluctuation in oxygen potential.

2.2.3 Transport

Further oxidation of the metal requires transport of one of the reactants through the scale, the dense oxidation product. Solid state diffusion is the process by which this occurs.

The driving force for metal cation and/or oxygen anion diffusion through the scale is the chemical potential or activity gradient created across the scale as demonstrated in Figure 3[2]. Thermodynamic equilibrium fixes the activities at the interfaces, where the activity of the metal in the oxide is equal to that of the metallic element in the alloy at the metal-oxide intreface, and the apparent oxygen partial pressure will be the dissociation pressure for that oxide. A similar treatment can be utilized at the gas-oxide interface to calculate activity of the metal where the pressure of the oxygen is that in the atmosphere. From these chemical potential gradients, two types of transport can exist. One type is the inward diffusion of the oxygen ions and the other is

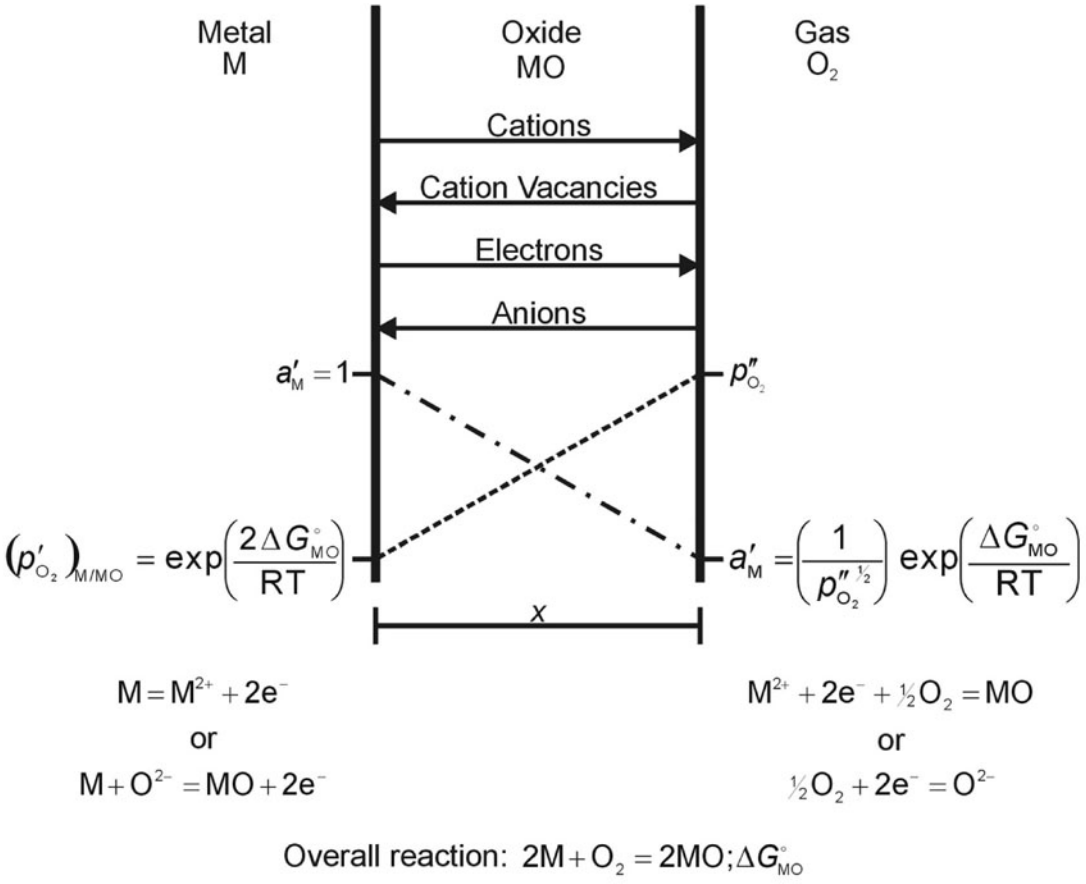

Figure 3. Schematic diagram of species transport and equilibrium reactions.

the outward transport by the cation of the metal species. Electroneutrality is required, and therefore, the fluxes across the scale are accompanied by transport of electronic defects. Figure 3 shows the respective fluxes of ionic and electronic species.

Wagner quantified the diminishing growth rate as the decrease in the thickening of the oxide scale with time[3]. As the scale thickens, the diffusion distance increases ultimately reducing the reactant flux establishing an ever decreasing scale growth rate. He formulated the parabolic rate law, where

$$x^2 = 2 \cdot k_p \cdot t \tag{2}$$

Here the square of the scale thickness, x^2, is proportional to time, *t*, and the proportionality constant is k_p, the parabolic rate constant. It is experimentally easier to continuously monitor oxidation by mass change rather than scale thickness. Similar to Equation (2),

$$\left(\frac{\Delta m}{A}\right)^2 = k'' \cdot t \tag{3}$$

the parabolic rate law can be expressed in terms of oxygen uptake normalized per unit surface area, $\left(\frac{\Delta m}{A}\right)^2$. A comparison of parabolic rate constants for selected oxide scales as a function of reciprocal temperature is presented in Figure 4. In this graph, the parabolic rate constant for mass gain (k'') is used instead of the k_p.

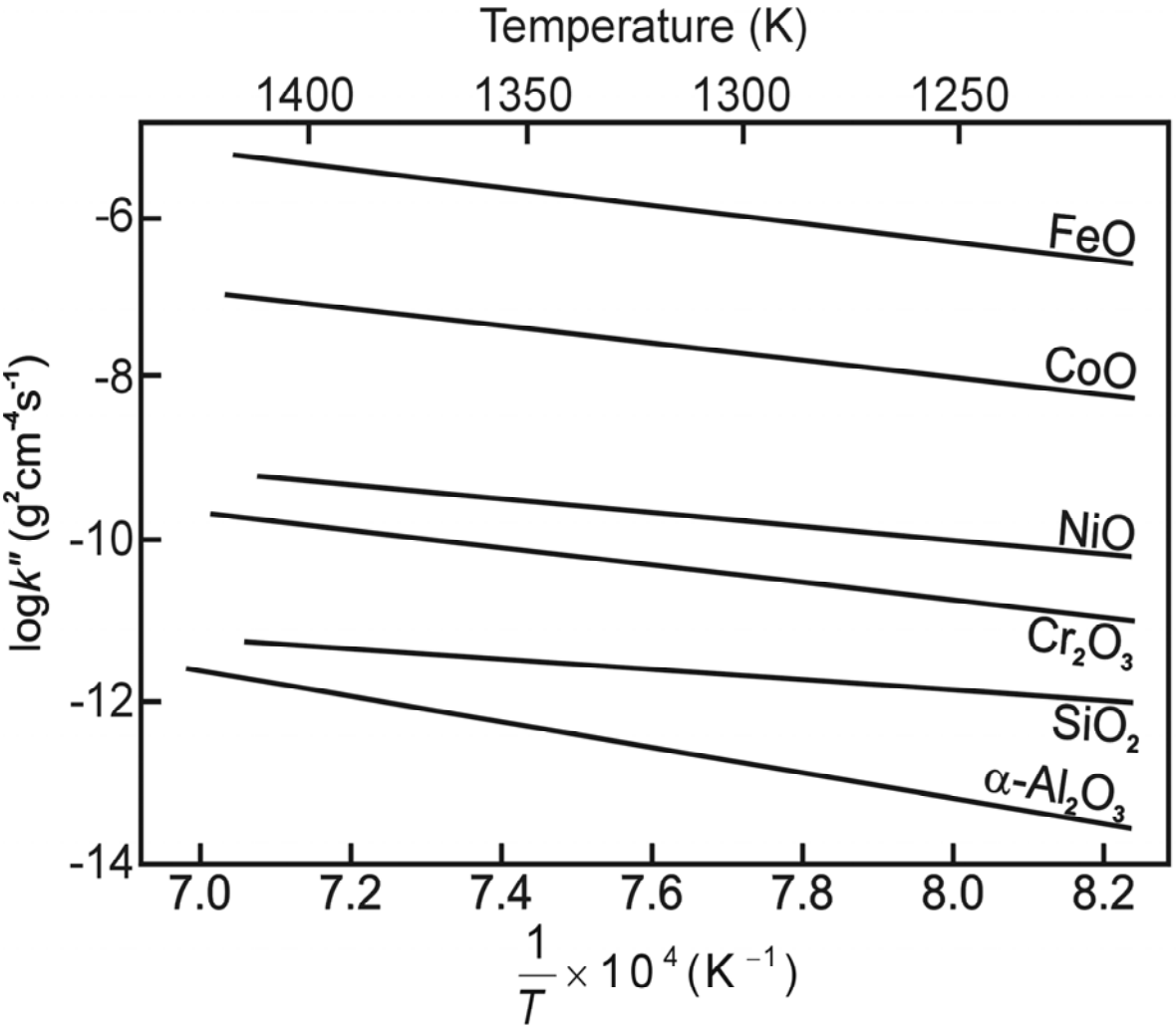

Figure 4. Plot of isothermal parabolic growth constant versus inverse temperature for various oxide scales.

Other rate equations exist for the various types of oxide scales. Different treatments of the transport, rate controlling step and the nature of the scale itself need to be considered.
For the oxidation of a large number of metals at low temperature, a logarithmic rate law can be used to describe the kinetics. This equation is

$$x = k_{\log} \cdot \log(t - t_o) + A \tag{4}$$

and $k_{\log}$, t_o and A are constants. This rate equation represents the behavior of metals at temperatures in the range of 300-400°C. In this temperature range, the oxide scales thicken rapidly followed by insignificant growth. Rate limiting transport of electronic defects or voids in these thin scales are theories that explain this type of behavior.

A linear law exists for a growth rate of a scale that is independent of time or oxide thickness. Here

$$x = k_l \cdot t \tag{5}$$

and k_l is the rate constant for this linear behavior. Transport across a boundary layer or a phase boundary reaction could be the limiting step for this process that results in the linear growth rate. Another phenomenon resulting in growth kinetics independent of scale thickness is the continual cracking of the oxide scale.

From these different rate equations for the oxidation of metals, the parabolic rate equation most accurately describes the behavior of high temperature alumina formers.

2.2.4 Selective Oxidation

The ability for an alloy to form a protective oxide is a thermodynamic and kinetic issue. From thermodynamics, the predicted oxide scale will be of the element that has the largest affinity for oxygen. For this investigation we will focus on alloys that form an alumina layer. During the initial stage of oxidation, all of the elements in the alloy will oxidize and the initial scale will be composed of elements in proportions as they are present in the alloy or coating. Once this transient oxide forms a continuous layer on the alloy, a drop in oxygen activity at the oxide metal interface will only allow the thermodynamically more stable oxide to continue to form. The capability of the alloy to maintain this oxide depends on the amount of this element in reserve and its ability to diffuse to the scale for further reaction. The concentration in the alloy to achieve this can be represented by

$$N_B^{critical} = \frac{V_m}{32\nu}\left(\frac{\pi k_p}{D_B}\right)^{1/2} \tag{6}$$

where $N_B^{critical}$ is the concentration of the oxide forming element in the alloy, D_B is the diffusivity of B in the alloy, k_p is the parabolic rate constant, V_m is the specific volume of the metal and ν is the ratio of oxygen to B in the oxide. This relation is derived by equating the transport of B to the metal-oxide interface from the alloy to that required for continual scale growth determined by k_p. If the actual concentration of B, N_B, in the alloy or coating should drop

below $N_B^{critical}$, diffusion of B in the substrate to the metal oxide interface would not be sufficient. As a result, the local oxygen partial pressure would increase to oxidize other alloy elements or dissolution of oxygen in the alloy could cause internal oxidation of B. This phenomenon has been described by Evans[4] as intrinsic chemical failure, or InCF.

If the scale should spall, direct exposure of the underlying alloy, which has been depleted of the scale forming element, *B*, would result. The critical concentration to reform the same oxide is determined by

$$N_B^* \geq \left[\frac{\pi g^*}{2\nu} N_S^o \frac{D_o V_m}{D_B V_{ox}} \right]^{1/2}. \tag{7}$$

Here N_S^o is the oxygen solubility in the substrate, N_B^* is the concentration of element *B* in the alloy, D_o and D_B are the diffusivities of oxygen and *B* in the alloy respectively, V_{ox} and V_m are the specific volumes of the oxide and metal respectively and g^* is an empirical parameter for lateral growth of oxide precipitates.. This critical concentration of *B* is determined by the ability to transport *B* in the alloy to initial oxide nuclei that results in lateral growth. This initial lateral growth of the oxide particles is the mechanism by which a continuous layer is developed. This concentration of the preferred scale forming element limits the oxidation life for the alloy or coating. Once this element is depleted below N_B^*, the alloy loses the ability to reform the lost B oxide scale and other alloying elements are oxidized. Rapid degradation of the component begins as a result of the nonprotecting nature of these other oxide scales. Failure by this type of

depletion of scale forming elements is referred to as mechanically induced chemical failure, or MICF[4].

Since growing the B oxide after spallation entails a lateral growth component of the oxide, the concentration required to heal the scale, N_B^*, is generally larger than that to maintain the scale growth, or

$$N_B^* > N_B^{critical}. \tag{8}$$

From this, one can deduce that any spallation of the alloy reduces the service life of the component.

2.2.5 Oxide Adherence

The adherence of an oxide scale to the metallic substrate is the greatest concern for oxidation resistance. From thermodynamics, the minimum work required to separate these two phases is the work of adhesion. It can be defined by the Dupre[5] equation as

$$W_{ad} = \Delta G_{ox/m}^{ad} = \gamma_{ox} + \gamma_m - \gamma_{ox/m} \tag{9}$$

Where W_{ad} is the work of adhesion, $\Delta G_{ox/m}^{ad}$ is the free energy change, γ_{ox} is the oxide-gas surface energy, γ_m is the metal-gas surface energy and $\gamma_{ox/m}$ is the oxide-metal interfacial energy.

The nature of oxide scale bonding to the substrate, which has a great influence on the $\gamma_{ox/m}$, is not completely understood. McDonald and Eberhart[6] have performed sessile-drop experiments of liquid metals on an alumina substrate. Their results show a linear relation of the W_{ad} to the free energy of formation for the native oxide of the metal. Part of their analysis shows that, the neighboring atom of the oxide to that across the interface of the metal determines the type of bonding. Metal-aluminum bonds across the interface would result in a weak Van der Waals bonding, but the metal-oxygen bonding across the interface is expected to be ionic in nature. These results are for liquid metals on a static alumina substrate, and caution is necessary when applying these results to solid metallic substrates and a growing scale. Another bonding theory proposes that electrostatic forces can develop from the electric field generated during the scale growth[7].

The nature and strength of the chemical bonding at the oxide-metal interface is extremely sensitive to the impurity levels. Sulfur is the element of major concern where a concentration of only a few parts per million can have profound effects on the cyclic oxidation life of a material[8]. However, there exists a controversy over the mechanism by which S causes deleterious effects. Grabke et. al.[9,10] have only detected S on the metal surface of interfacial voids. Here, the sulfur is not the cause of the void formation, but it reduces the metal surface energy for void stabilization and growth. As these voids grow, a decrease in the average adherence results from reducing the contact area or complete separation by void coalescence could occur. In contrast to these results, sulfur has been detected at the intact metal-oxide interface for alumina[11,12,13] and

chromia[14] forming scales. This interfacial sulfur must be responsible for the weakening of bonds at the interface, or it may have an embrittling effect when it segregates to the interface[15].

Reactive elements (REs), elements with a large affinity for oxygen, have been studied in detail for the past half century. Alloys with the addition of small amounts of oxygen active elements such as Hf, Zr, Y or Ce exhibit great increases in the cyclic oxidation life. With low level (≤100ppm) additions, scale adhesion has also been greatly improved[16,17]. These improvements can be achieved by alloying, ion implantation, or oxide dispersion of the RE oxides.

There have been a number of proposed mechanisms to explain this reactive element effect that include: (1) RE form oxide pegs at the metal-oxide interface to mechanically fix the scale[18]; (2) RE can act as a vacancy sink to eliminate void precipitation at the metal-oxide interface[19]; (3) RE have also been shown to alter the growth mechanism of the oxide scale[20,21]: (4) REs increase the scale plasticity for stress relaxation[22]; (5) REs segregate to the metal oxide interface to form a graded seal and strengthen the metal-oxide bond[23] and (6) REs act as a sulfur getter to prevent segregation to the interface[24].

The strength of the oxide to metal bond is a critical issue due to the large load that is applied to the interface. This load originates from the stresses that form in the oxide layer. There are two types of stresses that need to be considered. First is the growth stresses that form while the scale is growing during the high temperature exposure, and the second is the thermal stress. Growth stresses can result from a number of different mechanisms. One mechanism was proposed by Pilling and Bedworth[25] where the volumetric change during oxidation of a metal would result in

a stress due to the constraint imposed on the oxide scale by the geometry of the metal substrate. They compared metals based on the Pilling and Bedworth ratio (PBR) where

$$\text{PBR} = \frac{\text{volume per metal ion in oxide}}{\text{volume per metal atom in metal}} \tag{10}$$

Metals with PBR greater than one would have oxide scales that grow in compression and less than unity would form tensile stresses in the scale Also from their explanation, scales that form by cationic diffusion would have new oxide form at the oxide-gas interface and would not be subjected to the constraints and form stress free. A second source of growth stresses occurs at the early stages of oxidation. Here lattice strains from epitaxial growth are significant, but as the scale thickens, the contribution would be minimal. Another mechanism could be a gradient in point defects in the oxide scale that results in the change in lattice parameter. This would only occur in oxides that accommodate significant deviations from stoichiometry. Changes in the substrate due to recystallization or phase transformations can alter the stress state. For chromia formers, alloy grain growth has been shown to disrupt the oxide[26], and for alumina formers, phase transformations in nickel aluminide coatings have a similar affect[27]. Compressive growth stress can develop when oxide forms within oxide, as the case of anion diffusion along grain boundaries or microcracks. The following effect has been noted on chromia formers[28]. Single crystal scale (no grain boundaries) grown on pure Cr remained planar and adherent. In contrast, a polycrystalline scale on the same alloy would buckle on the substrate as a response to the stress. These above mechanisms only deal with an oxide on a planar, semi-infinite surface which is not the case of the 3 dimensional components. Hancock and Hurst[29] have formulated an explanation for convex and concave surfaces as a function of cationic or anionic diffusion in the

scale. Cationic transport results in the recession of the metal-oxide interface since the new oxide forms at the oxide-gas interface. This condition with a convex surface results in a compressive stress, while the concave surface would result in initial compression that would transfer into a tensile stress. For anionic diffusion, new oxide forms at the metal-oxide interface and on a convex surface, this new oxide pushes the original oxide resulting in a tensile stress in the outer region of the scale. On the concave surface, a compressive stress develops that increases with time.

The second type of stress occurring in the scale is the thermal stress. This situation is analogous to the bi-metal strip where two dissimilar metals are bonded together. As a result of the different coefficients of thermal expansion (CTE) the strip bends with a change in temperature. For metal-oxide systems a mismatch in CTE is present, but a constraint is applied to the interface. There is no bending since the thickness of the metal is generally orders of magnitude larger than the thickness of the oxide and oxide usually forms on both sides of the specimen. For a planar surface, the stress in the oxide can be determined by[30]

$$\sigma_{ox} = \frac{E_{ox} \cdot \Delta T \cdot (\alpha_{ox} - \alpha_m)}{1 + 2 \cdot \left(E_{ox} / E_m \right) \cdot \left(t_{ox} / t_m \right)} \tag{11}$$

where σ is the stress in the oxide, E is Young's modulus, ΔT is the change in temperature, α is the coefficient of thermal expansion (CTE) and t is the thickness. Subscripts *ox* and *m* denote oxide and metal respectively. Since $t_{ox} << t_m$, the second term in the denominator can be assumed to equal zero and this equation can be reduced to

$$\sigma_{ox} = E_{ox} \cdot \Delta T \cdot \Delta\alpha \tag{12}$$

Where $\Delta\alpha$ is the difference in the oxide and metal CTEs. With this large difference in thickness between scale and substrate, one can conceive that the oxide is forced to conform to the dilatation of the substrate. The magnitudes of these stresses are on the order of four to five GPa compression for an alumina scale on a Ni-base alloy after cooling to ambient temperature from 1000 to 1200°C which places a considerable load on the metal-oxide interface.

The metal-oxide system responds to the growth and residual stresses differently. Growth stresses, are present at elevated temperatures where the strengths of the metallic substrate and the oxide are low. Plastic deformation and creep of the scale and the substrate have been reported for alumina scales on FeCrAlY alloys[31]. For this case, a growth stress of approximately 1GPa has been measured in the scale. At room temperature, the thermal stress has reached a maximum and any additional strain from the growth stress increases the total residual stress in the oxide. Also, the tendency of the alloy and oxide to deform under these loads is reduced. If the residual stress is too large for the interface bonding, cracking and spallation of the scale are the results, as demonstrated in Figure 5. Failure by the initiation of an interfacial buckle with subsequent cracking of the oxide scale is depicted in Figure 5a and the initiation of wedge cracks in the oxide scale followed by interfacial cracking is shown in Figure 5b. If the interface is strong enough, the residual stress can cause deformation of the scale and substrate without scale loss as shown in Figure 5c. Because of the large residual stresses, adherence of the oxide becomes an important issue during thermal cycling.

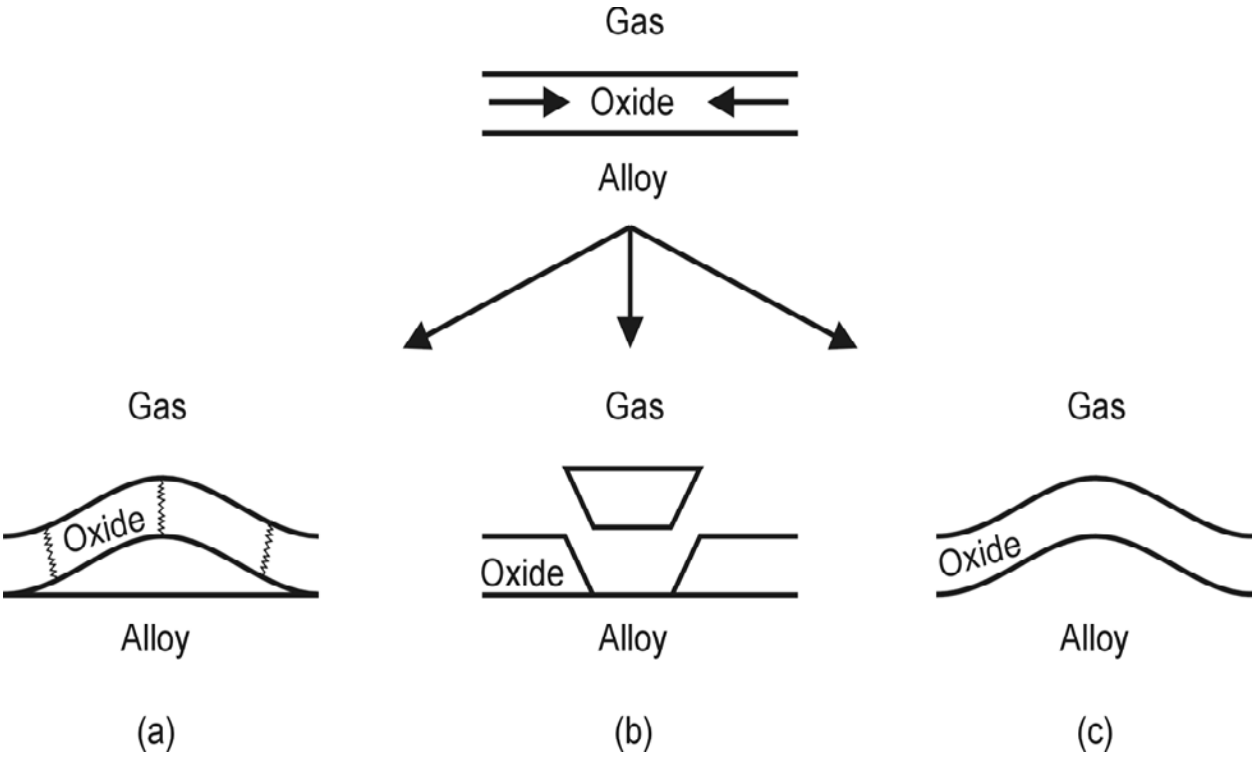

Figure 5. Schematic diagram of oxide and substrate response to the compressive stresses in the scale.

2.3 OXIDATION TESTING

Oxidation testing generally implies exposing the alloy or coating to an oxidizing atmosphere at elevated temperatures. This can be service in a gas turbine engine, exposure in a burner rig apparatus or a simple exposure in a laboratory furnace. Exposure methods are listed in decreasing order of complexity. In the laboratory, parameters of the test including: temperature, temperature cycle, atmosphere and flow rate of the gas can be precisely controlled. Therefore laboratory exposures have become acceptable and attractive means of testing from the lower cost and fewer experimental parameters.

Measuring of the kinetic data during a laboratory exposure is the greatest advantage over other forms of exposure. A simple balance when used in conjunction with the furnace can provide the mass of the sample as a function of exposure time. A setup for this type of thermogravimetric analysis (TGA) is shown in Figure 6. As the alloy or coating continues to form an oxide product, the incorporation of oxygen can be recorded as a mass change. In comparison to the isothermal test, temperature cycling can provide information about the durability of the oxide scale. Figure 7 graphically depicts the cycle for this type of testing where the material is exposed to damage in the transient temperature segments. In thermal cycling, scale growth will occur during the high temperature soak neglecting the insignificant time at elevated temperatures in the transient heating and cooling segments. Yet, it is during these transient segments when large stresses develop in the scale to drive spallation. It is generally accepted that compressive stresses develop during cooling and these stresses are relaxed during the following reheat. An exception

is the relaxation of significant stress during the cooling that would translate into a tensile stress during reheating[32]. If the adherence of the scale is low, spallation of the oxide scale exposes the substrate and a subsequent high temperature soak will test the materials ability to reform the same oxide scale. Due to the complexity of the experimental apparatus, continuous data collection of specimen mass is difficult, but extremely slow scale growth kinetics at the low temperature provides an opportunity to interrupt the experiment to manually record specimen mass. Figure 8 depicts a mass change curve of a hypothetical material exhibiting parabolic growth kinetics in the isothermal curve from such measurements. For the cyclic oxidation curve, mass loss is evident in the initial times and becomes extensive enough for the specimen to exhibit a negative weight change after longer exposure times. Cyclic oxidation produces information about scale growth kinetics and scale adherence.

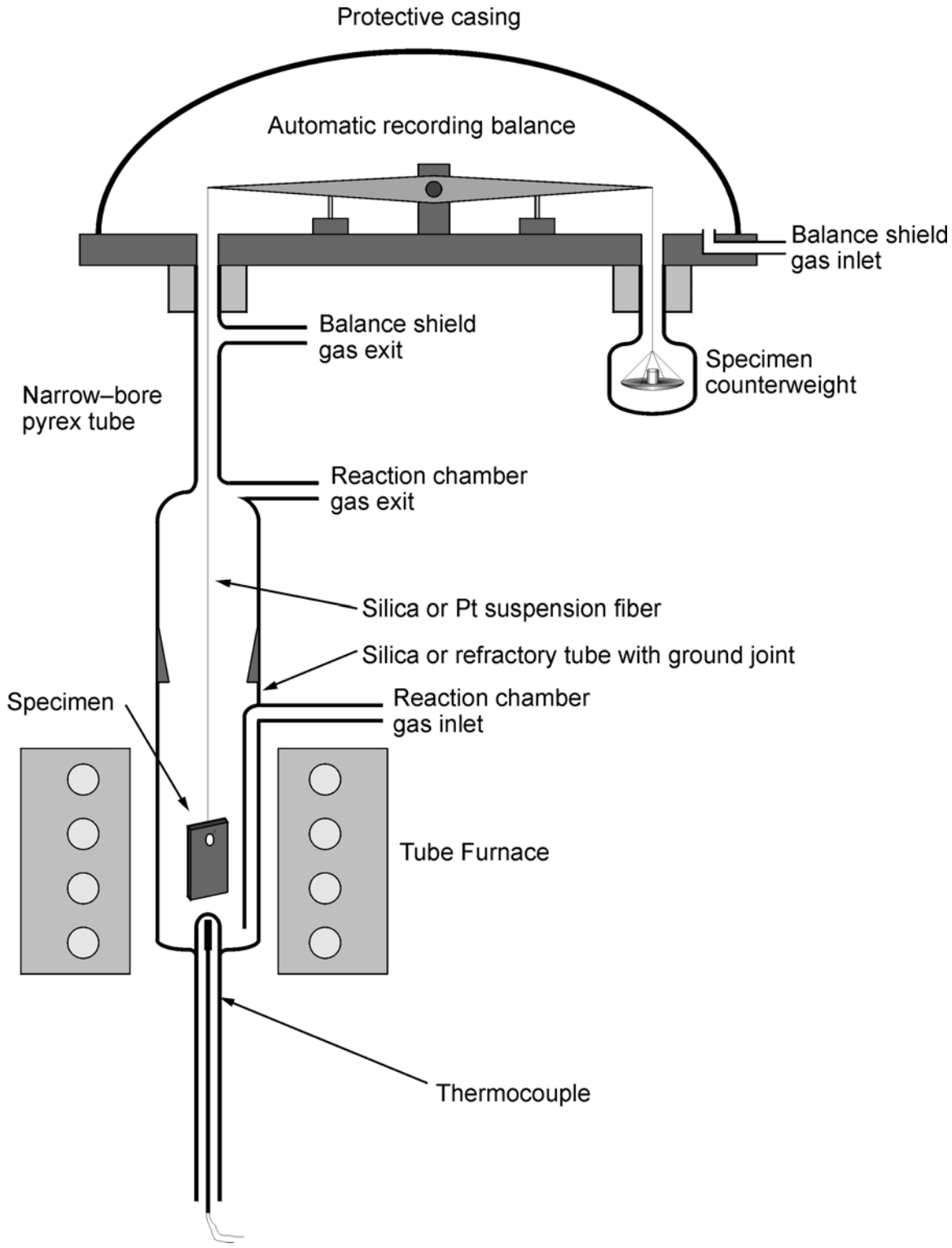

Figure 6. Diagram of typical microbalance and furnace used for TGA (thermogravimetric analysis).

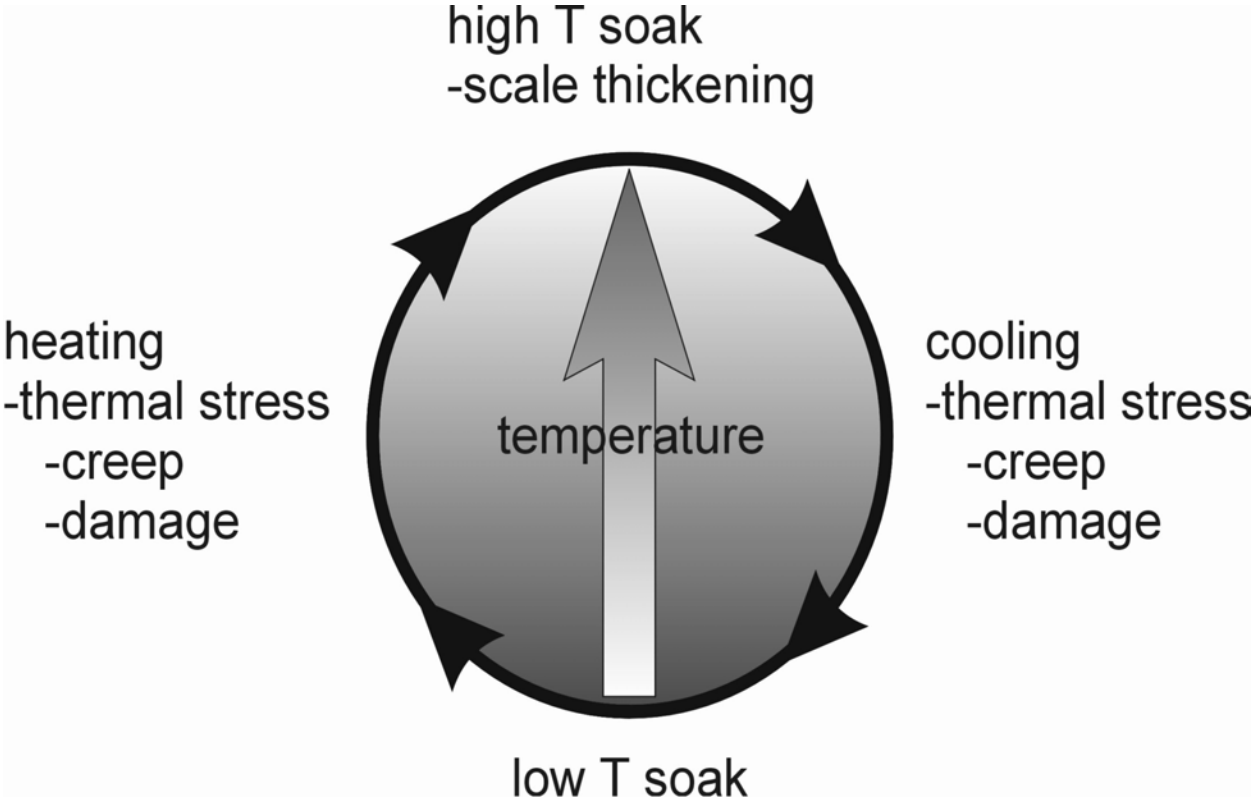

Figure 7. Schematic representation of thermal cycling with four segments labeled. Microstructural and mechanical developments are listed for each segment.

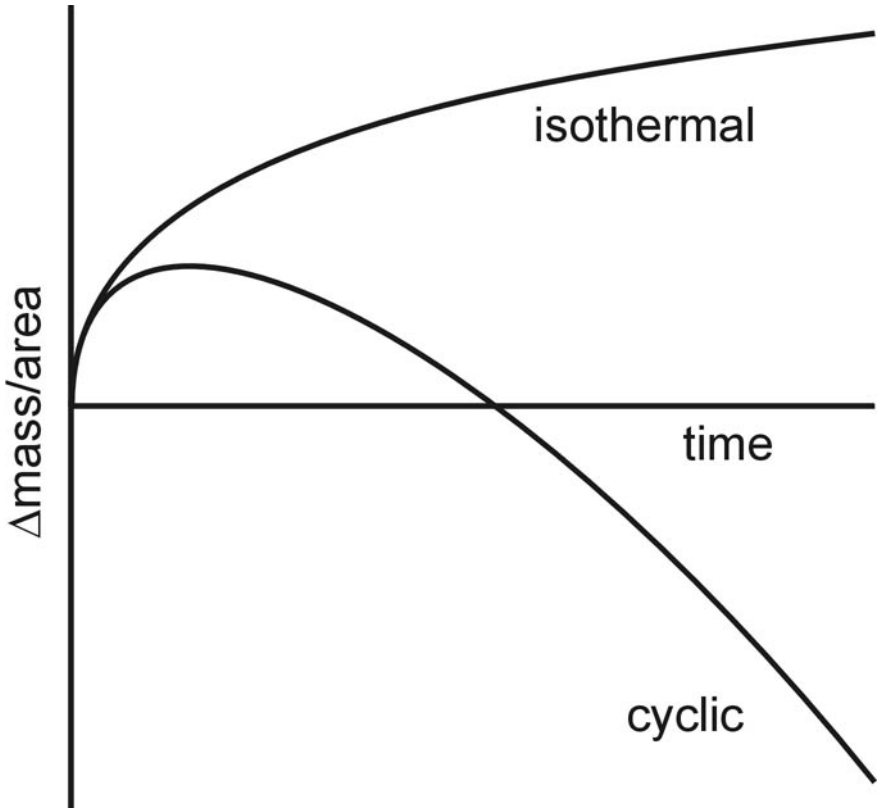

Figure 8. Schematic diagram of typical isothermal and cyclic oxidation mass change curves. Isothermal curve exhibits an ever decreasing mass gain from oxygen uptake, but thermal cycling causes scale spallation evident as mass loss in the cyclic curve.

For a direct means to test the adherence of the scale to the substrate, pull tests have been employed on alumina formers[33]. Oxide scales were pulled off by loading in a direction normal to the surface and a stress value was obtained at failure of the metal-oxide bond. This test is not widely accepted due to the loading geometry. The intrinsic loading of the scale is a biaxial compression due to growth and thermal stresses unlike the load applied by this technique. To avoid this, the entire system, substrate and oxide scale can be placed in compression. This has been used on oxidation resistant coatings with a ceramic topcoat applied for thermal insulation[34]. Critical strains were achieved when the oxide scale, and ceramic topcoat spalled from the compressive loading of the coating. Specimen bending has also been employed to load the scale in a similar compressive mode[35,36]. Although these tests are simple in design, specimens require certain geometries for use in the loading equipment and for strain calculations. Another method that is not sensitive to sample size is indentation. Lateral strains are achieved by the use of an indenter that pierces the scale deforming the substrate plastically and elastically. Induced strain in the substrate translates across the interface and into the scale to increase the in-plane stress that results in delamination. Drory and Hutchinson[37] developed this test for diamond coatings on Ti substrates and used a Rockwell hardness tester with a Brale indenter. In addition to inducing failure by the same intrinsic loading, they also could calculate an interfacial fracture toughness. This method has been adapted to thermally grown oxide scales[38].

2.4 STRESS MEASUREMENT

Quantifying the critical stress to failure, by any of the above techniques requires knowledge of the magnitude of the residual stress in the oxide scale. The residual stress, comprised of the growth and thermal components, is difficult to calculate since the stresses generated at high temperatures are susceptible to reduction from creep and plastic deformation. A measured value of the stress in the oxide would be more accurate than the approximate calculated value. Residual stresses have been experimentally determined by change in geometry of thin oxidized specimens. For thin samples, stress in the substrate cannot be ignored and can be quite significant resulting in elongation due to the tensile load. Using a force balance across the interface with the known or measured thickness of scale and metal, the stress in the oxide can be determined. This method is susceptible to errors in measuring the elongation and in contributions to the elongation from creep of the alloy at high temperatures need to be addressed. Rather than quantifying stresses from microscopic geometric changes, a piezospectroscopic analysis has been developed by Clarke et. al.[39] to measure residual strains. This technique depends on substitutional chromium ions being present in the alumina to act as a source of fluorescence when excited by a laser. The wavelength of the fluorescent photon is dependent on the hydrostatic strain. Measured shifts in this wavelength are used to calculate the stress with the use of piezospectroscopic coefficients.

Original work to gain insight on the growth stresses was by deflection of thin samples after oxidation of only one side of a thin film[40,41]. If a stress develops during oxide formation and

growth, the specimen will bend from the asymmetric loading about the center of the sample. To achieve this, one side of the specimen must be protected from oxidative attack. Deposition of thin coatings of silica has been used to provide the protection required. With the assessed deflection, beam mechanics are used to determine the average stress in the scale. Calculating this stress requires knowledge of the substrates elastic, plastic and creep behavior at the high temperature. In addition, the effects of the oxidation resistant coatings on the beam deflection are critical to the solution

Since x-ray diffraction (XRD) is the most accurate method to measure lattice spacing, this accuracy can be utilized for the measurement of the lattice strain from macroscopic stresses[42,43]. For thin compressed scales, the directionality of the biaxial stress of the scale will compress the planes that are normal to the surface, while expanding the planes that are parallel to the surface. A schematic of the effect of strain on the (hkl) spacing is shown in Figure 9. The measurement of this shift as a function of the tilt angle from the surface normal depends on the magnitude of this stress. In addition to residual stress measurements, this technique can also be directly applied to high temperature measurements of growth stresses.

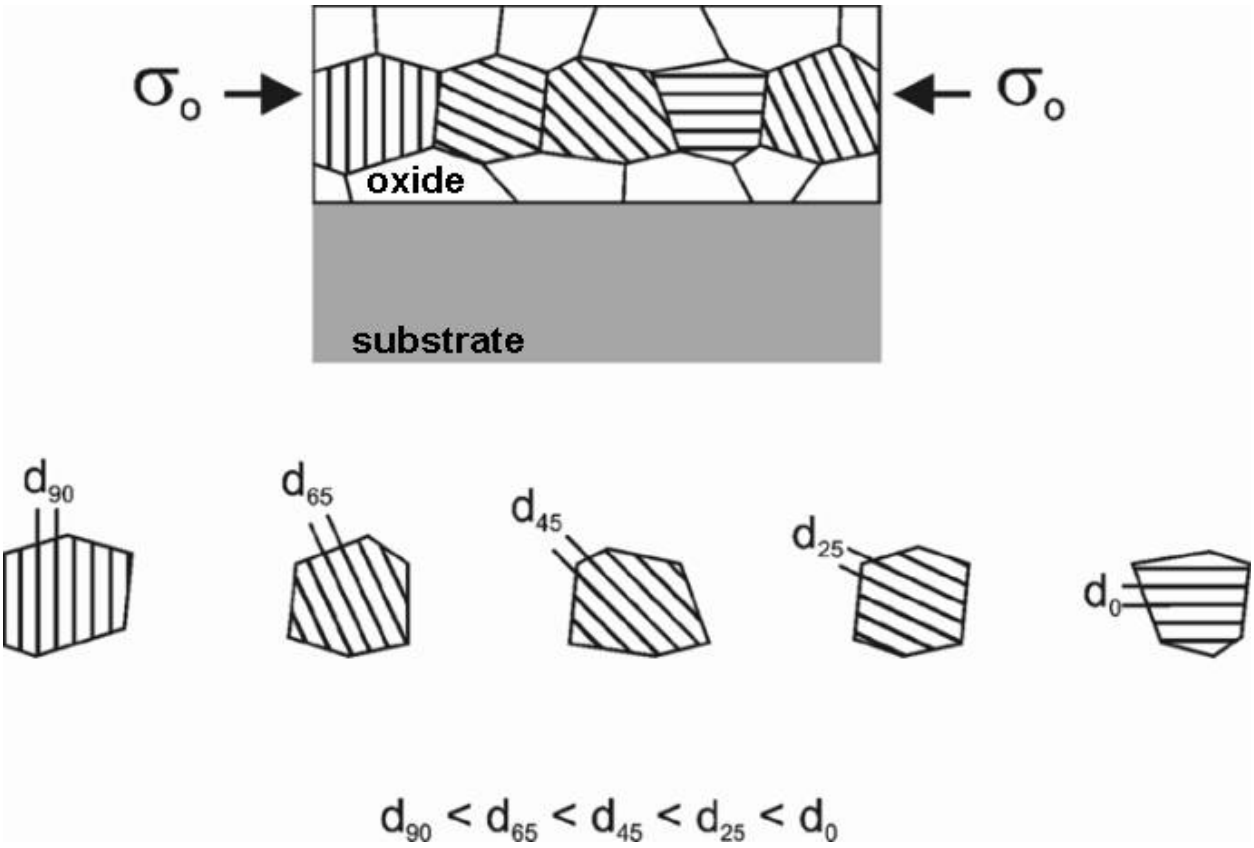

Figure 9. Schematic diagram showing the change in a plane spacing with respect to plane orientation. Subscripts on d are angles between lattice plane normal and sample surface normal.

2.5 OXIDATION MODELING

A great deal of information about the oxidation of alloys and coatings is obtained from isothermal TGA data. Furthermore, a number of widely accepted theories have been developed to describe and quantify the mechanisms controlling isothermal oxidation. However, most in-service exposure conditions entail thermal cycling where isothermal TGA data does not provide insight on the spallation behavior. To describe and understand factors affecting cyclic oxidation, mechanistic models have been developed to quantify scale growth and loss in a manner to generate mass change curves similar to those obtained from cyclic oxidation testing. Models employed in this investigation and described below are cyclic oxidation spall program (COSP) uniform layer (UL)[44,45,46] version, COSP Monte Carlo (MC)[45,46] version, deterministic interfacial cyclic oxidation spall model (DICOSM)[47] and a statistical model developed by Monceau[48]. Each model operates on the same principle and basic iterative process where oxide forms during the high temperature segment of the cycle and spallation occurs during the cooling segment. Where these models differ greatly is in the approach each model employs on statistically managing oxide spallation during cooling.

The operation of the COSP-UL, mathematically the simplest of the four, is the following. On the initial cycle, oxide growth is purely a brief isothermal experiment where the growth rate follows a prescribed behavior. The isothermal growth kinetics allow determination of the weight of oxide after the heating portion of the cycle prior to cooling, W'_r. During the subsequent cooling step of the cycle, a portion of the oxide will spall with a mass of W_s. After the cycle is complete, the total mass of the oxide retained, W_r, is the starting point for the next cycle as graphically

shown in Figure 10. COSP-UL works with two assumptions. First, the kinetics of the oxide growth is constant and the oxide scale growth rate is a function of the oxide thickness. The second assumption is that the amount of oxide that spalls after each cycle is only dependent on the amount of oxide present after the preceding cycle.

To look at these steps of the COSP-UL in more detail, consider a material that exhibits parabolic growth kinetics where the parabolic rate constant is k_p. On the first cycle, the weight of the oxide per unit surface area would be W'_r and it is obtained from

$$W'_{r,i} = \xi \cdot k^{1/2} \cdot \tau^{1/2}. \tag{13}$$

In this equation, ξ is the stoichiometric constant (mass of oxide/mass of oxygen) and τ is the time at elevated temperature per cycle. The subscript i represents the cycle number and for this case it is equal to one. During the cooling segment, a portion of the oxide will spall and in the COSP-UL a thin section of uniform thickness will spall over the entire specimen surface leaving an attached uniform layer of oxide. This type of spallation requires cracking within the oxide scale. Determining the amount of spallation requires introducing new terms. The fraction of the oxide that spalls, F, is proportional the amount of oxide that is present where

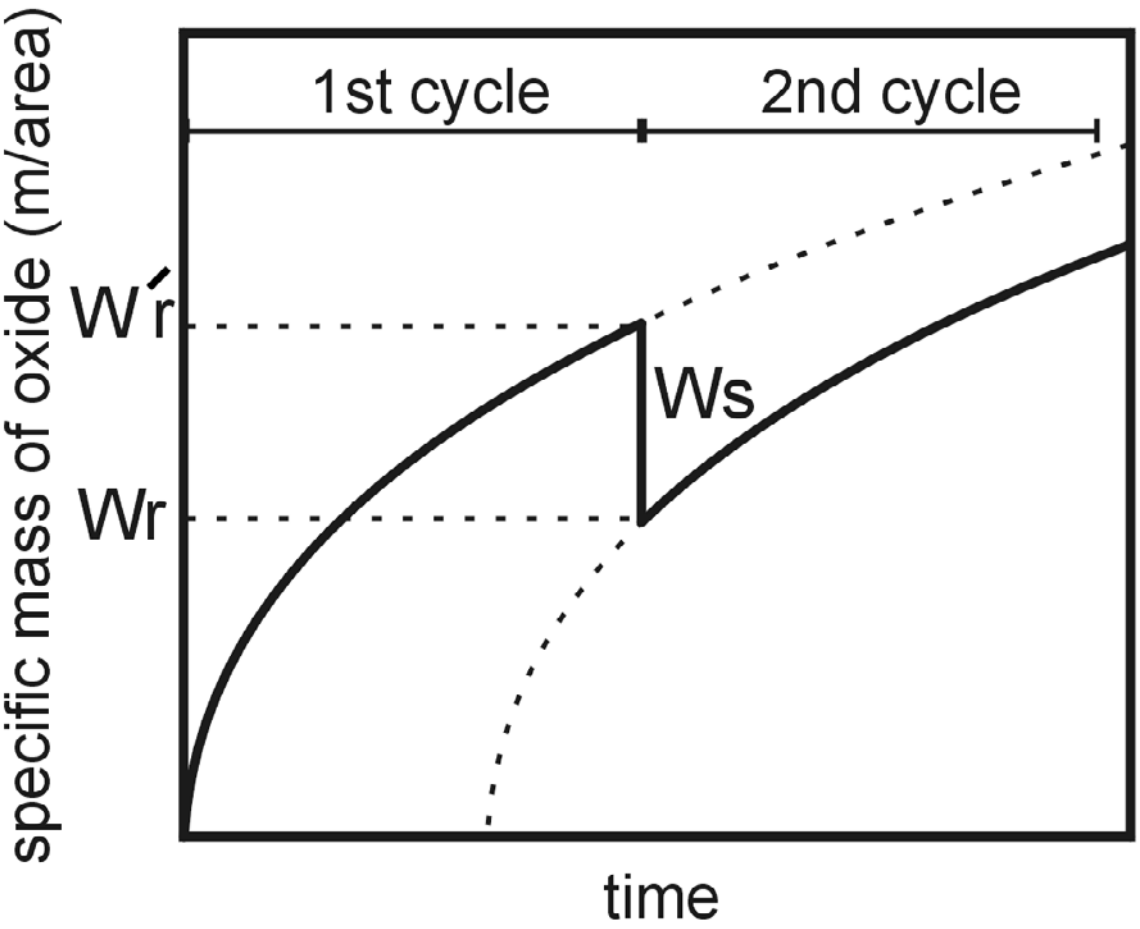

Figure 10. Weight of oxide in COSP-UL versus time at temperature

$$F = Q_o \cdot W'_{r,i}, \tag{14}$$

and *Qo* is defined as the spall constant. This relation has been empirically determined by careful mass change measurements on a NiCrAlY alloy[47] and this linear relationship between *F* and W'_r is shown in Figure 11. With a known value of *F*, the weight of the oxide to spall per unit area is

$$W_{s,i} = F \cdot W'_{r,i}. \tag{15}$$

With the $W'_{r,i}$ and $W_{s,i}$ for this cycle, the $W_{r,i}$ can then be calculated by

$$W_{r,i} = W'_{r,i} - W_{s,i}. \tag{16}$$

For the subsequent cycles, a smaller amount of new oxide will form since some oxide is retained after the first cycle, as shown in the schematic in Figure 12. An effective time is required to calculate the growth of the scale for the next cycle. Since the growth rate of the scale is dependent on the amount of oxide present the time required to accumulate an amount of scale W_r, can be calculated by

$$W_{r,i} = \xi \cdot k^{1/2} \cdot \tau^{1/2} - Q_o \cdot \xi^2 \cdot k_p \cdot \tau \tag{17}$$

from this $W_{r,i}$ can then be expressed in terms of the effective time (t_{eff}), the total hot time required to form $W_{r,i}$ amount of oxide, as

$$W_{r,i} = \xi \cdot k^{1/2} \cdot t_{eff,i}^{1/2} \tag{18}$$

where

$$t_{eff,i} = \tau (1 - \xi \cdot k^{1/2} \cdot \tau^{1/2} \cdot Q_o)^2 \tag{19}$$

With t_{eff}, the total weight of the oxide present after the second cycle, prior to spallation, is

$$W'_{r,i} = \xi \cdot k^{1/2} \cdot (t_{eff,i} + \tau)^{1/2} \tag{20}$$

For the subsequent cycles, an iterative process from Equations 14 to 20 is used to calculate the virtual $W'_{r,i}$, $W_{s,i}$, $W_{r,i}$ for each cycle and a plot of these variables is shown in Figure 13 and a hypothetical mass change curve is shown in Figure 14. In calculating these curves in Figure 14, isothermal growth kinetics were held constant for each curve and only Q_o was varied to show the effect.

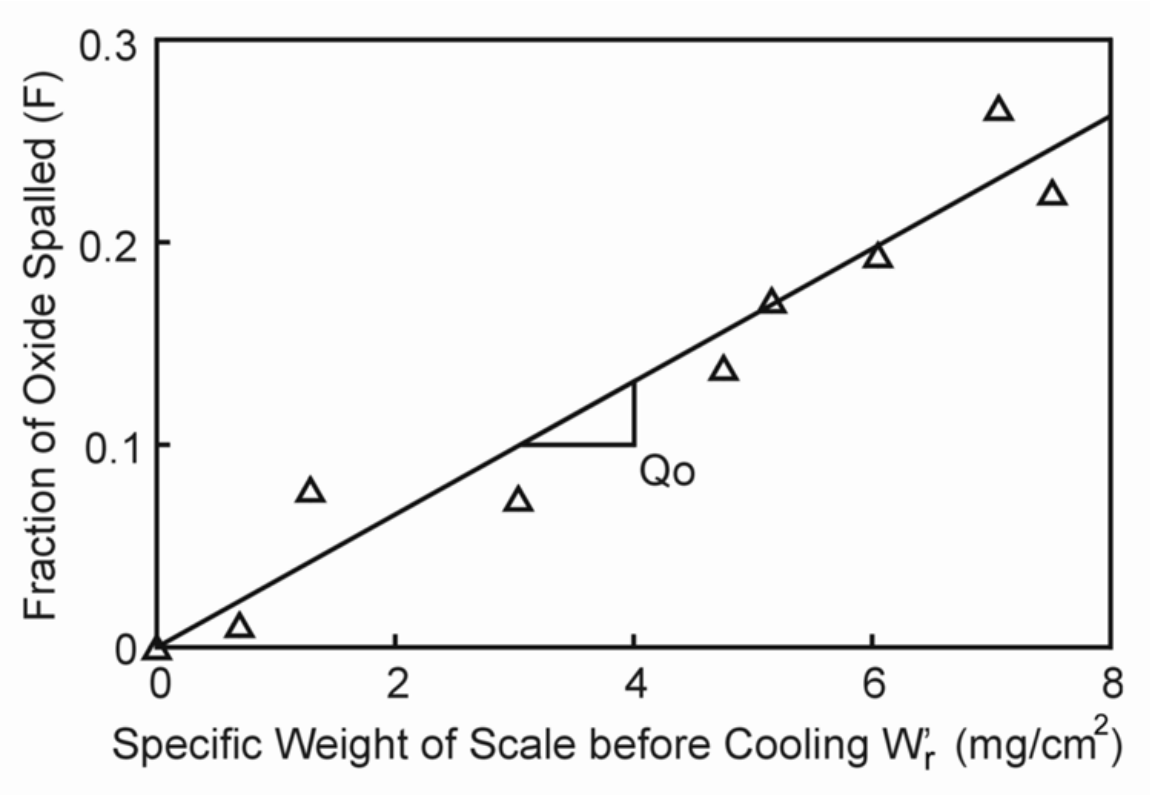

Figure 11. Plot of fraction of oxide that spalls (*F*) exhibiting linear relation to the amount of oxide present prior to spallation (W'_r).

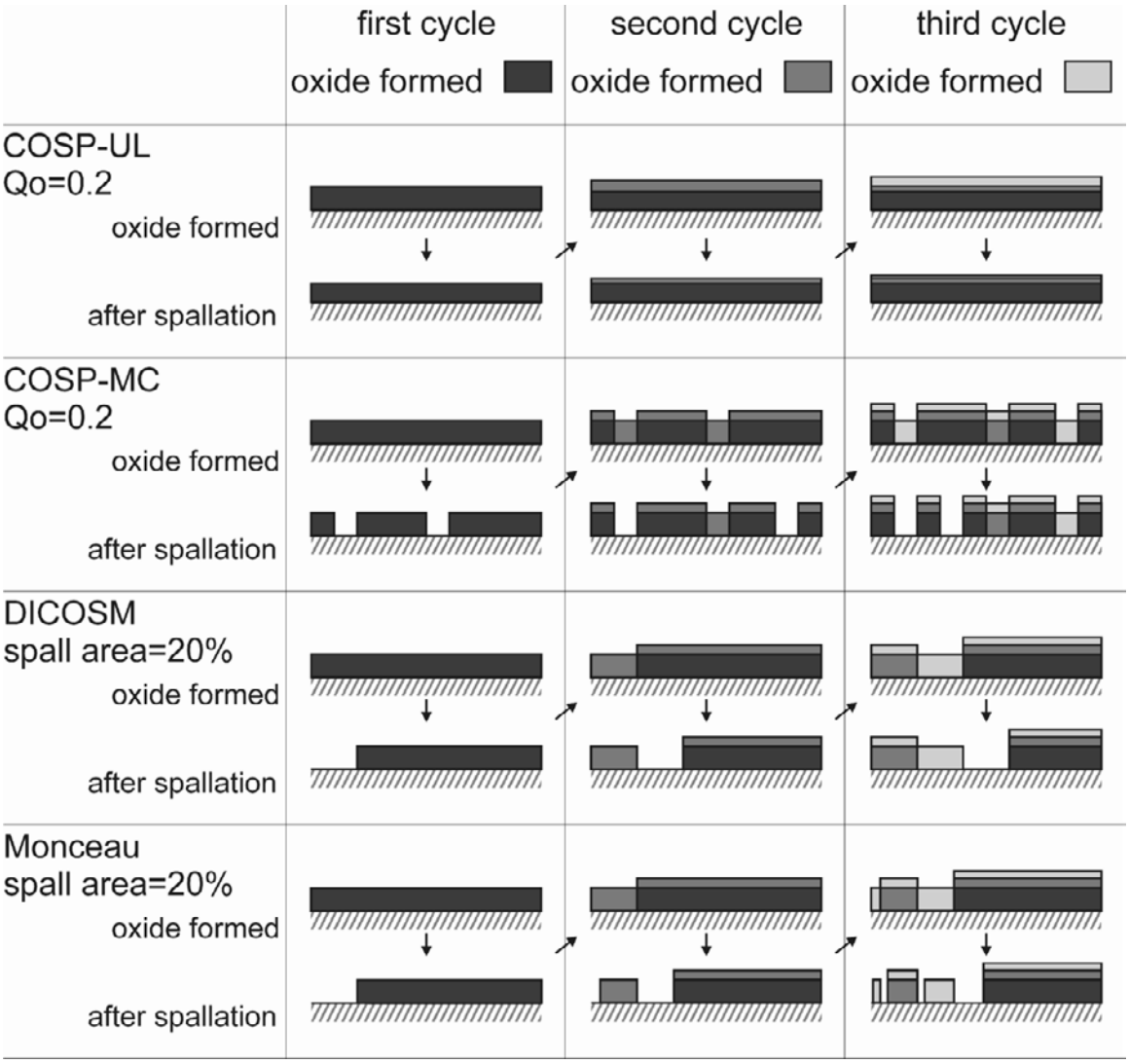

Figure 12. Schematic representation of cyclic oxidation models for the first three cycles. For this relative comparison spall area is 20% and Q_o is 0.20.

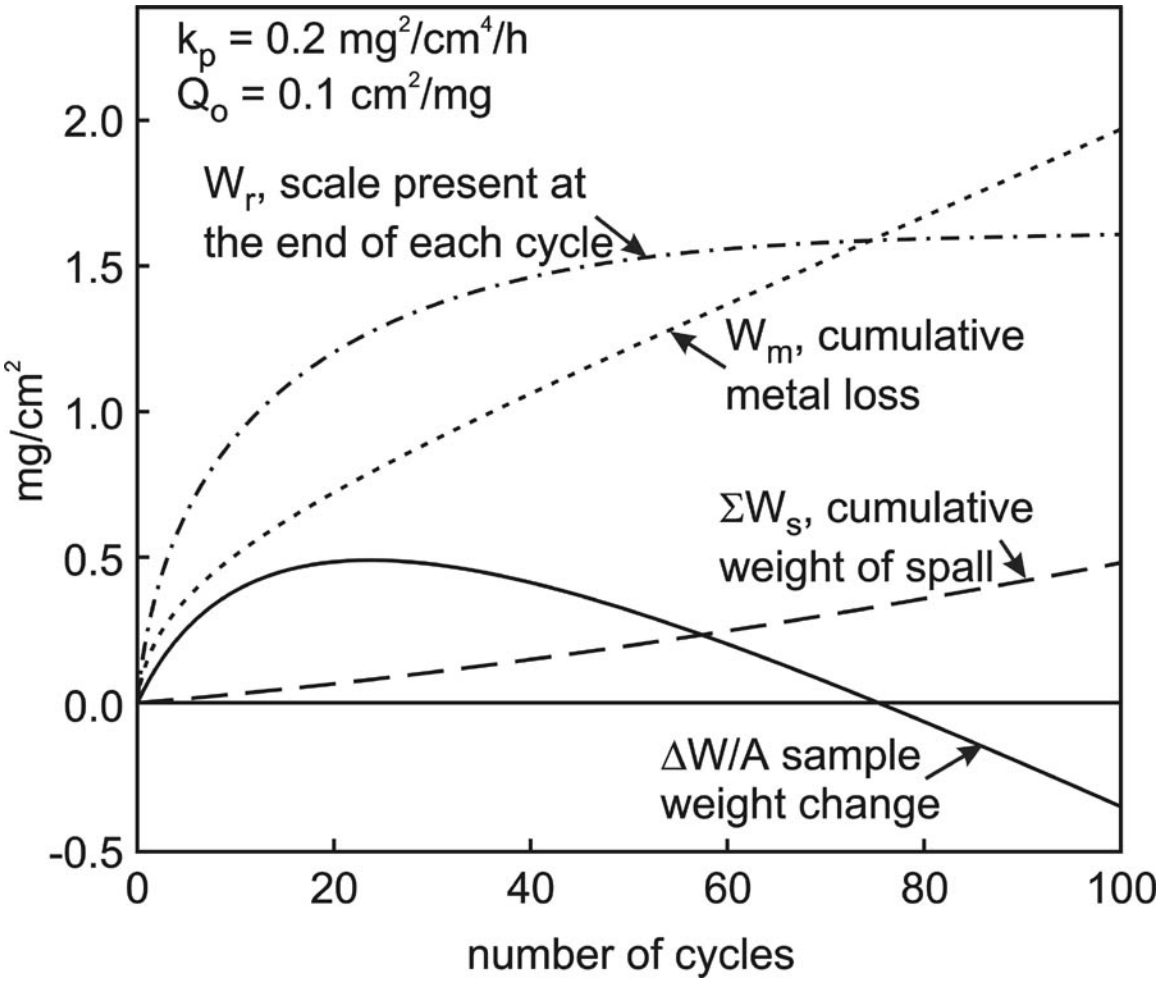

Figure 13. Plot showing the progress of important variables in the COSP model.

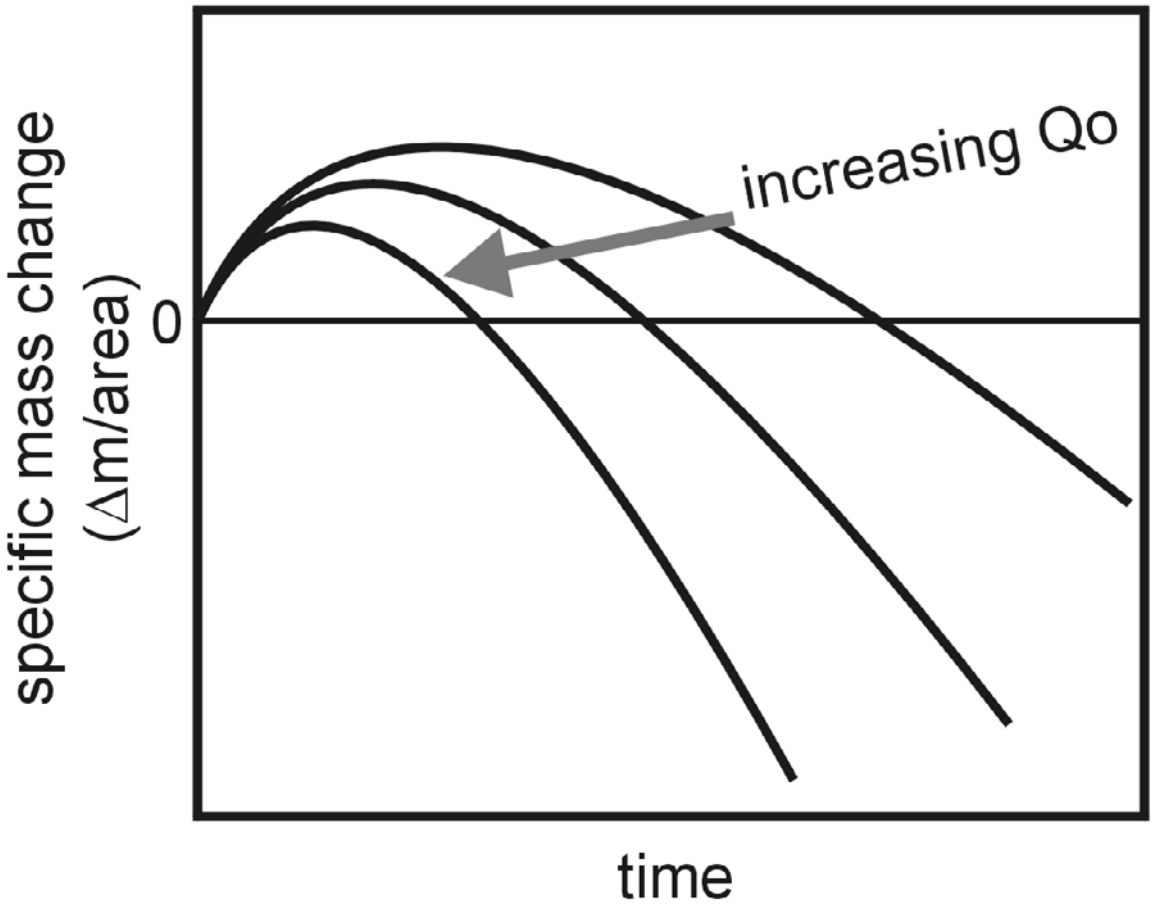

Figure 14. Plot of specific mass change versus time curves generated by COSP. Each curve is for material of same oxide growth kinetics show the effect Q_o.

In the COSP-MC, the surface of the sample is divided into separate areas and the growth and spallation of the oxide is treated independently for each area. This treatment allows complete oxide loss to expose the metallic substrate over discrete areas on the specimen. Localized spallation to the substrate is more representative of actual failure of the scale rather than spallation of a thin layer over the entire surface. The amount of surface area that exhibits spallation is handled in a probabilistic manner hence the Monte Carlo designation. On a per surface unit basis, $W'_{r,i}$ is similar to that of the UL version, yet the fraction of the spalled oxide will be unity only when complete spallation occurs. The probability for complete spallation to the metal-oxide interface to occur is determined by

$$P = Q_o \cdot W'_{r,i}. \tag{21}$$

If the condition is met for complete spallation, $W_{s,i}$ would equal $W'_{r,i}$ and an oxide free surface would be ready for exposure on the next cycle. If no spallation occurred, the oxide would continue to grow on the following cycle according to isothermal kinetics. Calculating t_{eff} is simpler in the COSP-MC since the value will be an integer product with the cycle time, or

$$t_{eff,i} = \tau \cdot n \tag{22}$$

where n is the number of cycles. In the event of no spallation, n is the number of cycles or if all oxide would spall, n is zero. A schematic representation of this model is presented in Figure 12 for a comparison to COSP-UL. Behavior of several surface segments are averaged to determine

the behavior of the complete surface and a plot similar to Figure 14 can be constructed. Use of this type of model has had success predicting the oxidation behavior of NiAl alloys [49,50] and RE doped NiCrAlY[51,43]. Fitting of the curves to represent the alloy or coating behavior has been limited to statistical regression of the experimental data to solve for the two unknowns, the spall factor and the isothermal parabolic rate constant. The k_p for the particular material is readily obtained from short-term testing, but the spall factor remains a difficult parameter to measure.

Both DICOSM and Monceaus's model assume that spallation occurs by fracture at the metal-oxide interface like the COSP-MC. Rather than distributing spallation in a random manner, each model predicts a constant area fraction during cooling in each cycle. In DICOSM, the surface is divided into surface segments of identical size, like the COSP-MC, and the number of segments equals the reciprocal of the area fraction that spalls. This results in one segment spalling for each cycle and it is one of the segments with the thickest oxide that spalls. Spallation in this manner is supported by fracture mechanics where the thickest oxide would spall assuming interfacial fracture and a uniform interfacial toughness of the entire sample. Monceau also worked with this constant area fraction of spallation, but the surface is divided into segments grouped together by the thickness of the oxide. Each thickness group will spall the same percentage determined by the area fraction. From this, the number, size and distribution of groups change with each cycle, but in this formulation, Monceau has developed this model with an analytical solution. Such a solution removes the iterative process and complicated computer programming required. For comparison to the COSP, progress of each model is schematically shown in Figure 12.

2.6 ACCELERATED TESTING

Since oxidation lives of some modern alloys and coatings are expected to be thousands of hours, a dilemma is faced on how to test such a material in a reasonable amount of time. There are two methods to consider. One possibility is to accelerate the degradation process. This would entail identifying the life limiting mechanism and designing a particular test that would only modify (increase) its effect on the life. The other method would be life prediction by short-term testing. For this type of testing, the mechanism would be monitored in the early stages and the behavior would then be used to rate the material's performance

2.6.1 Acceleration of a Mechanism

Since the degradation processes are thermally activated, an increase in temperature will increase the rate. Consider the parabolic rate constant. Its dependence on the diffusion of the controlling species is shown in Figure 3. From this one can propose that a simple increase in temperature would increase the reaction rate that ultimately increases the degradation of the material and shorten the life. This trend is shown in Figure 15 where the natural logarithm of the reciprocal lives of TBC coated specimens are plotted against the reciprocal of the exposure temperature. The relationship is shown over the temperature range and extrapolated to lower temperatures for failure times in tens of thousand of hours. One also needs to be cautioned, that the rate controlling mechanism must not change. The onset of another rate controlling process will result in erroneous predications from accelerated degradation.

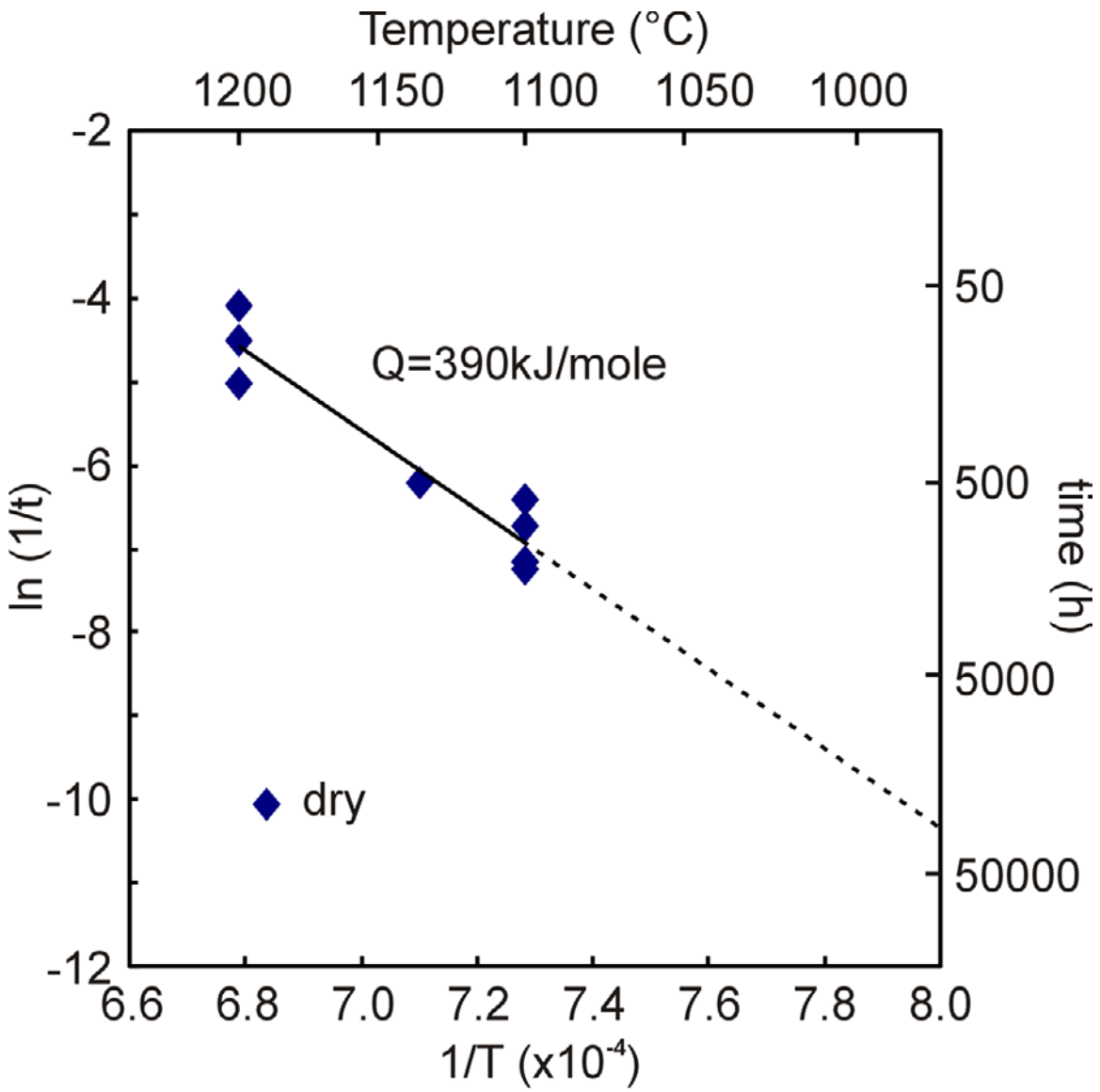

Figure 15. Arrhenius type plot for the failure of thermal barrier coatings. Failure of TBC system is the spallation of the ceramic topcoat.

2.6.2 Short-Term Testing

Short term testing is not an accelerated test by the exact meaning, yet can provide information about performance in an accelerated manner. There is no acceleration of the mechanism under investigation but rather monitoring of the mechanism in a way that permits prediction of long-term performance. The most convenient method to judge long-term performance is by using the parabolic rate constant for cases where oxidation is diffusion controlled. Scales that are slow growing have always been used in high temperature oxidative environments due to the thinner scales and low alloy consumption. Because of this, alloys with rapidly growing scales are generally omitted from high temperature applications. This is a necessary but not sufficient condition. Short-term cyclic oxidation tests are also used for long-term prediction. This type of test is usually used to screen out alloys or coatings that have high positive or negative weight changes. As mentioned in previous sections, quantifying scale adherence in early stages of oxidation can be used as short-term testing. Scales with low initial adherence could be considered to develop problems with spallation later in service life.

One could propose that certain beneficial characteristics observed in the short-term behavior could have profound effects on the long-term performance. Generalities like this could be drawn for all aspects of oxidation behavior, but caution needs to be employed. It was found that small grains of NiCrAlY alloys suppress the transient oxidation period compared to large grains, yet there was little effect on the long-term oxidation[52]. Another account was the long-term (720days) cyclic oxidation performance of Ni-Cr and Fe-Cr alloys. Here the differences in

initial weight changes (up to 45days) were almost indiscernible yet profound differences were apparent at the end of the test[53]. Results are shown in Figure 16.

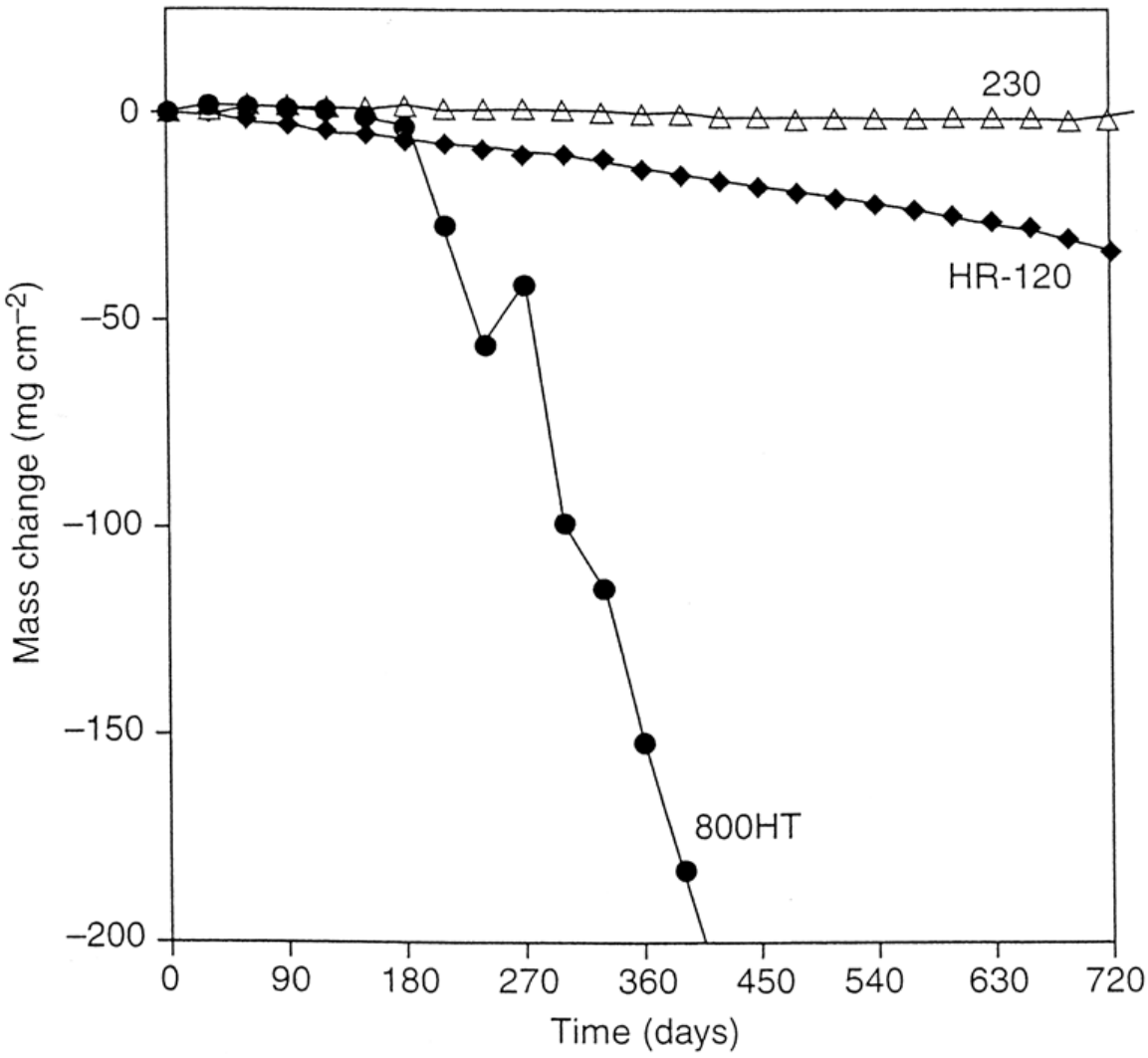

Figure 16. Plot of long-term cyclic oxidation for Fe-Ni alloys HR-120 and 800HT and Ni alloy 230[53].

2.6.3 AE experiments

The stresses that form in the oxide scale are the driving force for cracking and ultimately spallation of the oxide scale. This type of event leads to the release of the stored elastic strain energy within the oxide. This release results in acoustic emission (AE). Associated with this dynamic fracture, a portion of the released energy manifests itself as a propagating elastic wave that can be monitored and recorded on a per event basis. Features of the AE such as peak amplitude, duration, frequency and energy should be characteristic of the type and magnitude of each event.

Monitoring AEs in the field of oxidation testing has brought about a number of novel tests for performance ranking. One set of experiments was conducted on NiCrAlY alloys during isothermal exposure and cooling to room temperature[54] AE were recorded through the one cycle experiments to show AE activity during the hold during scale growth at temperature followed by an increase in this activity during cooling. Interest was focused on the behavior during cooling where the scale is loaded by the thermal stresses. Since the thermal stress magnitude is proportional to the change in temperature and with the use of AE to determine the temperature for the event (cracking and spalling), a critical stress was calculated. The use of thermogravitmetry to compliment AE data was also used during isothermal exposures of FeCrAl alloys[55]. During these exposures, AE activity from cracking and spalling was successfully correlated to the sudden loss of mass. Another interesting test was the monitoring of AEs from the alloy Rene N5 after cyclic oxidation by immersion in water[56]. AE activity was determined to be related to mass loss from cyclic oxidation and an increase in activity was observed upon

immersion in water after the end of high temperature exposure. From these types of tests, the ability to quantify degradation of oxide scales with a non-destructive and an *in situ* technique has become attractive in recent years.

3.0 PROBLEM STATEMENT, SHORT-TERM TESTING AND MODELING

Due to the long oxidation lives of modern alloys and coatings, there is a desire to rate the performance of these materials by accelerated or short-term testing. Rather then accelerate a mechanism for rapid data acquisition to rank a materials performance, short-term testing will be developed to obtain information about the materials performance in an oxidation test. The use of TGA, acoustic emission and stress measurement data will be used to quantify inputs into existing models. It is the purpose of this investigation to explore the use of short-term test data in conjunction with modeling and ultimately the feasibility to rate the cyclic oxidation performance of these materials via life-time prediction

4.0 EXPERIMENTAL

4.1 ALLOYS AND COATINGS

The alloys studied in this investigation are two Ni-base superalloys Rene N5 and PWA1484, FeCrAlY and pure Nickel. Compositions of these alloys are listed in Table 1. The two superalloys are cast single crystal nickel-base superalloys with a gamma matrix and gamma prime precipitates. Two subgroups of N5 were studied, but not in a direct comparison. The First type is a low sulfur content alloy with a concentration of S less than 3ppm which was used as uncoated coupons. The other is a normal content sulfur, 8-10ppm, N5 coupons of which were coated with both aluminide and Pt-modified aluminide diffusion coatings. The iron alloy is a commercial grade high temperature alloy with the trade name Fecralloy. All alloys and coatings are alumina forming systems except for Ni. Specimens of 99.999% nickel were also studied as a comparison to another oxide forming system. Surface conditions varied for each system. Alloys were sectioned to create the test specimen geometry then all surfaces were ground to a 600 grit finish. The aluminide coatings were generally exposed in the as-coated state, but a few were precision polished to a 5μm finish to remove surface roughness. All specimens were ultrasonically cleaned in soapy water, and then ultrasonically cleaned in acetone.

Table 1. Alloy Composition (weight percent) and Coating Descriptions

Alloy	Ni	Fe	Cr	Al	Co	Ta	W	Mo	Ti	Hf	Zr	Y	Re
FeCrAlY		Bal.	22	5							0.1	0.1	
LS N5	Bal.		7	6.2	7.5	6.5	6	0.6	1	0.1			3
1484	Bal.		5	5.6	10	8.7	6	2		0.01			3
Ni	99.999												

Coating	
St-Al	diffusion aluminide coating in N5 superalloy
Pt-Al	Pt modified diffusion aluminide coating in N5 superalloy

4.2 HIGH TEMPERATURE OXIDATION EXPOSURE

4.2.1 Isothermal Exposures

Isothermal exposures were performed in a resistance heated tube furnace. A silica reaction chamber was used in the furnace to provide a barrier from the heating elements and for atmospheric control. The furnace and reaction chamber were oriented in a vertical position. Specimens of the alloys and coatings were suspended from a Pt wire and inserted into the furnace from above. The exposure gas used for these experiments was either dry bottled or ambient air and the temperature ranged form 1050°C to 1175°C. Isothermal tests were used for acoustic emission experiments and to measure isothermal scale growth kinetics. Thermogravimetric analysis (TGA) was performed using a Cahn D200 microbalance with a setup shown in Figure 6.

4.2.2 Cyclic Oxidation

Cyclic oxidation tests were also performed in a resistance heated furnace, but with a horizontal configuration. One hour cycles were preset to 45 minutes in the hot zone at the exposure temperature and 15 minutes in the cool zone. This cycle was achieved by automated mechanical insertion to the hot zone of the furnace and extraction of the sample. Since the samples were confined to the reaction chamber in close proximity to the furnace, the lowest temperature of the cool segment was approximately 100°C. The progress of cyclic oxidation was followed by monitoring the mass change of the specimen. Weight recording was not an automated process therefore the samples were manually weighed once a day during the cool segment of the thermal cycle until the test was terminated.

4.3 ACOUSTIC EMISSION

Acoustic emission experiments were used to monitor the cracking and spalling of the oxide scale by the AE activity. These tests were only performed during isothermal exposures to avoid extrinsic AE activity from the cyclic apparatus. The AE equipment was the Physical Acoustic Group AEDSP-32/16B acquisition and processing hardware with the Mistras-2000 data acquisition software. A Physical Acoustic Group R15 transducer with the frequency range from 100 to 1000kHz was attached to a stainless steel cone. The cone acted as a transition from the transducer diameter to the Pt-wave guide with a diameter of 1mm. This 80cm wave-guide was necessary for this application because of the incompatibility of the transducer and the high temperatures in the furnace. A schematic of this setup is shown in Figure 17. During data

acquisition, a 40dB preamp and a band pass filter of 100 to 400kHz respectively were applied to the transducer signal. Figure 18 depicts a simplified acoustic emission signal from an event. This curve shows the typical increase in amplitude with time to the maximum amplitude through the duration of the rise time followed by the slow ring down to the end of the waveform. Once the signal crosses the threshold amplitude, digital recording of the waveform is started and continues until the amplitude drops below the threshold value. A maximum recording duration of 5000μs is imposed on all waveforms and any event exceeding this duration will not be completely recorded. There is also a time-out limit after a truncated event when no recording occurs until the amplitude drops below the threshold for 1000μs. This shows the limitation on the data acquisition capabilities but one needs to be cautious since events occurring during the time-out period will not be recorded. A number of parameters from these recorded waveforms are used to describe the event. These include: (1) time to peak amplitude, rise time; (2) peak amplitude: (3) duration of the event and (4) the number of peaks that cross the threshold value, referred to as "counts." The most descriptive parameter is acoustic energy (E^{AE}). E^{AE} is calculated by integrating the square of the event signal over the duration as shown graphically in Figure 19 and is sensitive to the amplitude and duration of the event. This parameter with the dependence on the squared amplitude and duration provides the opportunity to approximate the energy of the event.

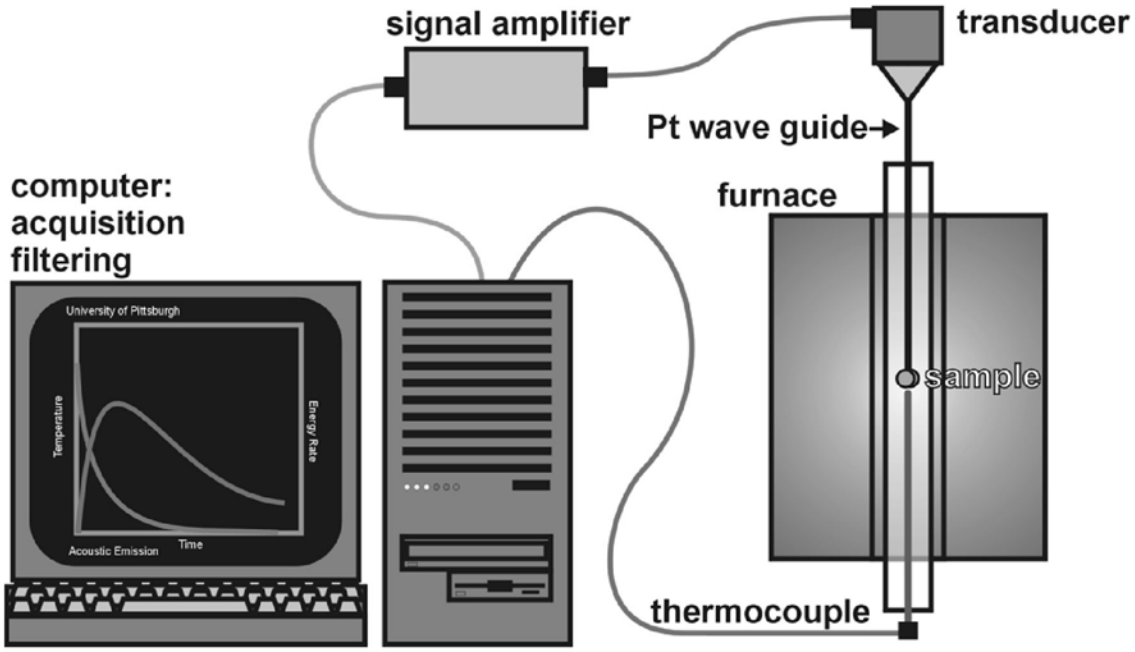

Figure 17. Schematic diagram of the acoustic emission equipment and furnace setup used in this investigation.

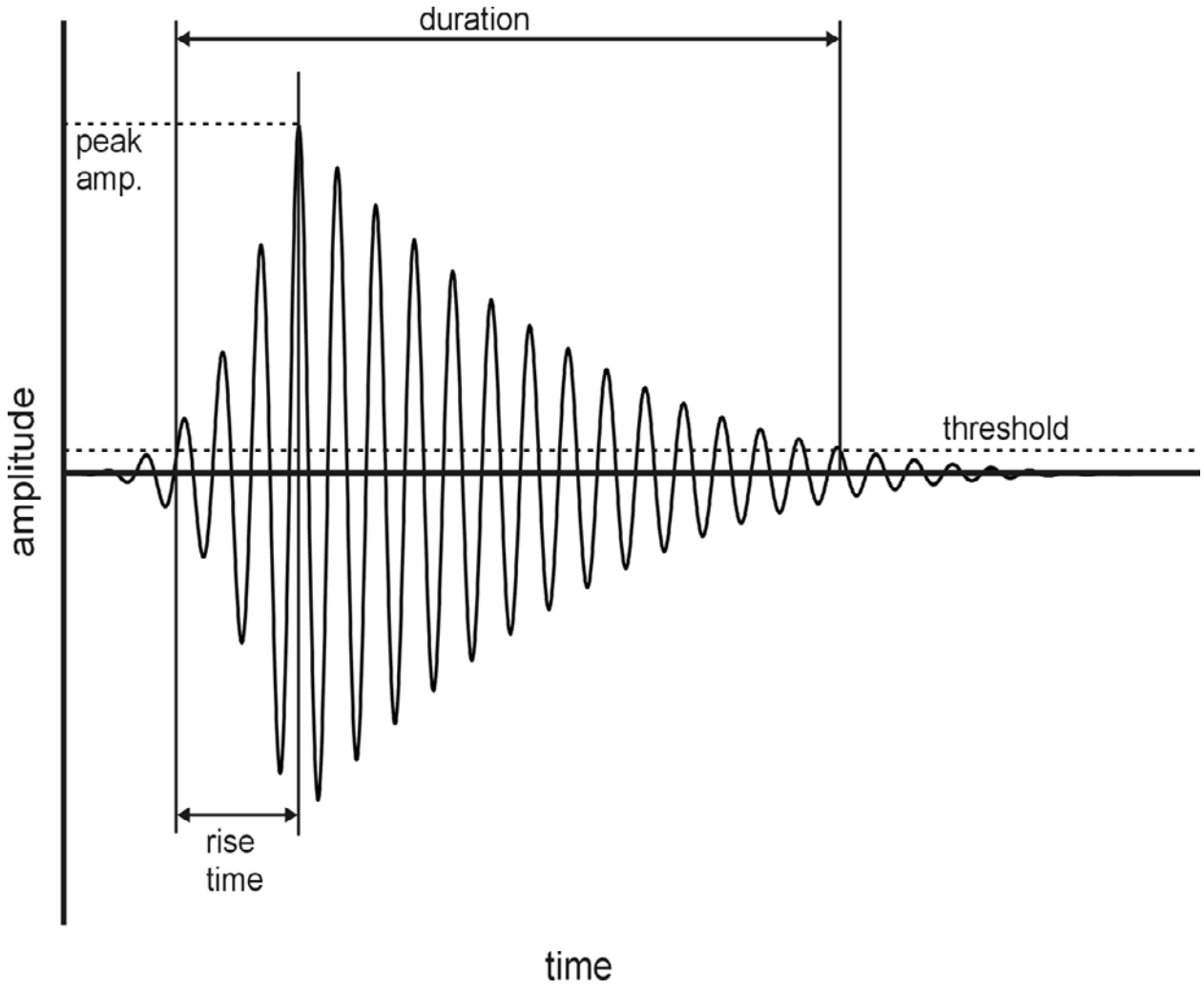

Figure 18. Plot of a typical acoustic wave and representation of important parameters.

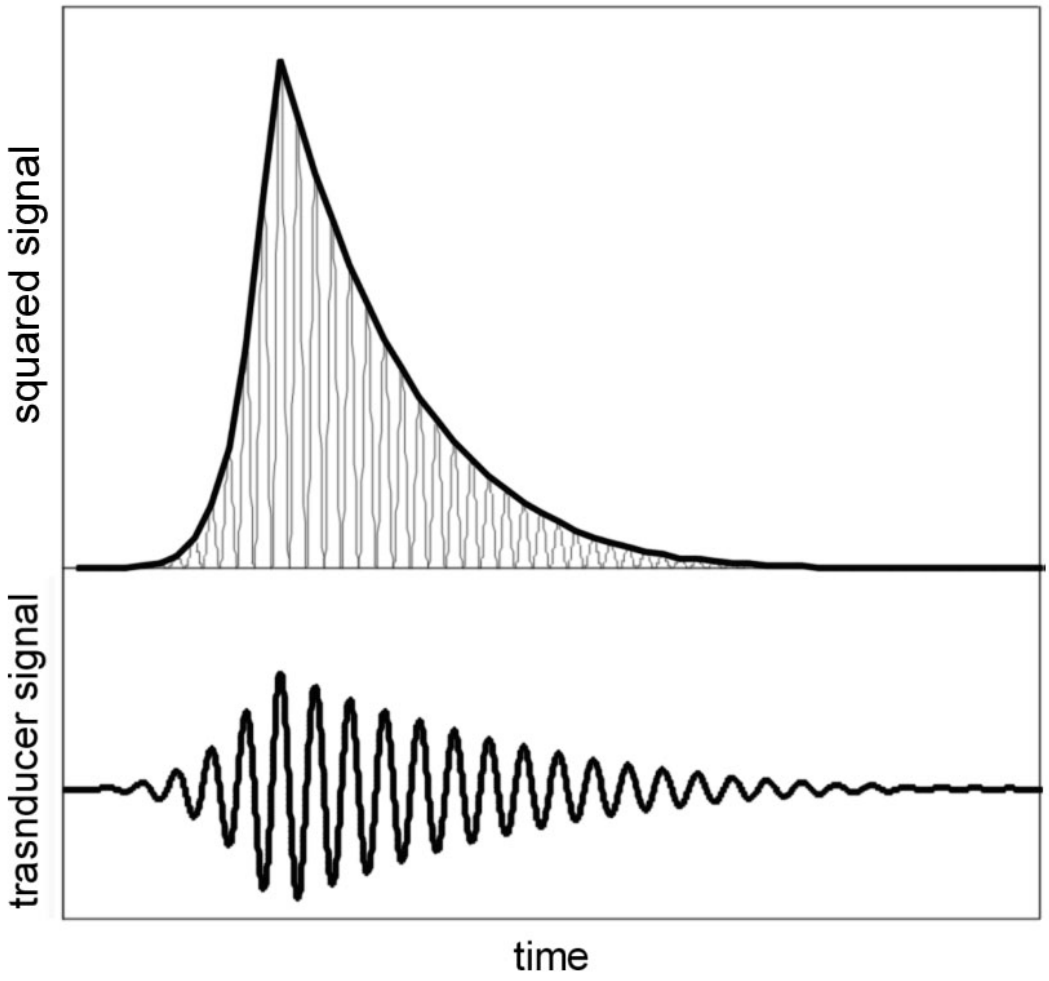

Figure 19. Graphical representation for calculating the E^{AE} (area under the top curve) for a typical acoustic wave (bottom curve).

The event of concern is fracture in the oxide scale and AE techniques provide a tool to quantify these events. This event is the cracking and spallation of the oxide scale that releases the stored elastic strain energy of the compressed scale and a portion of this energy is manifested as a mechanical elastic wave. A concept commonly used in seismology is the linear relationship between the energy manifested in the elastic wave as a result of the energy released from the fracture event[57]. This relation is

$$E_{elastic-wave} = \eta E_{Total} \tag{23}$$

where $E_{elastic-wave}$ is energy transported in the elastic-wave and E_{Total} is the total energy released from the event and η is a constant. Furthermore, the amplitude of the propagating elastic wave, A, is related to the energy transferred by the mechanical wave as

$$A^2_{elastic-wave} \propto E_{elastic-wave} \tag{24}$$

This amplitude of the elastic wave is detected as displacement at the surface of the specimen or waveguide and the AE transducer translates this displacement into a voltage signal by

$$V \propto u \tag{25}$$

where V is the voltage from the transducer and u is the displacement from the elastic wave. Equation (25) is a simplified version of the converse piezoelectric effect where [58]

$$\varepsilon_{jk} = d_{ijk} E_i \tag{26}$$

E_i is the electric field generated from the displacement, ε_{jk} is the induced strain and d_{ijk} is the converse piezoelectric constants.

As mentioned above, the energy of the elastic wave is linearly related to the square of the voltage from the transducer signal. From this formulation, an assumption that the energy released from the fracture event is linearly related to the E^{AE}. Independent work on this parameter adds empirical proof to the relationship of E^{AE} to the fracture energy. In one study, the fracture energy of breaking boron particles of various size was calculated and related to the measured E^{AE}. The fracture was achieved by uniaxial tension of an aluminum matrix with a boron particle dispersion. The sizes of the particles were varied to provide a range of fracture energies for detection by the acoustic emission equipment, and this relationship as shown in Figure 20a[59]. Another study that produced the same relationship used mortar specimens which were fractured in four point bend tests. Calculated fracture energies were readily available with the use of a standard fracture experiment and were related to the measured E^{AE} as shown in Figure 20b[60]. These studies have demonstrated that

$$E^{AE} = B \cdot \Gamma \tag{27}$$

where Γ is the fracture energy of the event and B is the proportionality constant. Equation 27 shows that the energy of a fracture event can be quantified by an AE technique.

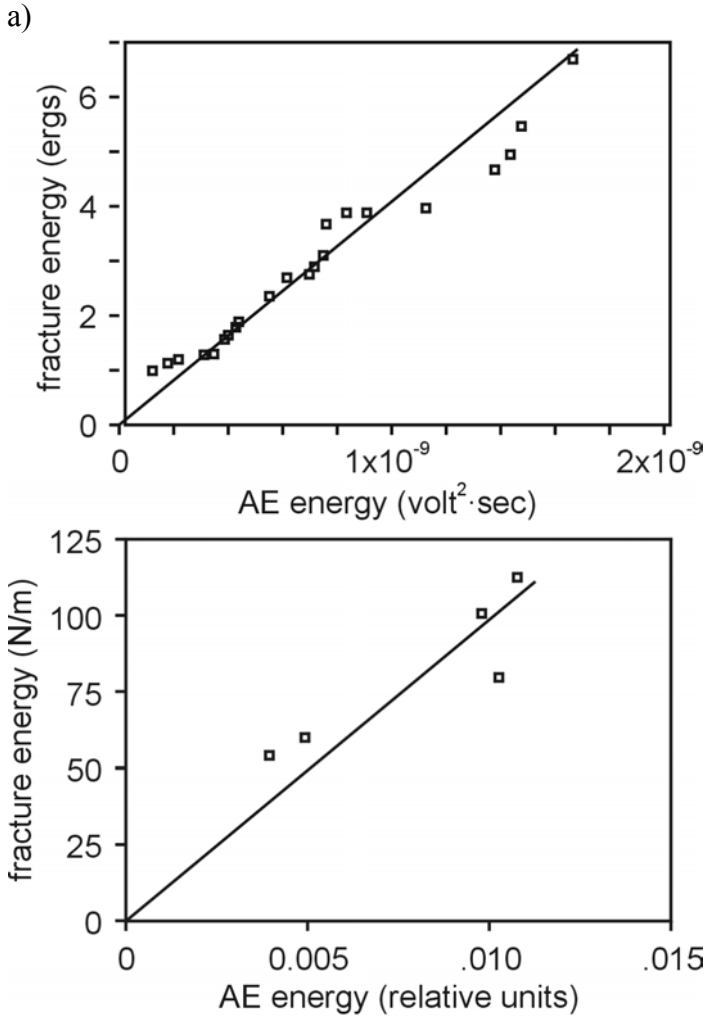

Figure 20. Plots of fracture energy exhibiting a linear relation to the measured acoustic energy (E^{AE}) from the fracture event for a) the uniaxial tension failure of boron particles in an aluminum matrix[59] and b) four point bend test of mortar[60].

For the case of spallation of a thin film on a substrate at least a few orders of magnitude thicker, the fracture energy associated with spallation can be approximated as

$$\Gamma_{spall} = V_{spall} \cdot \Omega_{ox} . \tag{28}$$

This fracture energy associated with the spallation of an oxide, Γ_{spall}, is the release of all the stored elastic strain energy, Ω_{ox}, in the volume of spalled oxide, V_{spall}. Detection of this fracture event by acoustic emission equipment has the capability to quantify the amount of oxide that spalls with known parameters Ω_{ox} and B. Determining the experimental proportionality constant, B, will be discussed in the next section, but Ω_{ox} is obtained from the following. For a thin film in biaxial compression, the stored elastic strain energy Ω is related to the biaxial stress as

$$\Omega = \frac{(1-\nu)}{E}\sigma_o^2 \tag{29}$$

This provides the stored energy per volume of stressed oxide. Adding the thickness of the scale into Equation (29) produces

$$\Omega' = \frac{(1-\nu)h}{E}\sigma_o^2 \tag{30}$$

where Ω' is the stored elastic strain energy per unit surface area. This equation also shows that the driving force for interfacial spallation increases with the thickness of the oxide scale and in the case of fracture along the metal–oxide interface with spallation, the energy released is proportional to the size of the spalled area.

4.4 XRD

4.4.1 Phase Identification

X-ray diffraction (XRD) was used for phase analysis of the thermally grown oxide scales that form on the alloys and coatings. Two Philips X'Pert diffractometer systems were utilized for these XRD measurements and this experimental equipment is illustrated in Figure 21. Both are $\theta - 2\theta$ machines where the x-ray source is fixed, the specimen is rotated through the angle θ and the detector is rotated 2θ. Also each diffractometer utilizes a Cu anode target, wavelength of 1.514Å and is operated at 40kV and 30mA. One is equipped with an open eulerian cradle that allows additional rotation of ψ (tilt) and ϕ (rotation) angles. Accommodating this deviation from true symmetrical diffraction where the sample surface is tilted ψ, the Cu target is oriented for a point source (round beam) and the detection system is comprised of a parallel beam collimator, flat graphite monochromator and proportional counter. This configuration is used for phase identification, residual stress measurements and texture analysis. The other machine is equipped with either a simple cradle or an Anton Paar resistance heated Pt strip high temperature stage. The target in this system is oriented for a line source and there is a choice of detection systems on this setup. The detection systems are a proportional counter with either a receiving

slit for symmetrical diffraction or a parallel beam collimator with a graphite monochromator for fixed incident and rocking diffraction geometries. Only sample rotation through the angle theta is possible which limits this configuration to phase identification and high temperature stress measurements.

a)

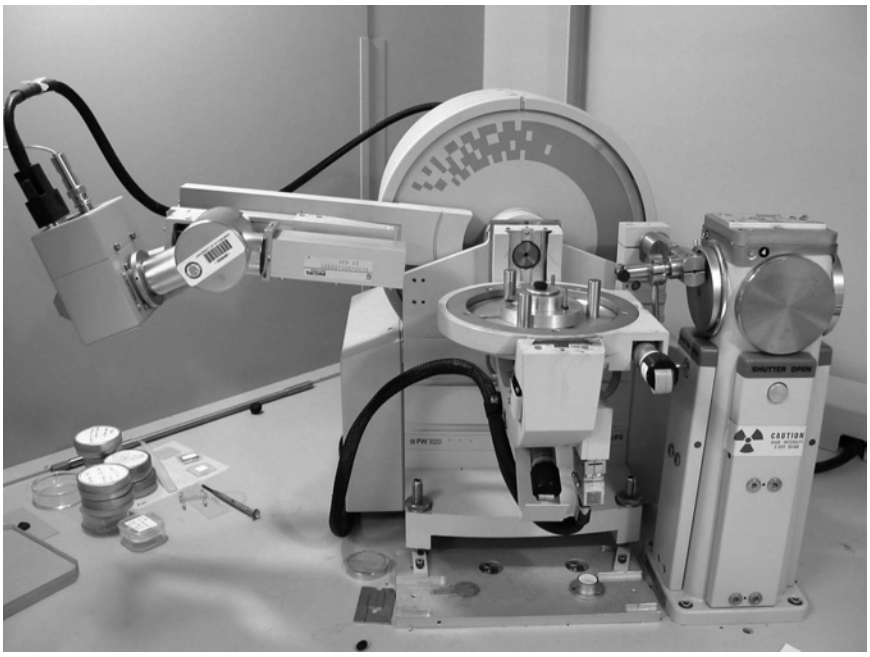

b)

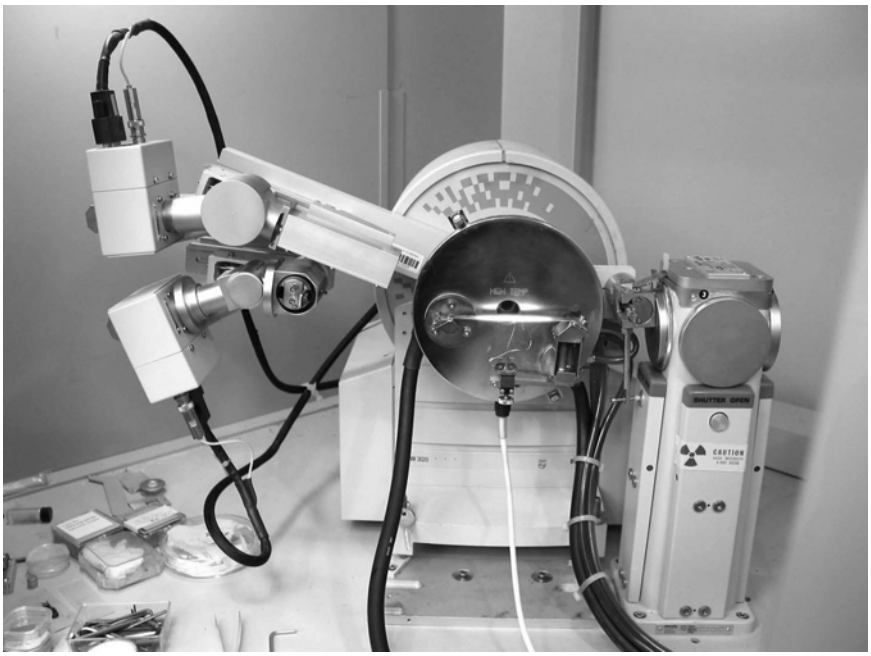

Figure 21. Images of XRD diffractometers used in this investigation where a) has the goniometer with open eulerian cradle and b) has the hot stage and two detector setup.

4.4.2 Stress Measurements

As previously described in the background, XRD stress measurements are carried out by measuring the displacement of *$d_{(hkl)}$-spacing* as a function of the tilt angle ψ , the angle between the plane normal and the surface normal of the specimen. The d-spacing of the (hkl) is obtained from Bragg's Law,

$$\lambda = 2d_{(hkl)} \sin\theta_B \tag{31}$$

where λ is the x-ray wavelength, $d_{(hkl)}$ is the (hkl) spacing and θ_B is the Bragg angle. This ability to measure $d_{(hkl)}$ in a diffractometer and record the change as a function of direction within a material provides a powerful tool to calculate stresses. For a biaxial stress state, the strain for a particular tilt, ε_Ψ , can be expressed in terms of measured plane spacing d_ψ and the unstressed spacing d_o [61] as

$$\varepsilon_\Psi = \frac{d_\Psi - d_0}{d_0} = \tfrac{1}{2} s_2(hkl)\sigma_o \sin^2\psi + 2s_1(hkl)\sigma_o . \tag{32}$$

In this classic equation, the dependence of d_ψ on the biaxial stress state and the x-ray elastic constants (XECs), $2s_1$and $\frac{1}{2}s_2$, are shown. With Equation 32, one needs only to measure d_ψ at one tilt angle to determine the stress with known x-ray elastic constants. This 1-point method incurs large uncertainties since the errors in measuring the stressed and unstressed d-spacings

can be on the same order of magnitude as the difference between them. Furthermore, a small error in determining d_o of less than a percent can result in large errors, >25%, in a calculated strain. By this method, these large errors can be difficult to resolve but this dependence on $d_\Psi - d_o$ can be eliminated by rewriting the above equation as

$$d_\psi = \tfrac{1}{2} s_2 \cdot \sigma_o \cdot d_o \cdot \sin^2\psi + d_o\left(2s_1 \cdot \sigma_o + 1\right) \tag{33}$$

where the d_ψ versus $\sin^2\psi$ relation is established. In the multipoint method, a number of d_ψ values are measured over a range of tilt angles and from this data, a d_ψ versus $\sin^2\psi$ plot can be constructed. Referring to Equation 33, one can see that the slope of this plot is

$$\text{slope} = \tfrac{1}{2} s_2 \cdot \sigma_o \cdot d_o \tag{34}$$

Although d_o is still used to calculate the stress in this equation, the contribution to error in stress calculation from d_o is much smaller than the experimental errors in determining the slope.

Another benefit of using the multipoint method is only one of the XEC, $\frac{1}{2}s_2$, is required. Two models have been proposed to average the response of the hexagonal alpha-alumina grains to the average stress. Both models assume a random distribution of crystal orientations. The Voigt model assumes that the all grains are subjected to identical strains and the following relation exists[62] for hexagonal crystals

$$\tfrac{1}{2}s_2 = \frac{15}{7C_{11} + 2C_{33} - 5C_{12} - 4C_{13} + 12C_{44}} \tag{35}$$

where the C_{ij} are the single crystal elastic constants of stiffness for alumina. Values for elastic stiffness are listed in Table 2[63]. The other, the Reuss model, assumes a uniform stress in all grains. For the Reuss model, two versions have been previously used. The first version[64] uses five single crystal compliance values of a hexagonal crystal in

$$\begin{aligned}\tfrac{1}{2}s_2(hkl) = {} & \tfrac{1}{2}(2S_{11} - S_{12} - S_{13}) - \tfrac{1}{2}(5S_{11} + S_{33} - 3S_{44} - S_{12} - 5S_{13})a_{33}^2 \\ & + \tfrac{3}{2}(S_{11} + S_{33} - S_{44} - 2S_{13})a_{33}^4\end{aligned} \tag{36}$$

where S_{ij} are the compliance constants for single crystal alumina, values calculated from C_{ij} listed in Table 2. The second version utilizes all six published compliance values[65] and the relation is

$$\begin{aligned}\tfrac{1}{2}s_2(hkl) = {} & \tfrac{1}{2}(2S_{11} - S_{12} - S_{13}) - \tfrac{1}{2}(5S_{11} + S_{33} - 3S_{44} - S_{12} - 5S_{13})a_{33}^2 \\ & + \tfrac{3}{2}(S_{11} + S_{33} - S_{44} - 2S_{13})a_{33}^4 + 3S_{14}a_{22}a_{33}(3a_{11}^2 - a_{22}^2)\end{aligned} \tag{37}$$

Values for $\frac{1}{2}s_2$ are plotted in Figure 22 against the angle between the (hkl) plane normal and the c-axis of the hexagonal crystal. In Table 3, values of the above models are calculated for all of the allowed reflections for alpha-alumina according to JCPDF 10-0173.

Table 2. Elastic constants for single crystal α-alumina.

Compliance (GPa^{-1})		Stiffness (GPa)	
S_{11}	2.35E-03	C_{11}	498
S_{12}	-7.10E-04	C_{12}	163
S_{13}	-3.68E-04	C_{13}	117
S_{14}	4.91E-04	C_{14}	-23
S_{33}	2.17E-03	C_{33}	502
S_{44}	6.94E-03	C_{44}	147

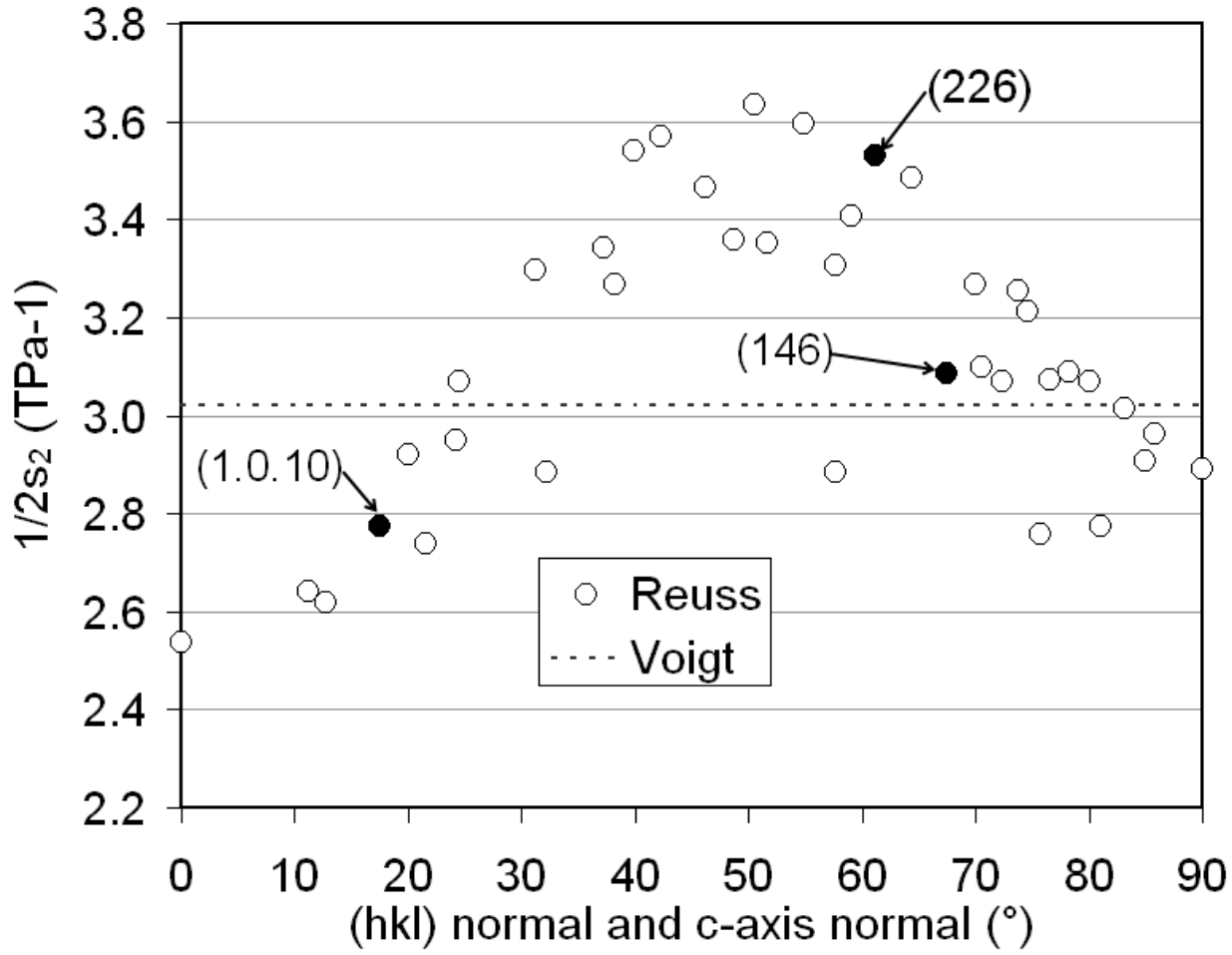

Figure 22. Plot of calculated X-ray elastic constants for α-alumina. Open circles are for diffracting α-alumina planes and closed are the (hkl) planes used in stress measurements.

Table 3. Calculated X-ray elastic constants for diffracting hkl planes of α-alumina.

Plane			XRD	d-spacing	angle	½S_2 (TPa^{-1})		
h	k	l	Rel. Int.	(Å)	(w/ c-axis)	Reuss (w/o S_{14})	Reuss (w/ S_{14})	Voigt
0	1	0	75	4.1213	90.00	2.892	2.892	3.02
1	0	4	90	2.5509	38.24	3.269	3.269	3.02
1	1	0	40	2.3795	90.00	2.892	2.892	3.02
0	0	6	1	2.1652	0.00	2.536	2.536	3.02
1	1	3	100	2.0854	61.21	3.259	3.532	3.02
2	0	2	2	1.9642	72.40	3.069	3.069	3.02
0	2	4	45	1.7400	57.61	3.306	2.884	3.02
1	1	6	80	1.6014	42.30	3.323	3.570	3.02
2	1	1	4	1.5466	83.16	2.922	3.015	3.02
1	2	2	6	1.5148	76.51	3.002	3.072	3.02
0	1	8	8	1.5108	21.51	2.878	2.739	3.02
2	1	4	30	1.4045	64.38	3.209	3.487	3.02
3	0	0	50	1.3738	90.00	2.892	2.892	3.02
1	2	5	2	1.3360	59.06	3.289	3.408	3.02
2	0	8	4	1.2754	38.24	3.269	3.269	3.02
1	0	10	16	1.2390	17.50	2.776	2.776	3.02
1	1	9	8	1.2341	31.24	3.128	3.298	3.02
2	2	0	8	1.1897	90.00	2.892	2.892	3.02
3	0	6	1	1.1600	57.61	3.306	3.306	3.02
2	2	3	6	1.1472	74.64	3.032	3.213	3.02
1	3	1	2	1.1387	84.97	2.909	2.909	3.02
3	1	2	6	1.1258	80.02	2.955	3.069	3.02
1	2	8	4	1.1241	46.19	3.351	3.465	3.02
0	2	10	8	1.0989	32.23	3.151	2.885	3.02
0	0	12	4	1.0826	0.00	2.536	2.536	3.02
1	3	4	8	1.0782	70.61	3.100	3.100	3.02
2	2	6	14	1.0427	61.21	3.259	3.532	3.02
0	4	2	2	1.0176	80.99	2.944	2.775	3.02
2	1	10	12	0.9977	39.83	3.293	3.541	3.02
1	1	12	1	0.9854	24.46	2.956	3.071	3.02
4	0	4	4	0.9821	72.40	3.069	3.069	3.02
3	2	1	1	0.9430	85.84	2.903	2.962	3.02
1	2	11	1	0.9411	37.17	3.251	3.343	3.02
3	1	8	4	0.9347	54.86	3.333	3.595	3.02
2	2	9	4	0.9181	50.50	3.356	3.635	3.02
3	2	4	14	0.9078	73.77	3.046	3.256	3.02
0	1	14	4	0.9053	12.69	2.669	2.617	3.02
4	1	0	8	0.8993	90.00	2.892	2.892	3.02
2	3	5	1	0.8885	70.00	3.111	3.269	3.02
4	1	3	4	0.8806	78.27	2.977	3.090	3.02
0	4	8	2	0.8700	57.61	3.306	2.884	3.02
1	3	10	12	0.8582	48.66	3.358	3.358	3.02
3	0	12	4	0.8503	38.24	3.269	3.269	3.02
2	0	14	4	0.8461	24.24	2.950	2.950	3.02
1	4	6	22	0.8305	67.44	3.156	3.088	3.02
1	1	15	4	0.8138	20.00	2.838	2.919	3.02
4	0	10	11	0.8073	51.58	3.353	3.353	3.02
0	5	4	7	0.7989	75.76	3.014	2.759	3.02
1	0	16	14	0.7966	11.15	2.640	2.640	3.02
3	3	0	13	0.7932	90.00	2.892	2.892	3.02

With this theory and framework, a number of techniques are employed for obtaining d_ψ values. A schematic representation of these techniques is depicted in Figure 23. The simplest geometry is the tilting technique and the use of symmetrical diffraction. Here the sample is tilted by angle ψ about the S_2 axis and the d-spacing is measured for given tilt intervals. When the diffracted beam intensity is too low for thinner films, a fixed low incident angle is used to spread the incident x-ray beam over the surface of the sample to increase the diffracting volume ultimately increasing the diffracted beam intensity. In this technique, the sample does not rotate through the angle θ as the detector rotates through 2θ. As a result, the tilt angle ψ is a composite angle of ψ', the goniometer tilt angle about S_2 and the incident angle α from the relation

$$\cos\psi = \cos\psi' \cdot \cos\gamma \tag{38}$$

where

$$\gamma = \theta_B - \alpha \tag{39}$$

The major deficiency of this fixed incident geometry is the smaller range of ψ that is possible when compared to the symmetrical FIT technique. The limit is imposed on the minimum tilt angle which is 90°-($\theta_B + \alpha$) and as a result of the this limited range, the errors in the stress values are generally larger. Both the symmetrical tilting and FIT were used for residual stress measurements.

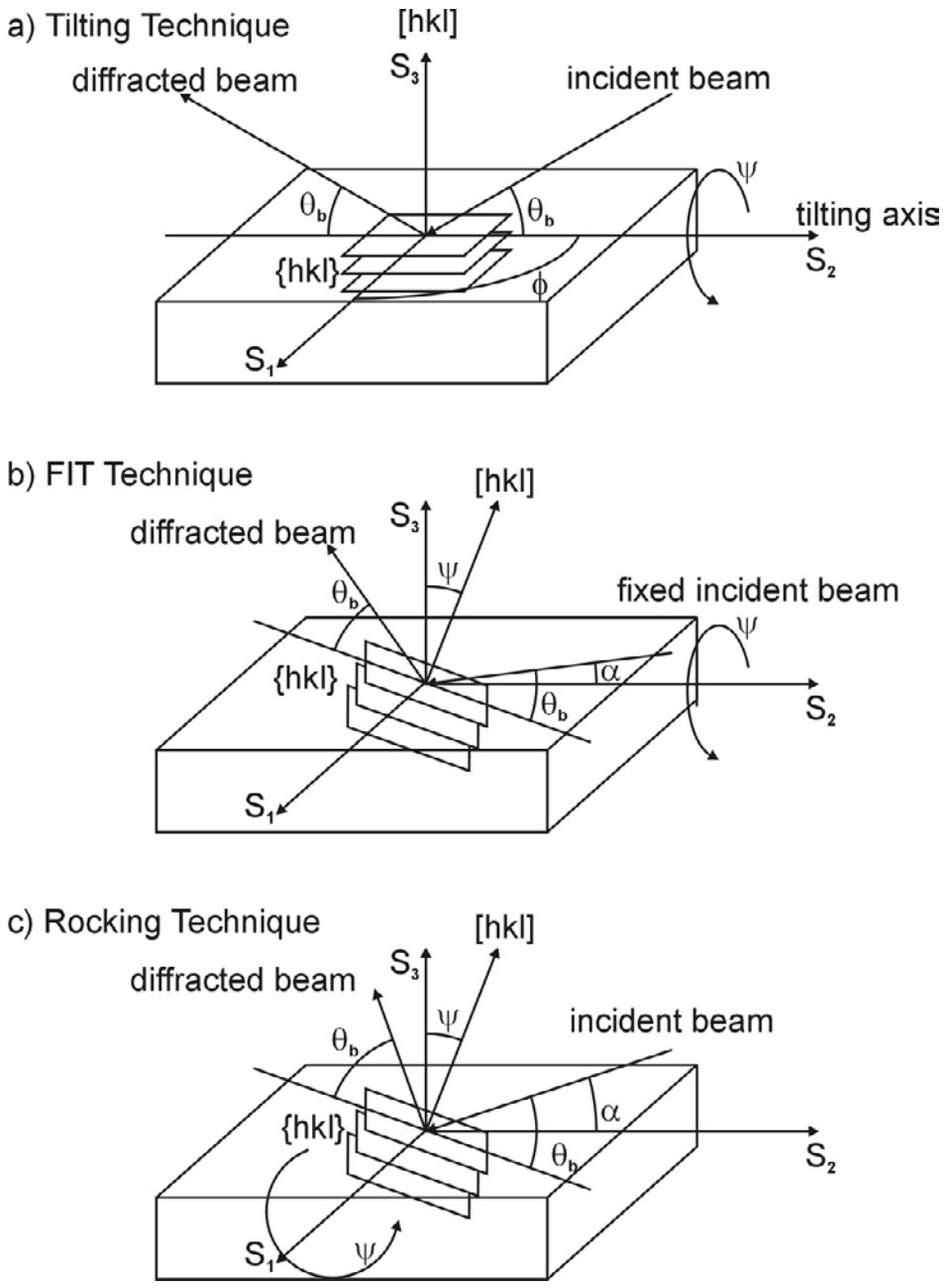

Figure 23. Schematic diagrams for the XRD stress measurement techniques: a) symmetrical tilting for residual stress measurement, b) fixed incident tilting (FIT) for residual stress measurement, and c) rocking technique for high temperature growth stress measurem

Measuring a growth stress in the oxide scale by an *in-situ* XRD technique is possible with the use of a high temperature stage. Specimen tilting about the S_2-axis cannot be achieved with this experimental apparatus because of the complicated heating and cooling equipment limiting stage mobility as shown in Figure 21b. The tilting required for stress measurements is achieved by rotating the specimen about the S_1-axis. This deviation from symmetrical diffraction is referred as specimen rocking and a schematic of this technique is depicted in Figure 23c. Although the sample is not tilted about the S_2-axis, as in the above techniques, a change in $d_{(hkl)}$ is still recorded with respect to the rocking angle or the effective ψ . As with the FIT technique, the range of tilt angles is not as large as the symmetrical tilting, but in this case, it is the higher tilt angles that are difficult to achieve since the limit for maximum tilt is the Bragg angle.

4.4.3 Error Calculation in XRD Stress Measurement

The experimental data from the XRD stress measurements areψ ,the independent, variable and the measured d_ψ , the dependent variable. Due to the assumed linear relationship in the d_ψ versus $\sin^2\psi$ plot, a least squares method is employed to derive this linear relationship as

$$\hat{d}_\psi = m \cdot \sin^2\psi + b\,. \tag{40}$$

In this equation, *m* is the calculated slope and *b* is the calculated intercept fitting the experimental data. $\hat{d}_\psi$ is the value calculated from this equation for a particular tilt angle, and should not be confused with the experimentally determined value d_ψ . The slope obtained from

the least squares method is then used to calculate the stress in the material, so any error in this slope is directly translated into error in the stress value. Determining the error in the slope is illustrated in the following. First, the variance of d_ψ , s_d^2 ,is calculated from

$$s_d^2 = \frac{\sum_i \left(d_{\psi i} - \hat{d}_{\psi i}\right)}{n-2}, \tag{41}$$

where *n* is the number of data points, or specific tilt angles used in the experiment and the numerator is the error sum of squares. This error sum of squares is the summation over *i* of the difference between the experimental data (d_ψ) and the values of $\hat{d}_\psi$ from Equation 40. This variance of d_ψ is then used in

$$s_m^2 = \frac{s_d^2}{\sum_i \left(\sin^2\psi_i - \overline{\sin^2\psi}\right)^2} \tag{42}$$

to calculate the variance of slope, s_m^2 , where values of ψ_i are the predetermined tilt angles and $\overline{\sin^2\psi}$ is the average of the squared sine of tilt angles used in the measurement. This variance of the slope of the regression line and a confidence interval are then used to apply an upper and lower bound to define an acceptable range as

$$m \pm t_{\alpha,n-2} \cdot s_m, \tag{43}$$

where $t_{\alpha,n-2}$ is the value describing the range of possible slopes or shape of the slope distribution. Values of $t_{\alpha,n-2}$ are dependent on *n* and α, the confidence level, and are generally obtained from t-distribution tables. This t-distribution is used rather than a normal distribution because of the small sample of tilt angles used in the stress measurements. The range of slopes determined by the above method is used to calculate a range of acceptable stresses that fit with a prescribed 80% confidence level.

4.4.4 Texture Measurements

The validity of the above methods for stress measurements depends on the random distribution of the grain orientation of the oxide scale. This random distribution is a requirement for the calculation of the x-ray elastic constants and necessary diffracted beam intensities. Since texture measurements are the comparison of intensities from a given (hkl), corrections are necessary for any phenomenon (other than grain orientation) that affects the diffracted beam intensity. Corrections required are: (1) background intensity subtraction, (2) shift in peak location (2θ) values as a function of tilt position (ψ); (3) defocusing of beam , geometrical considerations; and (4) a thin film correction (absorption correction).

For materials in biaxial compression (the usual case for thermally grown oxide scales), a shift of a peak to higher 2θ values is a result of tilting. Use of a single 2θ value will introduce a false drop in diffracted beam intensity. To correct this, a new 2θ value is used for a given ψ value.

Defocusing occurs at higher ψ values where the incident beam spreads over the surface of the sample. Since the incident x-ray beam has finite dimensions (width and height), the excited surface area increases with ψ as the beam spreads over the sample. This introduces a drop in the diffracted intensity. This effect is amplified by small or irregularly shaped samples, where the surface area is smaller than the area affected by the spread of the incident beam. To correct for this, intensities from a random sample of the same material, surface dimensions and orientation in the goniometer are acquired from a complete texture measurement. The correction is applied by

$$I_{\phi\psi}^{corr} = \frac{I_{\phi\psi}^{sample}}{I_{\phi\psi}^{random}} I^{average} \tag{44}$$

where $I_{\phi\psi}$ is the intensity for given ϕ and ψ values for the relative corrected (*corr*), measured sample (*sample*) and random sample (*random*) intensities[66]. The average intensity, $I^{average}$, is obtained by averaging all $I_{\phi\psi}^{sample}$ values. With this, any erroneous change from geometrical aspects can be corrected.

The final correction arises from an increase in diffracted intensity from thin films with respect to specimen tilt. Opposite to the effects from defocusing, as the sample is tilted, there is an increase in the diffracting volume from the oxide scale. Since the oxide scale thickness is smaller than the penetration depth of the incident x-rays, the area of excited surface becomes a limiting factor. At ψ equal to zero, the incident beam is at a maximum angle to the sample surface and as a

result, the excited surface area is at a minimum. Increasing ψ spreads the incident beam over the surface increasing the excited area and ultimately increasing in the diffracted intensity. The applied correction[67] is

$$I_t = I_\infty \left(1 - \exp\left(\frac{-2\mu \cdot t}{\sin\theta \cdot \cos\psi}\right)\right) \tag{45}$$

where μ is the mass absorption coefficient, t is the thickness of the scale, I_∞ is the diffracted intensity from a semi infinite thick layer and I_t is the intensity of the diffracted beam from the thin film.

4.5 MICROSCOPY AND ANALYTICAL

After high temperature exposure of the alloys and coatings, electron and optical microscopy were used to qualitatively describe the performance of the materials. The scanning electron microscope (SEM) used in this investigation was a Philips XL30 FEG (field emission gun). This SEM is equipped with secondary electron and back scattered electron detectors for imaging along with an X-ray detector for energy dispersive spectroscopy (EDS) for chemical analysis. For additional analysis, reflective light microscopy was employed for low magnification analysis. Within this optical technique, polarized light was utilized to image debonded sections of oxide scale that did not spall. Results and features obtained by microscopy were correlated to results obtained from acoustic emission and other oxidation testing.

5.0 RESULTS AND DISCUSSION

5.1 CYCLIC OXIDATION

The goal of this investigation is to use information from short-term tests to predict long-term cyclic oxidation behavior of the alloys and coatings listed in Table 1. Actual long-term test data for cyclic oxidation is necessary for the validation of the technique described in this section. These one hour thermal cycle oxidation tests were performed at 1100°C with 45 minutes in the hot zone and 15 minutes in the cool zone. Results for the superalloy LS N5 are shown in Figure 24. This behavior is typical for cyclic oxidation curves where the mass gain dominates at the early cycles. The contribution to oxide loss becomes apparent where the mass change reaches a maximum and increases as the specimen exhibits a net mass loss (crossover to negative weight change). The superalloy 1484 exhibited immediate weight loss as reported by Sarioglu et. al[68]. Aluminide coatings were cyclically oxidized and the results are shown in Figure 25. The St-Al coating was exposed to enough thermal cycles to produce the negative mass change, but after 2000 cycles, the Pt-Al coating has yet to exhibit a well defined maximum suggesting that mass loss by scale spallation is very low. FeCrAlY also displayed low mass loss when cyclically oxidized, and in an investigation by Stasik et. al.[69], FeCrAlY was exposed to 1600 cycles without cross over to negative mass change. Although the cross over point was not obtained, the FeCrAlY performance was not as good as the Pt-Al since a maximum mass gain was apparent at approximately 1200 cycles.

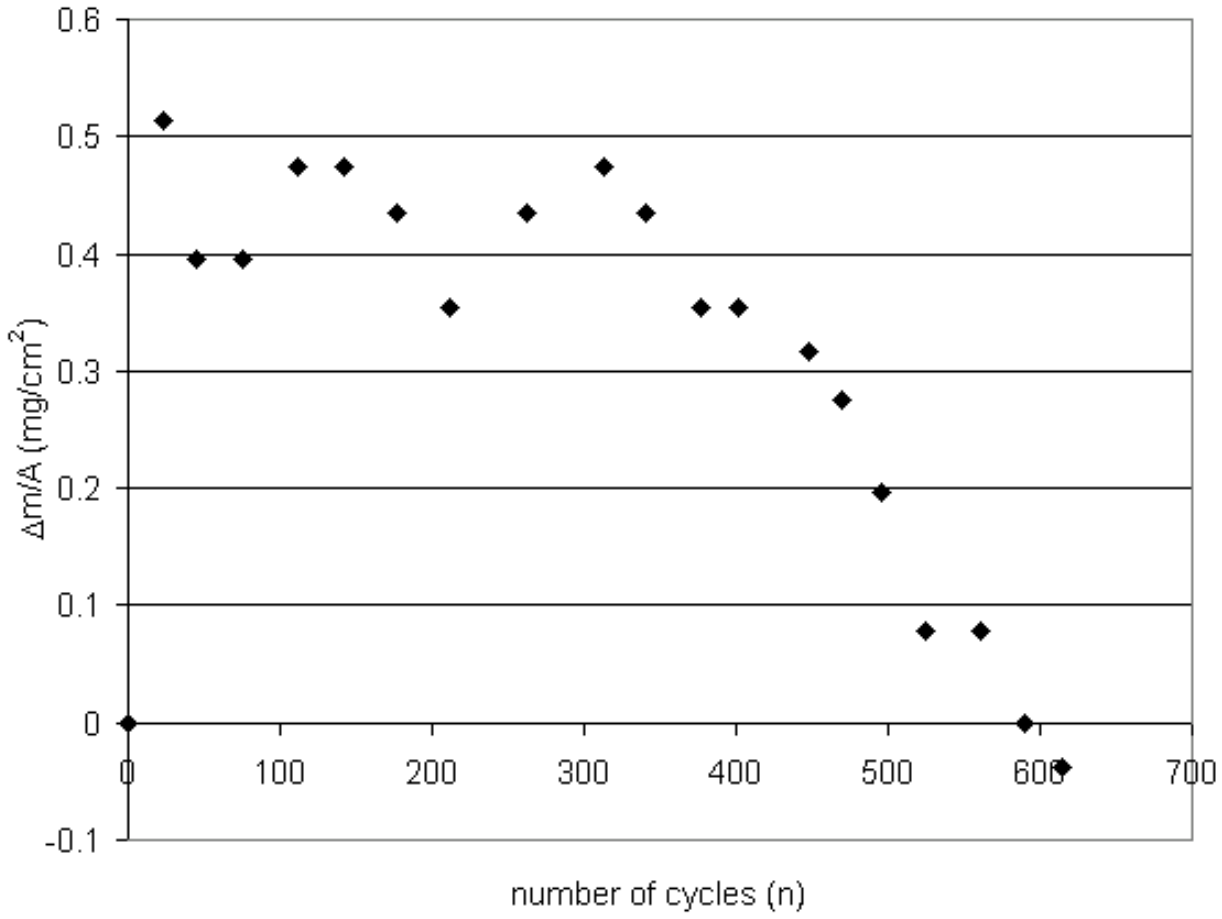

Figure 24. Cyclic oxidation plot for superalloy N5 exposed at 1100°C.

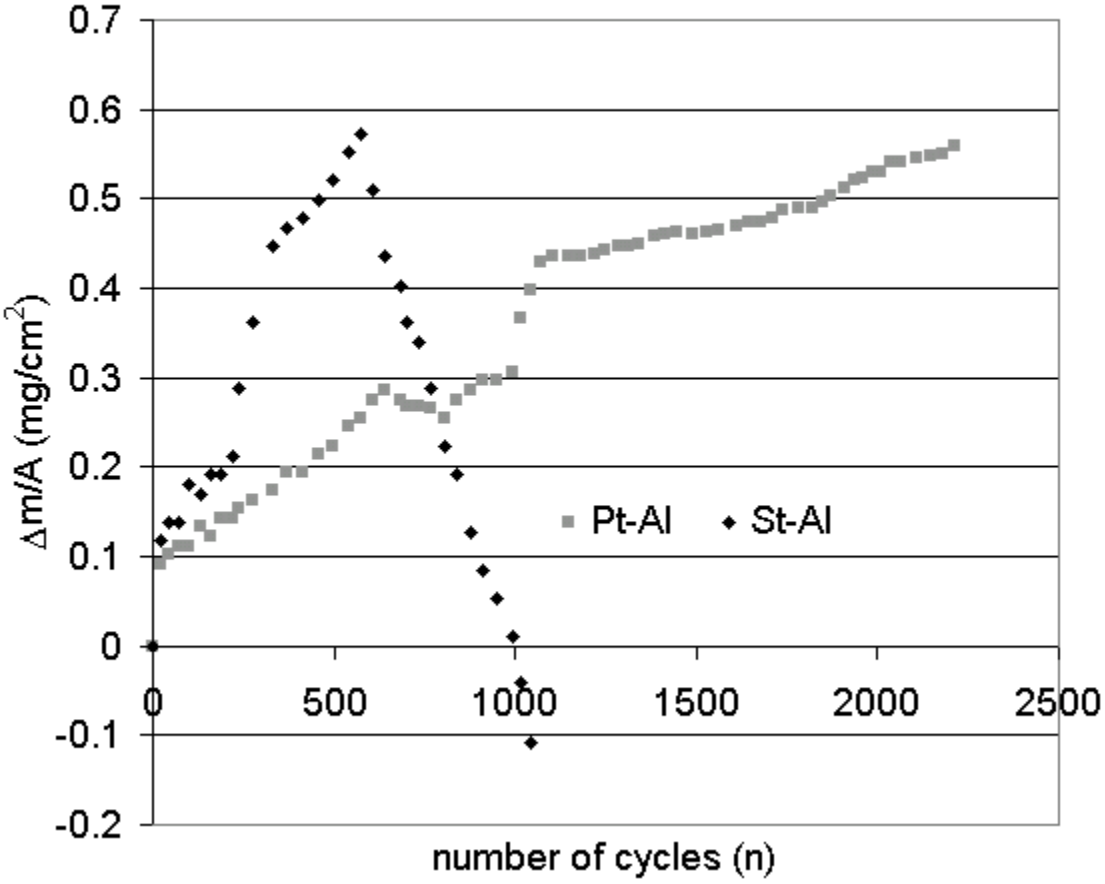

Figure 25. Cyclic oxidation plot for Pt and straight aluminide coatings on superalloy N5 exposed at 1100°C.

Figure 26 shows the cyclic oxidation results of duplicate nickel specimens. This experiment was not conducted to cross over to negative weight change because of an interesting phenomenon. The mass gain from cyclic oxidation is greater than the mass gain during isothermal oxidation and isothermal kinetics are included in Figure 26 and plotted against time at elevated temperature rather than number of cycles for a direct comparison. This result suggests that during thermal cycling, the protective oxide scale cracks and loses continuity over the surface. Nickel oxidation will progress faster in the locations of the through scale cracks accounting for the increase in oxygen uptake. In addition, this cracked oxide must not spall or a loss of mass would be apparent in the plot. Figure 27 presents two SEM surface micrographs of this oxide scale exhibiting tensile cracks to support this theory. This relaxation of thermal stresses during cooling can lead to the generation of a tensile stress and resultant cracks during heating[32].

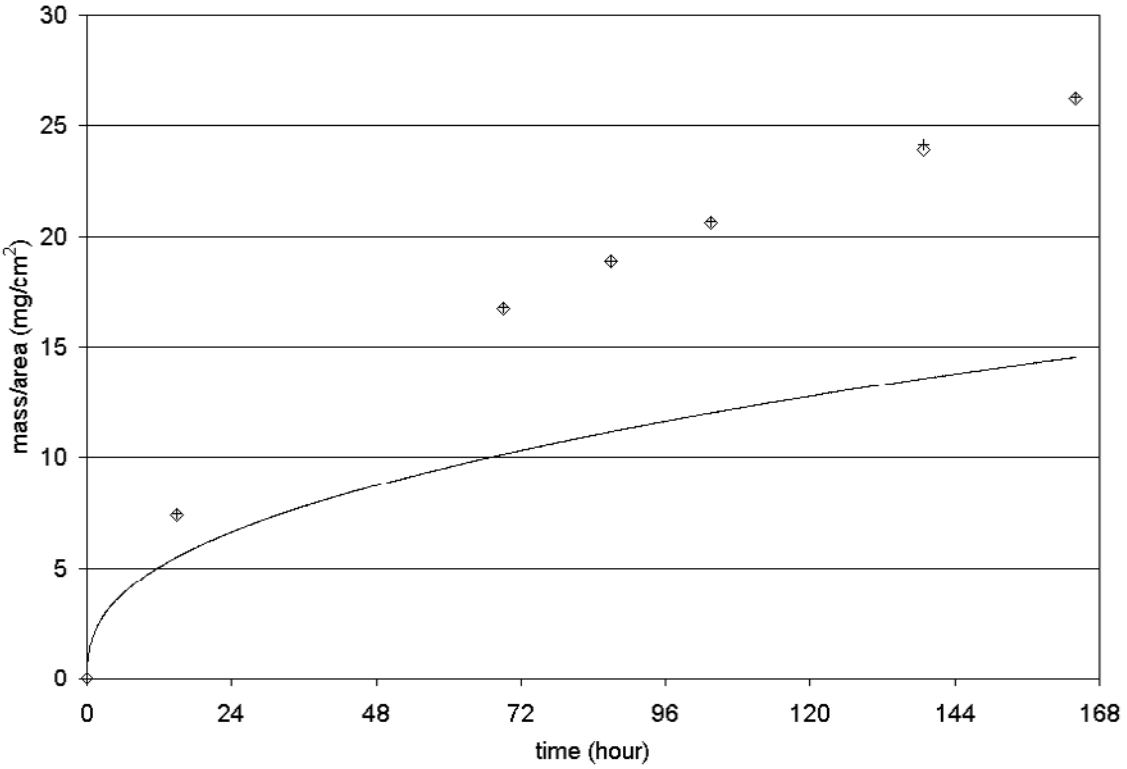

Figure 26. Cyclic oxidation plot for Ni (data points) exposed at 1100°C. The isothermal kinetics (solid line) is included for comparison.

a)

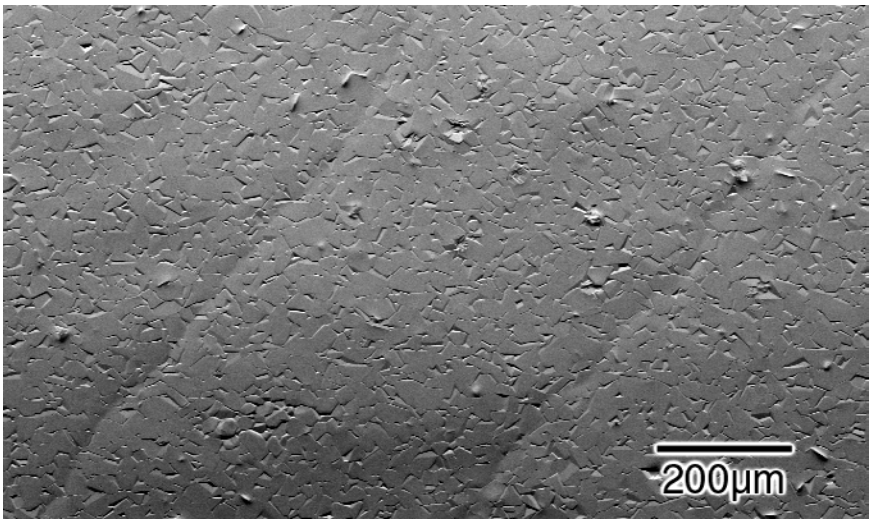

b)

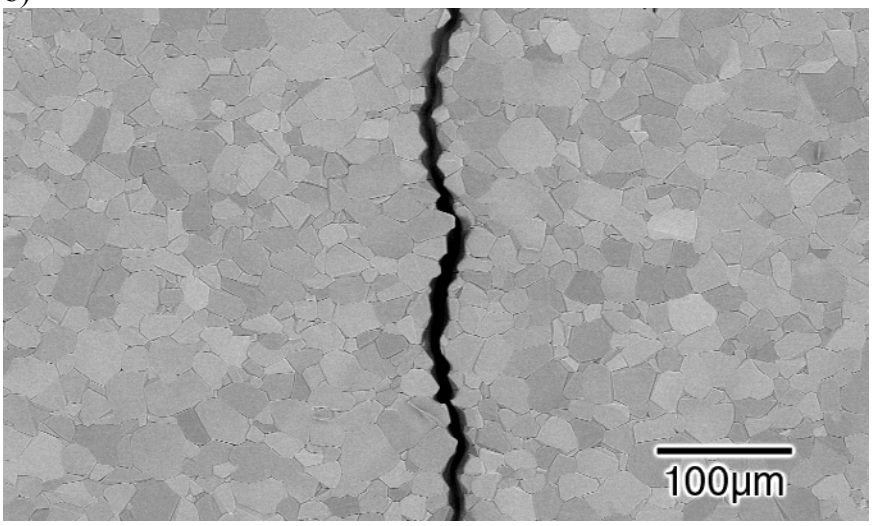

Figure 27. SEM surface micrographs of Ni after cyclic oxidation at 1100°C. Tensile cracks are apparent on the surface after this exposure.

A useful criterion to rate the cyclic oxidation performance is the time or number of cycles until the weight change of the specimen becomes negative. Other possible criteria could be used for determining the useful life of a material in a cyclic oxidation such as the maximum mass gain or the metal wastage rate, but for this investigation life-time is defined as the number of cycles to negative weight change. The number of cycles to negative weight change was used to represent cyclic oxidation life to directly compare long-term cyclic oxidation data to modeled data since this value was easily obtained from model calculations. Therefore, life-times for 1484, Low S N5 and Ni aluminide coating are respectively 24, 600 and 1000 cycles. Since the tests were terminated prior to negative weight change for FeCrAlY and Pt modified aluminide, the cyclic oxidation lives were obtained by extrapolation with values of 2000 and 4000 cycles respectively.

5.2 ISOTHERMAL OXIDATION

Cyclic oxidation curves provide information about scale growth and scale spallation by the change in specimen mass. Since both growth and spallation contribute to the mass change, interpreting cyclic oxidation curves from a fundamental aspect requires at least independent knowledge of one of the competing phenomena. The independent test universally accepted is an isothermal oxidation experiment used to measure the growth kinetics of the oxide scale. TGA data for isothermal oxidation in dry air are shown in Figure 28 for alumina formers. FeCrAlY has the fastest overall growth kinetics of the materials in this plot and was the only material to exhibit parabolic growth behavior. 1484 and LS N5 superalloys are grouped as the intermediate growth kinetics but did deviate from parabolic behavior in the initial oxidation[70]. This initial

rapid mass increase can be associated with the formation of transient oxides (nickel aluminate) and the effect is more severe for the 1484 as indicated by the largest initial mass gain. Both aluminide coatings are classified with the slowest kinetics in this collection of materials, hence the use of these coatings for oxidation resistance. The deviation from parabolic growth behavior of the scale formed on these coatings is a result of transient aluminum oxides that initially form[71]. These transient metastable aluminas grow faster than the stable α-alumina phase but once they transform to the stable α-alumina phase a slower growth rate is apparent. The isothermal oxidation of Ni demonstrates growth kinetics orders of magnitude faster than the alumina formers and these results are shown in Figure 29.

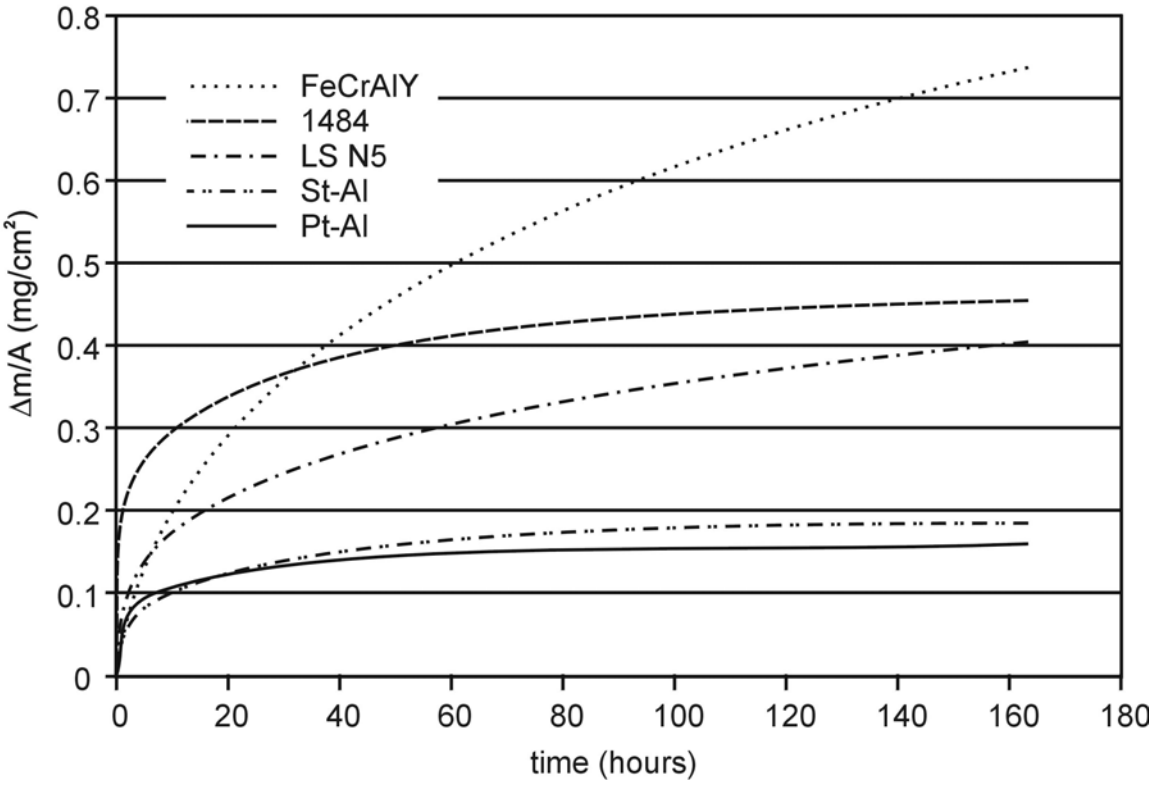

Figure 28. Plot of thermogravimetric results from isothermal oxidation of alumina forming alloys and coatings exposed at 1100°C in dry air. All curves are duplicated except for St-Al.

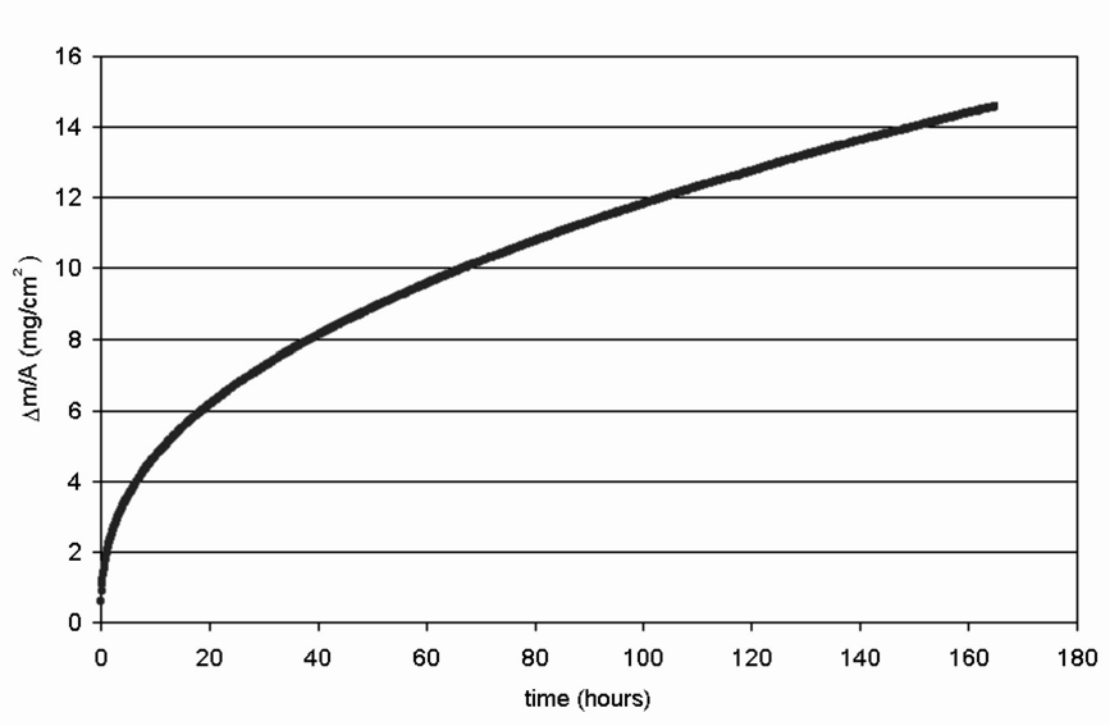

Figure 29. Plot of thermogravimetric results from isothermal oxidation of nickel exposed at 1100°C in dry air.

All of the TGA data in Figures 28 and 29 were duplicated except for the St-Al data. The purpose was to determine the accuracy of the method and validate these results since this data is critical for further model calculations. Additionally, this TGA data was compared to oxide scale thickness measurements. The same materials were exposed to 1100°C for 24 hours and metallographic cross sections were prepared for SEM thickness measurements. Low magnification micrographs of each alloy are shown in Figure 30, but the actual thickness measurements were performed at higher magnifications. Since these oxide scale thickness measurements were performed in the SEM, where the actual magnification is dependent on specimen height, proper focusing and calibration, one needs to consider a relative error of a few percent for these thickness values. Calculating the oxide thickness from TGA data requires converting the mass change (oxygen uptake) per surface area into total oxide mass per area according to oxide stoichiometry to compare with the SEM thickness data. This oxide mass is then converted into the scale thickness with a known oxide density. The density of alumina and NiO are 3.96 and 6.67 g/cm^3, respectively. Data from the SEM measured thickness and calculated thickness from TGA is listed in Table 4. There is good agreement between these two techniques except for the superalloys where mixed transient oxides complicate the result. The oversimplification of treating the entire scale thickness as only one type of oxide led to the discrepancy between the methods.

Table 4. Thickness of Oxide Scale after 24 hour exposure to 1100°C

material	24 hour mass change (mg/cm^2)	24 hour total oxide (mg/cm^2)	oxide thickness from TGA data (μm)	oxide thickness from SEM image (μm)
Pt-Al	0.12	0.26	0.64	0.86
S-AL	0.13	0.28	0.69	0.95
FeCrAlY	0.32	0.68	1.72	1.6
LS N5	0.23	0.49	1.19	1.9
1484	0.35	0.74	1.86	2.9
nickel	6.6	30.9	46.4	40

a) 1484

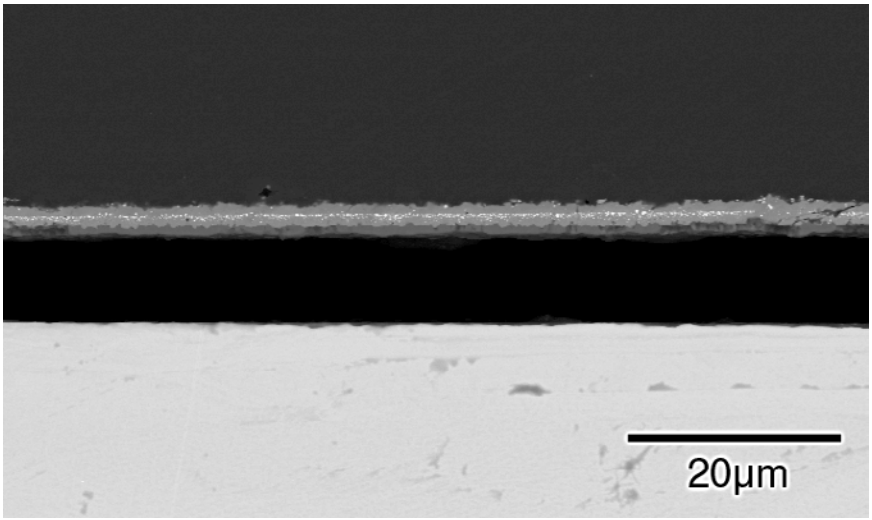

b) FeCrAlY

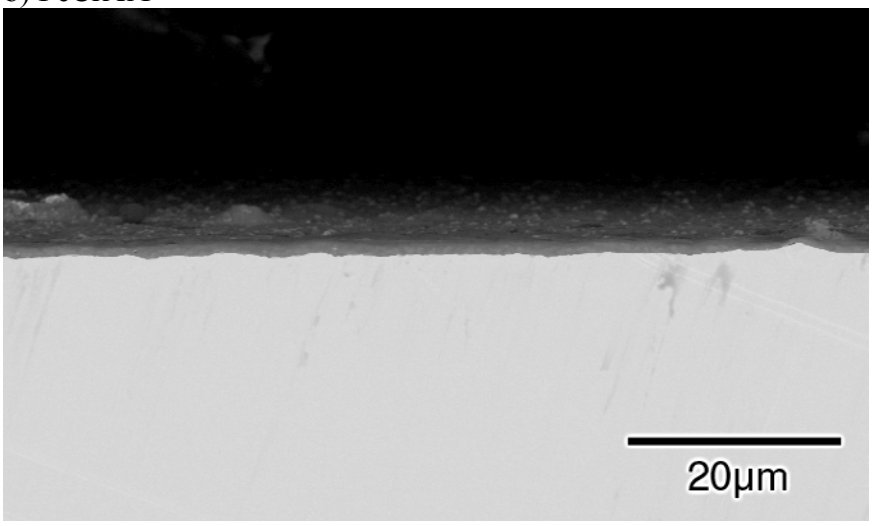

Figure 30. SEM cross section micrographs of alloys and coatings exposed at 1100°C for 24 hours. Thickness of each scale was measured from these images to compare to TGA data.

c) LS N5

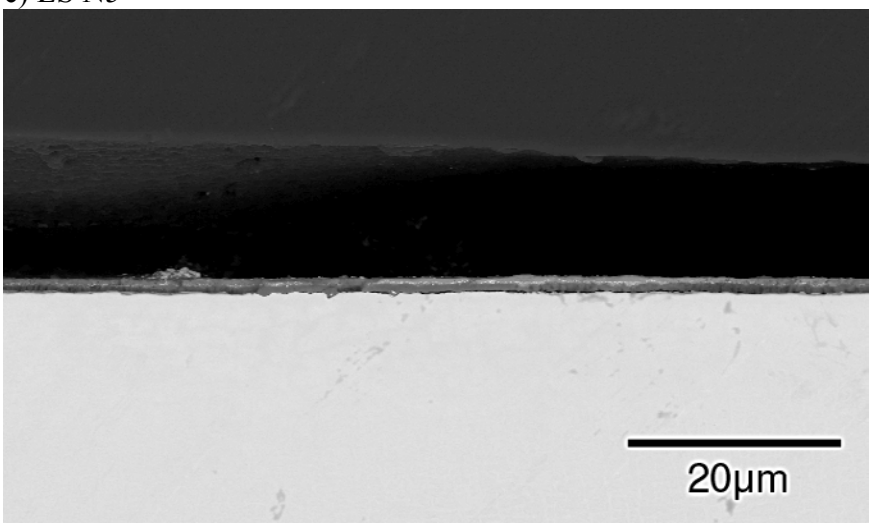

d) nickel

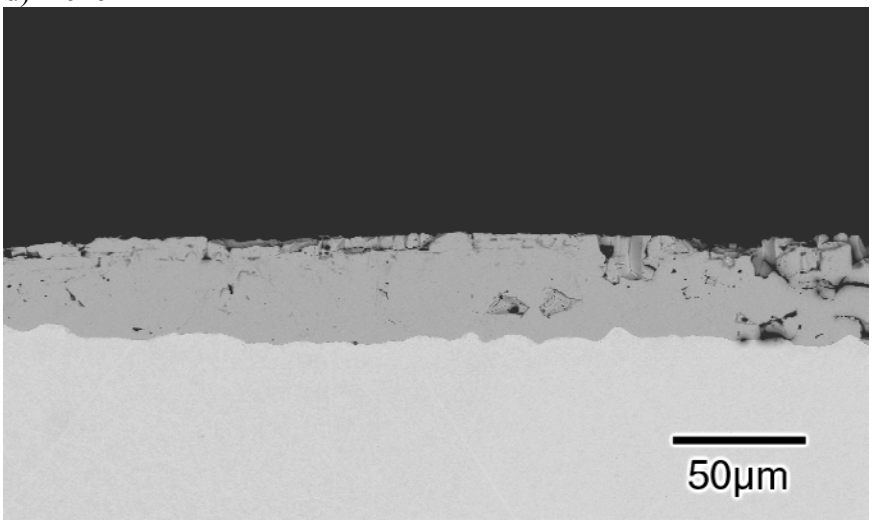

Figure 30 continued. SEM cross section micrographs of alloys and coatings exposed to 1100°C for 24 hours. Thickness of each scale was measured from these images to compare to TGA data.

e) Pt-Al

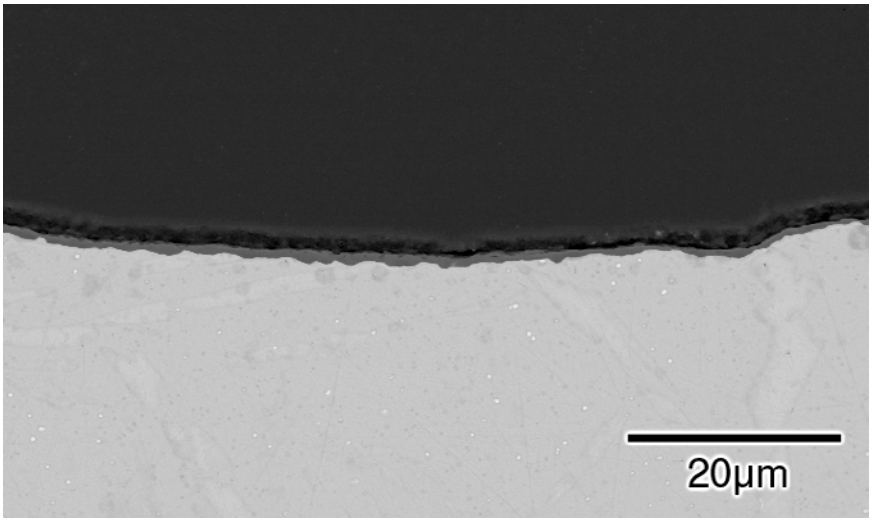

f) St-Al

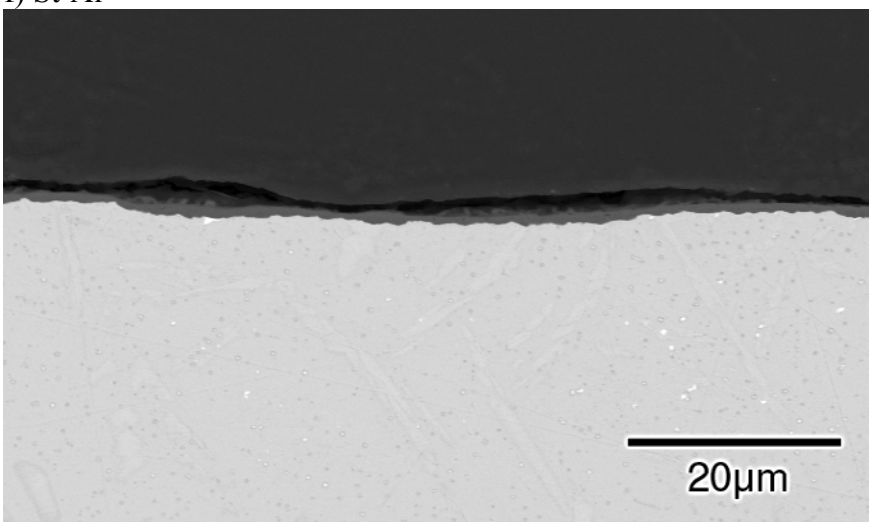

Figure 30 continued. SEM cross section micrographs of alloys and coatings exposed to 1100°C for 24 hours. Thickness of each scale was measured from these images to compare to TGA data.

5.3 CYCLIC OXIDATION MODELING

The COSP model has been developed to create cyclic oxidation plots similar to Figure 24 and 25 with known oxidation kinetics and spallation behavior during cooling for the thermally grown oxide. Since alumina scales usually crack and spall to the oxide-substrate interface, the Monte Carlo version of the COSP, which manages cracking and spallation in a similar method, was chosen for the rest of the modeling. To demonstrate the Monte Carlo version, a curve has been constructed for a hypothetical material with parabolic growth kinetics of those obtained from FeCrAlY oxidation in the isothermal TGA experiments. Therefore, the k_p is 0.066 $mg^2cm^{-4}h^{-1}$ but a hypothetical Qo of 0.00002 cm^2/gm is used to generate the curves in Figure 31. Each curve is constructed with a different number of surface segments. The average of 10000 segments produces a smooth curve yet the progress of each segment is apparent in the curve created with only 10 segments. The use of a large number of segments, generally around 10000, is necessary for reproducibility with the Monte Carlo COSP.

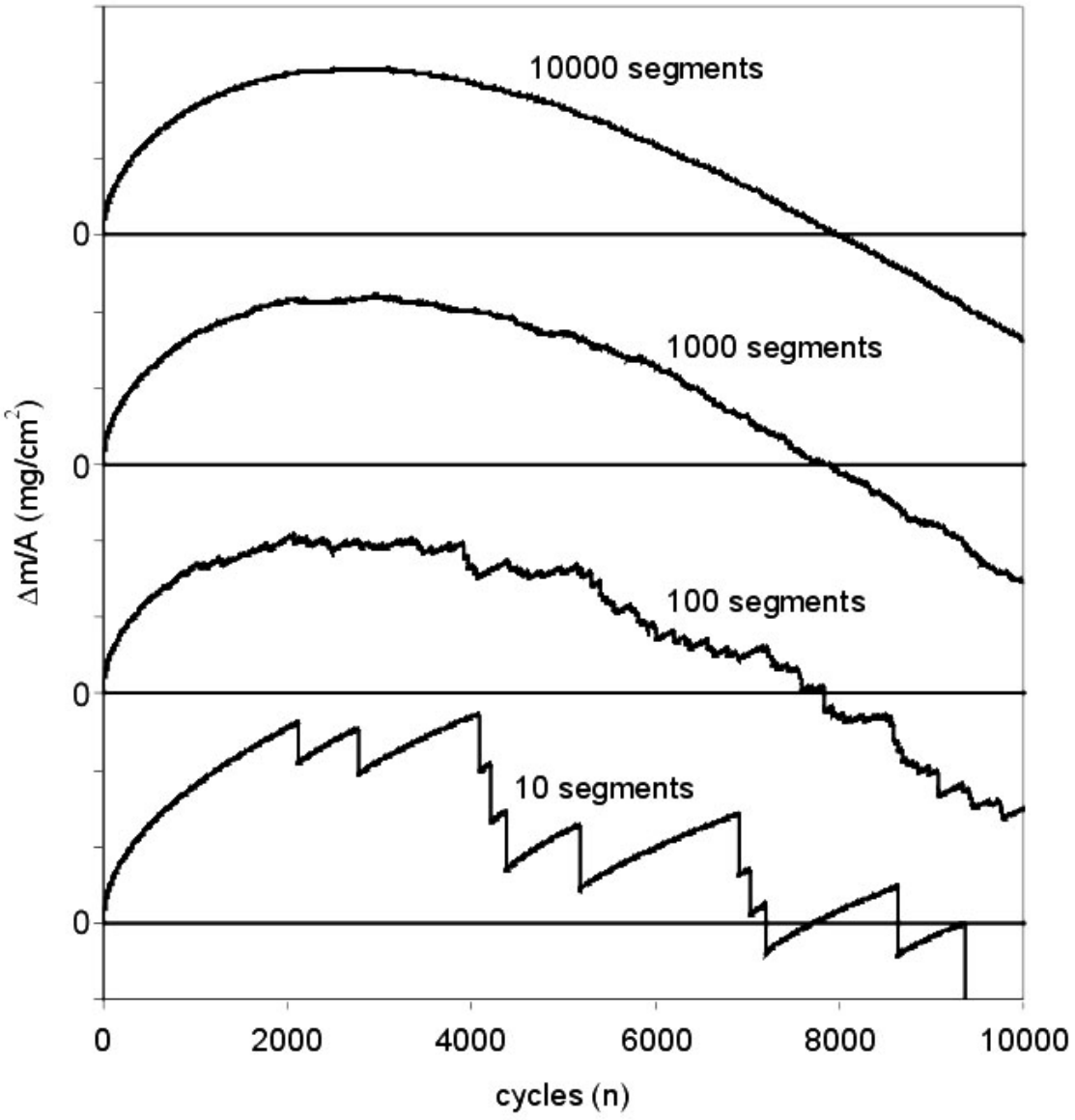

Figure 31. Plot of modeled cyclic oxidation curves for a hypothetical material exhibiting a k_p = $0.066 mg^2 cm^{-4} h^{-1}$ and $Q_o = 0.0000^2 cm^2 mg^{-1}$. Each curve was calculated for a different number of surface segments and as the number of segments increases, the smoothness and reproducibility of the curve.

The fundamental mechanisms utilized to generate the curves in Figure 31 are the same as those in operation in long-term cyclic oxidation experiments. Likewise, scale growth in the model results in the increase in mass of the sample during the initial oxidation cycles and when the spalling contribution is small. As the oxide thickens, the additional amount of oxide that forms during each cycle reduces due to the parabolic growth kinetics, but the amount of oxide lost per cycle begins to increase since the probability for spallation to occur is linearly related to the amount of oxide present. As the effect from oxide spallation becomes considerable, the slope of the curves in Figure 31 lessens and ultimately becomes negative. Finally, these two competing aspects during cyclic oxidation, oxide growth and oxide spallation, reach a steady state condition were the amount grown per cycle equals the amount that spalls. Once this condition is reached, the cyclic oxidation curve becomes linear with a negative slope.

For non zero values of Q_o, the weight change of the oxidizing material in the COSP will eventually become negative and a time to represent cyclic oxidation life can be obtained. Figure 32 shows the effect of Q_o on the modeled oxidation curves. The growth kinetics are those for the FeCrAlY (k_p = 0.066 $mg^2cm^{-4}h^{-1}$) and 10000 surface segments are used in the calculation of the curve for a range of Q_os. As Q_o is increased, the time to crossover (cyclic oxidation life-time) is decreased, the maximum mass gained is decreased and the final slope is more negative. The dependence of cyclic oxidation life on Q_o can be established for a material with known growth kinetics from a series of curves like those in Figure 32. A linear relation, or life-time curve, is observed when the log of cyclic oxidation life (cycles to crossover) is plotted against the log of Q_o. Figure 33 show a series of life-time plots for the alloys and coatings and the only

information needed for curve construction is the isothermal oxide scale growth kinetics. Each line is constructed on a per materials basis, where the faster growing scales result in curves shifted to the left. This plot presents a means for predicting cyclic oxidation lives for alloys and coatings if spall behavior (Q_o) is known.

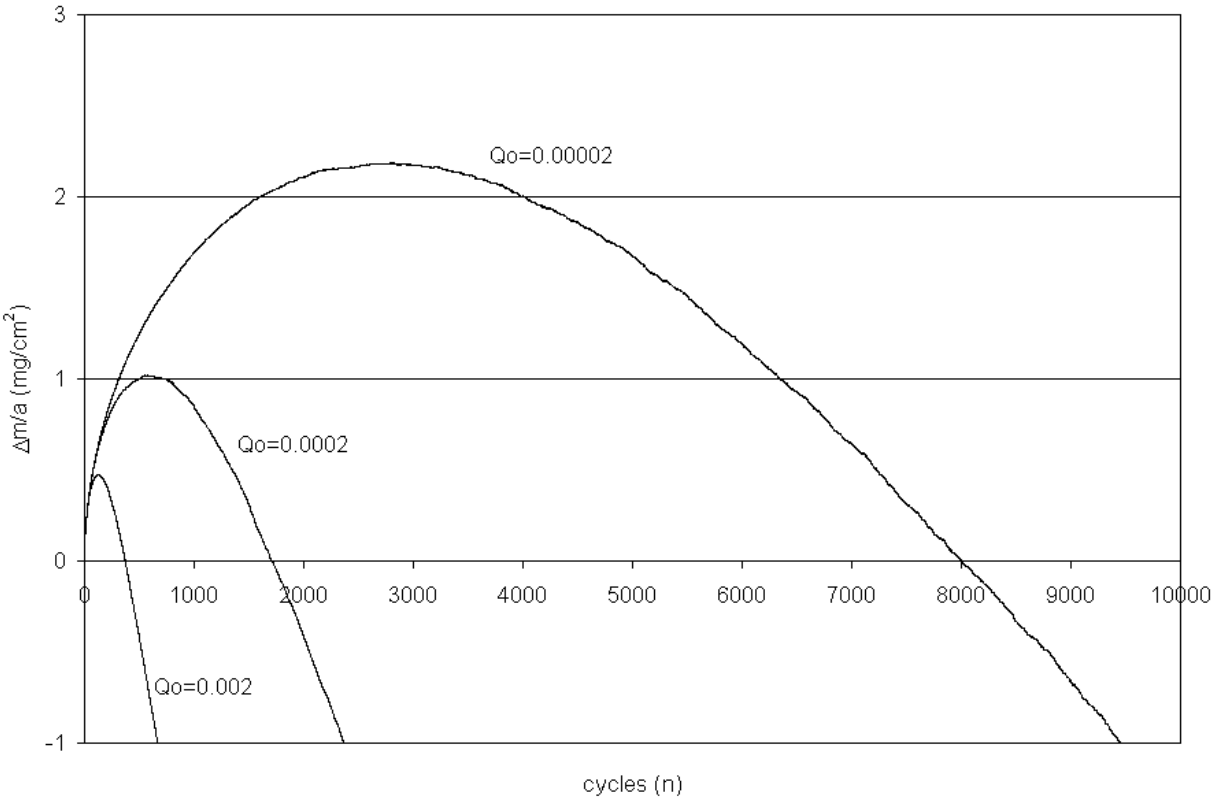

Figure 32. Plot of modeled cyclic oxidation curves for oxides that have kp = 0.066mg^{2}cm^{-4}h^{-1} and 10000 surface segments. The decrease in cycles to negative weight change (cyclic oxidation life) with respect to an increase in Q_o is evident.

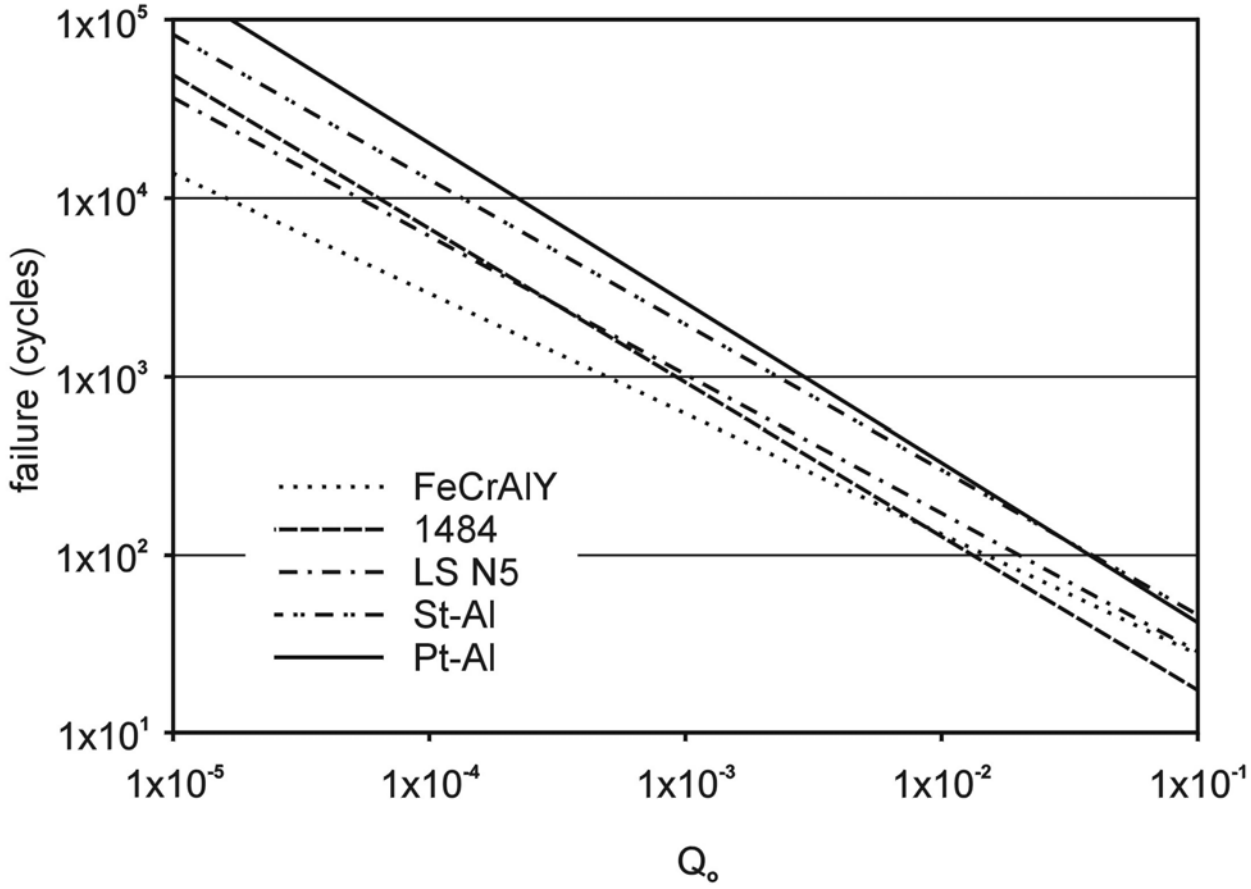

Figure 33. Plot of cycles to failure as a function of Q_o using COSP. Each curve represents the lives of materials and only the isothermal growth kinetics are required for construction.

Quantifying the COSP Q_o is an important problem addressed in this investigation. It is achieved by assigning physical significance to experimental parameters observed from short-term tests. The short-term tests involve monitoring isothermal scale growth by TGA, stresses in the oxide scale and spallation behavior during cooling. A novel AE test had been developed to quantify the amount of oxide that cracks and spalls using the acoustic wave containing information about the acoustic event. Combining equations 27 and 28 as

$$E^{AE} = B \cdot V_{spall} \cdot \Omega_{ox} \tag{46}$$

demonstrates the dependence of the acoustic energy (measured parameter) on the volume of the spall and provides a tool to quantify scale spallation. Next, the definition of the fraction of oxide that spalls, from COSP, can be used as a ratio of volumes in addition to a ratio of weights as

$$F = \frac{W_s}{W_r'} = \frac{V_{spall}}{V_{total}} = Q_o \cdot W_r' \tag{47}$$

Furthermore, a relation of V_{spall} to Q_o is established. With

$$V_{total} = W_r' \cdot A/\rho_{ox} \tag{48}$$

and Equations 46 and 47, the normalized acoustic energy can be related to Q_o as

$$\frac{E^{AE}}{A} = B \cdot Q_o \cdot (W_r')^2 \cdot \Omega_{ox} \cdot \rho_{ox}^{-1} \tag{49}$$

After isolating Q_o as

$$Q_o = \frac{\left(E^{AE}/A\right) \cdot \rho_{ox}}{B \cdot (W_r')^2 \cdot \Omega_{ox}} \tag{50}$$

one can see the dependence Q_o has on the experimentally measurable parameters of acoustic energy, stored elastic strain energy and the isothermal growth kinetics.

5.4 AE EXPERIMENTS

The information obtained form AE experiments is used to quantify the magnitude of the event or for this case, the amount of oxide that spalls by a fracture. In accordance with the COSP, the cracking and spallation events of interest are those during cooling from an oxidation exposure and the measured E^{AE} of these events are used to calculate Q_o with Equation 50.

An optimum exposure of 24 hours at elevated temperature for scale growth has been experimentally determined for AE tests to quantify scale spallation. This exposure time was the compromise between maintaining the short-term capability of the test and an exposure duration long enough for significant scale growth. Exposing the materials for 24 hours generally results in scale growth whereby spallation results in detectable acoustic emission. The driving force for

spallation increases as the scale thickens, from a fracture mechanics approach, and according to COSP, the probability increases with respect to the amount of retained oxide. Caution needs to be taken since a limit of overloading the detection system exists leading to missed or truncated recorded spallation events. On the contrary, if the exposure was too short, the spallation events could conceivably release too little elastic energy where spallation events produce undetectable acoustic events.

Another concern was the cooling rate of the sample. With an event duration limit and event time out built into the electronic hardware it is possible that simultaneous events could be erroneously recorded or completely missed. Rapidly cooling the specimen after the high temperature soak results in a large number of events occurring within a short time. Slow cooling the sample in a controlled method is introduced for better event resolution. Therefore, the typical AE experiment consists of a 24 hour exposure at the temperature of interest followed by a 1°C/min cool to ambient temperature. Material specimens are inserted into the hot zone of a furnace and AEs are continually monitored during high temperature soak and cooling. Since the majority of events occur at or near ambient temperature, all E^{AE} were summed and then normalized with respect to surface area for direct comparison.

Initial AE testing was performed on the 1484 superalloy that was exposed to 1100°C for 24 hours. No acoustic emissions were recorded during the high temperature soak and after 24 hours the specimens were furnace quenched to ambient temperature. The AE results for three specimens are plotted in Figure 34 during cooling. The acoustic emission rate increases as the drop in temperature increases as expected since thermal stresses in the scale increase with

decreasing temperature. This AE rate drops once the specimen reaches room temperature since no additional loading of the scale occurs, therefore areas of no spallation will not spall without a further increase in elastic strain energy. There does exist considerable variability from specimen to specimen in both the AE data and in images of two of these specimens in Figure 35. Different amounts of spallation are apparent in these images where one specimen exhibits 66% scale loss and the other is 97% from image analysis. This spallation variability can account for AE variability. In addition, the furnace quench, where the furnace is turned off and allowed to naturally cool, is faster than the 1°C/min cooling rate resulting in a spallation rate that may be too high for the AE equipment. Rapid cooling could overload the electronic system resulting in truncated recordings and missed events adding to this variability.

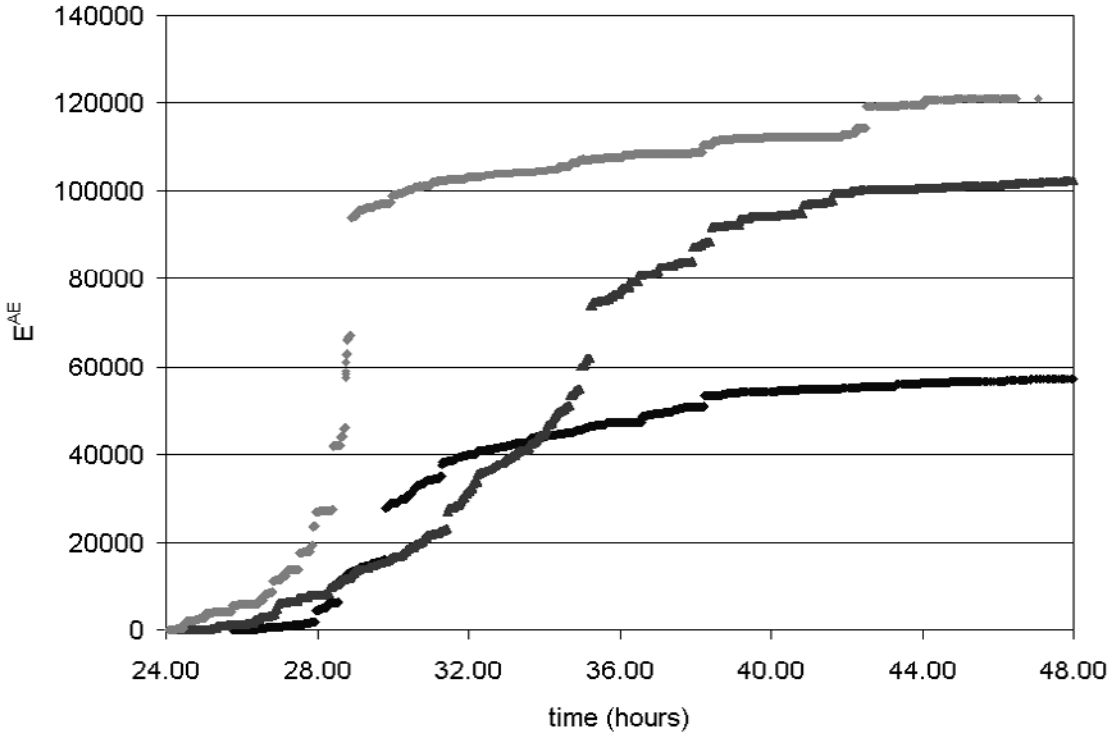

Figure 34. Plot of AE results for 1484 alloy exposed 24 hours at 1100°C and rapidly cooled to ambient temperature by a furnace quench. Variability in total E^{AE} is due to detection problems associated with rapid cooling and variability in specimen performance.

a)

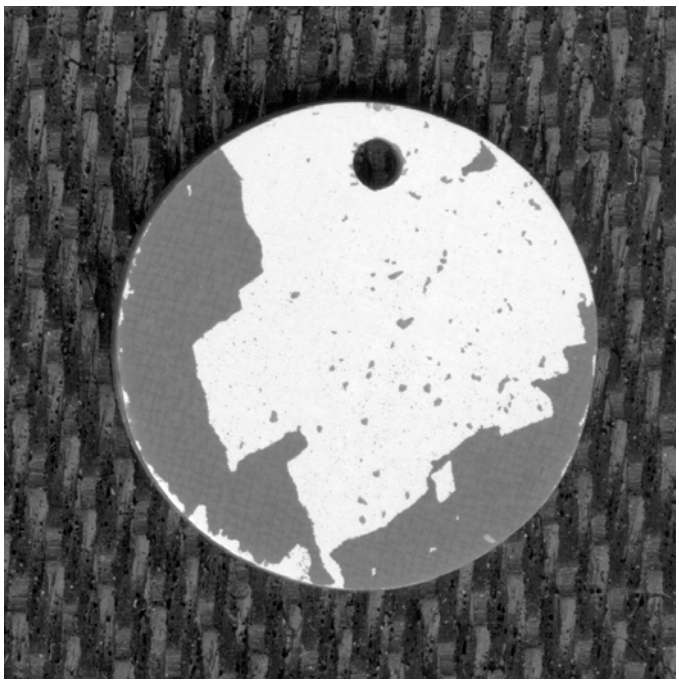

b)

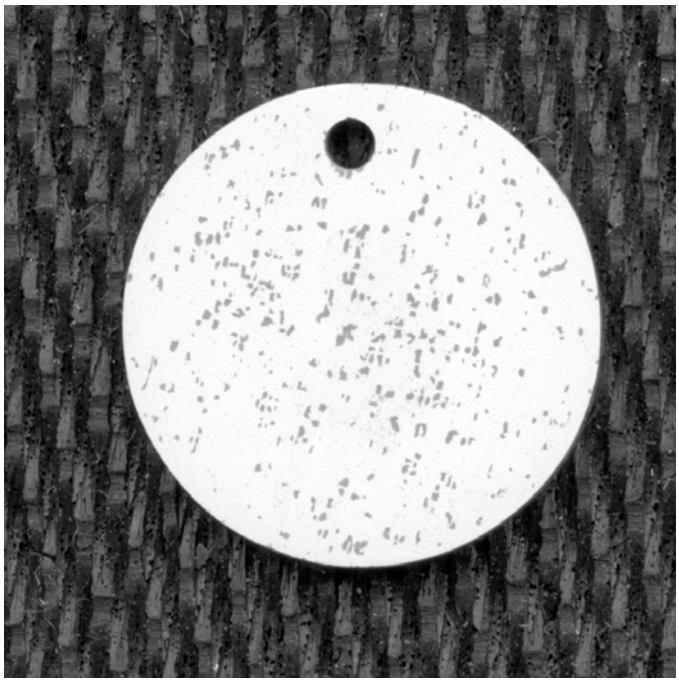

Figure 35. Optical Macrographs of 1484 AE test specimens exposed at 1100°C for 24 hours. Note the difference of amounts of spalled oxide.

For the low S N5 superalloy, cumulative AE energy and temperature of the sample are plotted against time in Figure 36. The slow cooling rate of 1°C/min was used for this and the remaining AE experiments. Like the 1484, no acoustic activity was recorded during the isothermal exposure. This suggests no significant cracking occurred during growth of the scale. The first sign of acoustic activity appeared when the samples began cooling. From the CTE mismatch, the change in temperature begins to load the scale in biaxial compression. As the sample continues to cool, the stress in the oxide scale increases as does the driving force for oxide cracking and spallation. This is apparent in Figure 36 where the AE energy rate increases as the sample temperature decreases until room temperature is approached.

This series of AE tests showed that an increase in temperature did not necessarily increase the acoustic activity or amount of spalled oxide. In Figure 36, the lowest total AE energy was from the sample exposed to 1100°C. Total AE energy values were higher for samples exposed to lower temperatures of 1000°C and 1050°C and to the higher temperature of 1175°C. At the two extreme exposure temperatures for this alloy, mixed oxides are formed on the surfaces of the specimen. Comparison of the surface oxides are presented in macrographs of samples exposed to 1000°C, 1100°C and 1175°C in Figure 37. The 1000°C exposure formed a nickel and aluminum oxide mixture at the edges of the sample and a considerable amount of spallation of the oxide is associated with these regions. In regions further from the edge of the sample, only alumina was found with a dispersion of Ta oxides, Figure 38. This behavior was similar to that of the sample exposed to 1100°C where only alumina was found on the surface with the Ta oxides, Figure 39. The origin of these Ta oxides is from the oxidation of the Ta carbides that are

present in the as-cast structure. It appears that some of the oxide spallation may correlate with the Ta oxides, but the major difference between the 1000°C and 1100°C samples was the contribution to total AE energy from the mixed scale that formed near the edge on the lower temperature exposure. The sample exposed at 1175°C exhibited considerable acoustic activity which resulted from the spallation that is apparent over the entire surface of the scale as shown in Figure 40. This high temperature exposure produced mixed oxides over the entire surface as shown in Figure 37, with the presence of nickel oxide nodules dispersed on the surface. Although oxide spallation was associated with the nickel oxide nodules, the majority of the AE activity can be accounted for by the profuse spallation that is evident over the entire specimen.

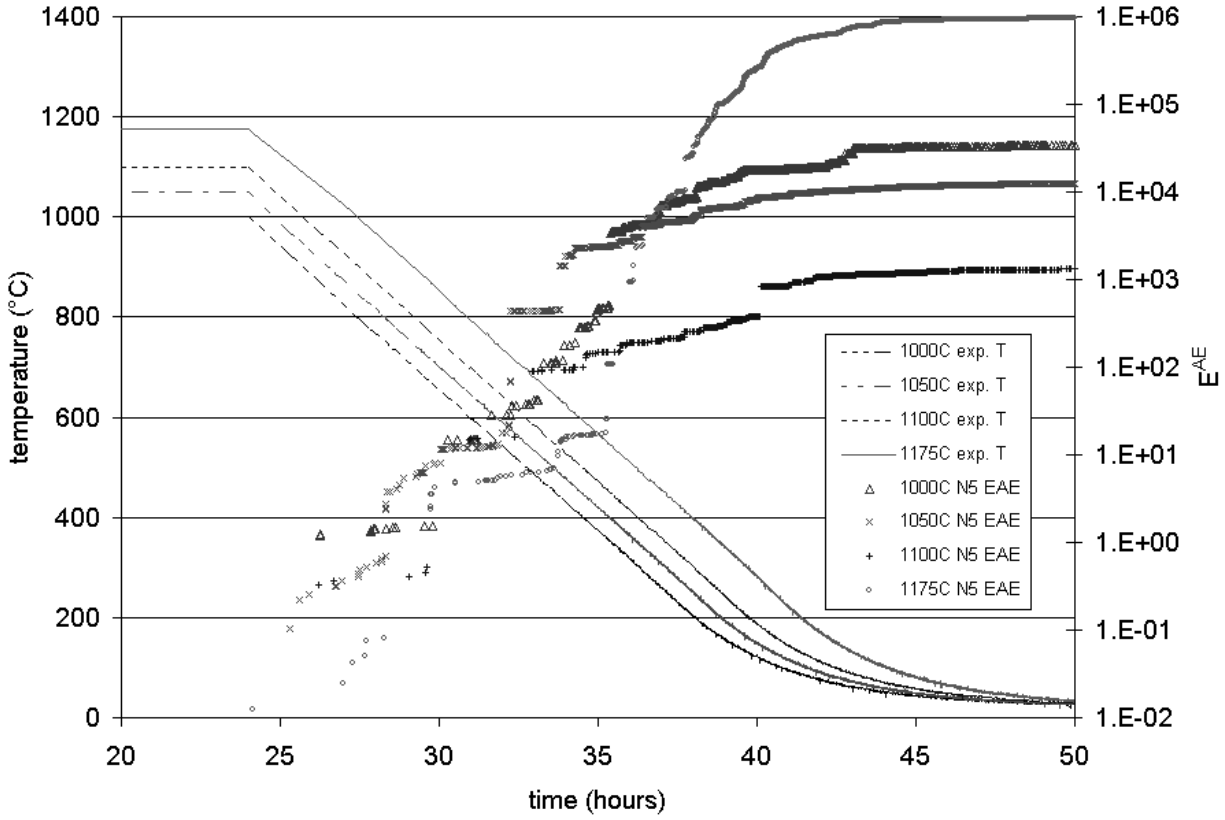

Figure 36. Plot of temperature and cumulative E^{AE} versus time for N5 superalloy exposed for 24 hours to a temperature range from 1000°C to 1175°C followed by a 1°C/min cooling rate.

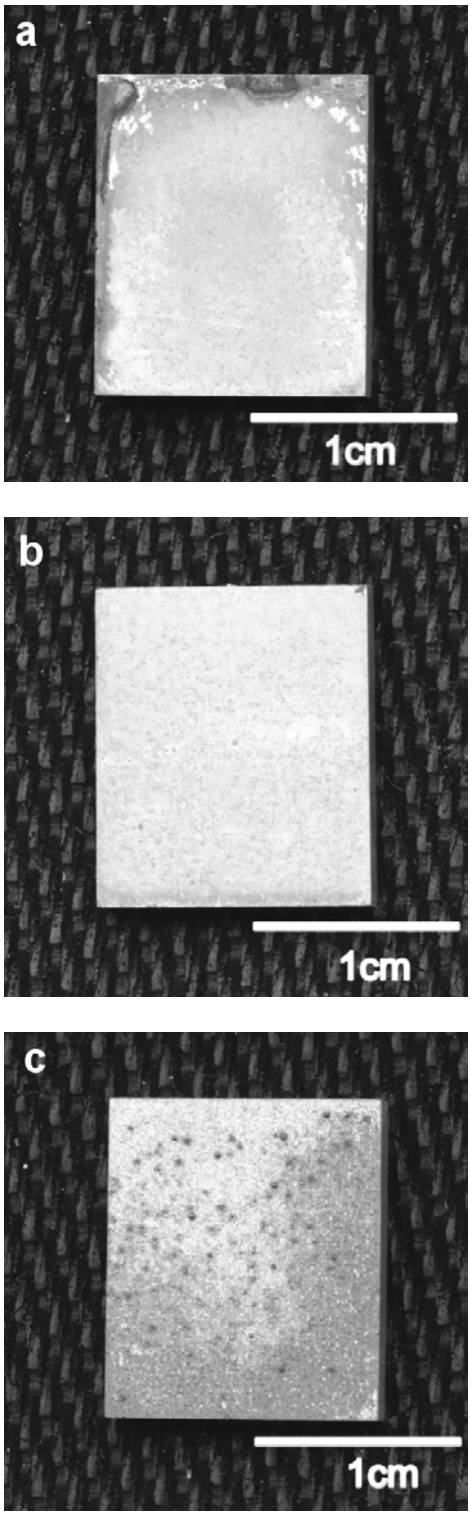

Figure 37. Surface macrographs of N5 samples exposed for 24 hours at a) 1000°C, b) 1100°C and c) 1175°C.

a)

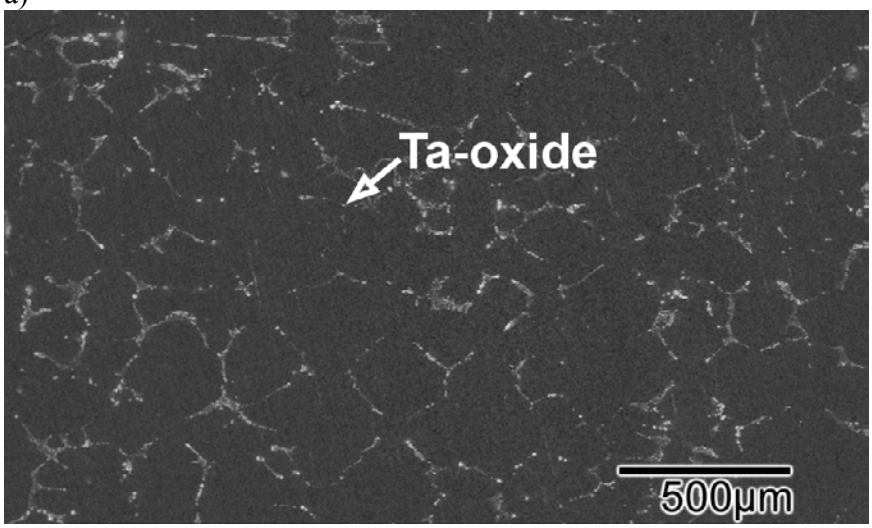

b)

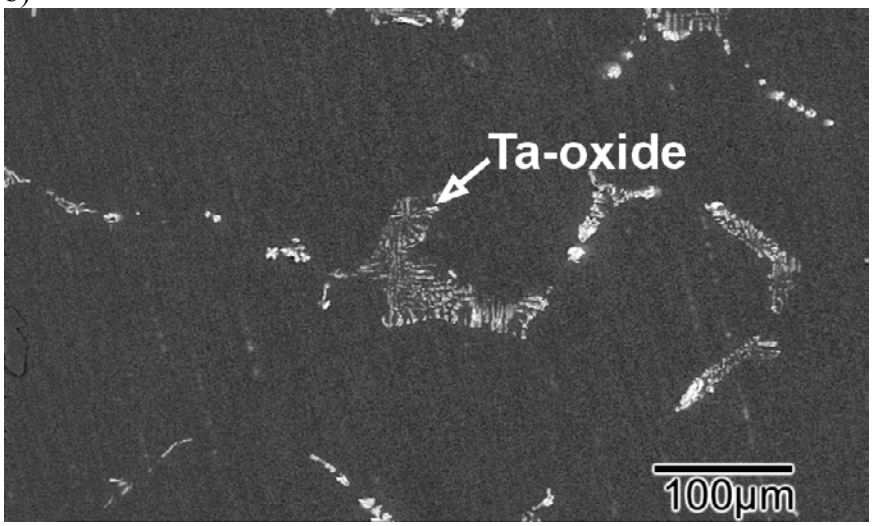

Figure 38. SEM micrograph of the surface from the N5 sample exposed at 1000°C for 24 hours where a) and b) are low and high magnifications respectively.

a)

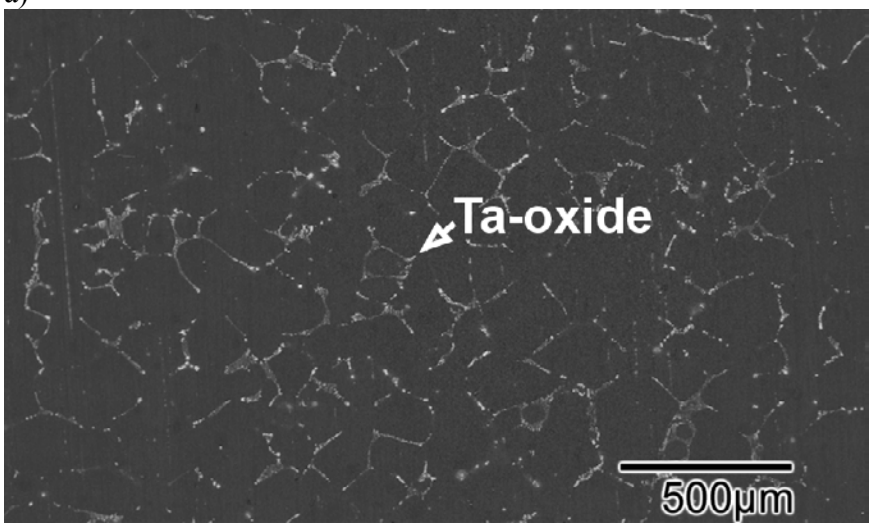

b)

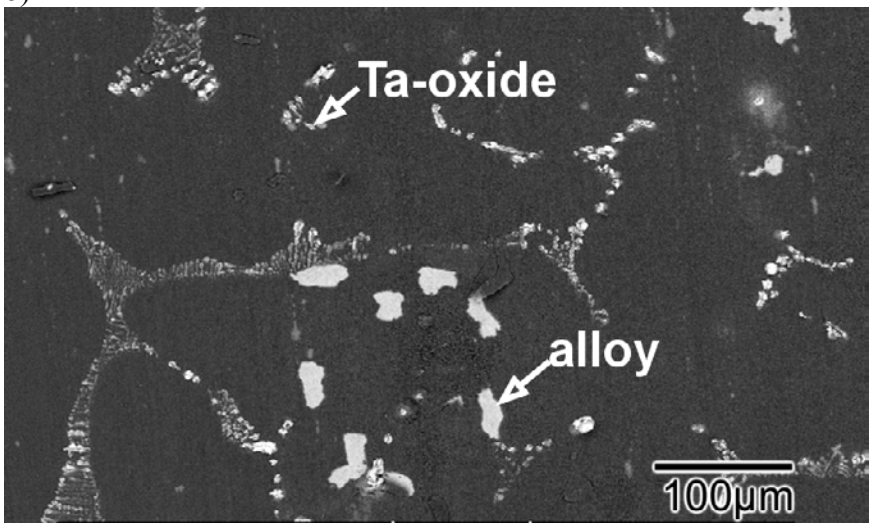

Figure 39. SEM micrograph from the N5 sample exposed at 1100°C for 24 hours where a) and b) are low and high magnifications, respectively.

a)

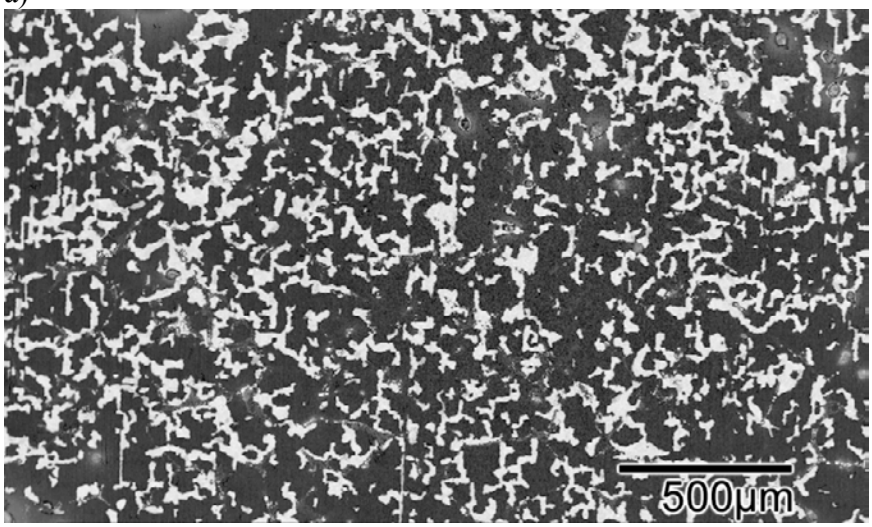

b)

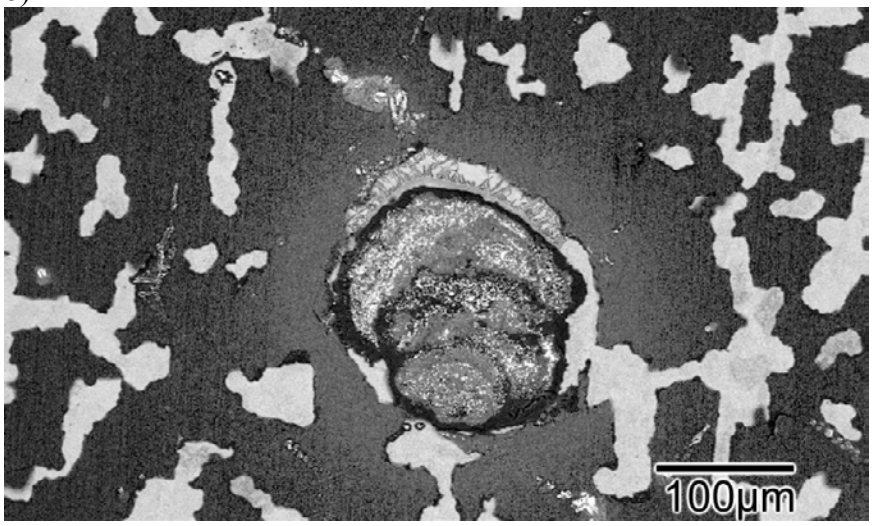

Figure 40. SEM micrograph from the N5 sample exposed at 1175°C for 24 hours where a) and b) are low and high magnifications respectively. The light regions in these micrographs are locations of spalled oxide where the substrate is exposed.

AE tests were also performed on the N5 superalloy coatings with the Pt modified diffusion aluminide coatings (Pt-Al). For these series of experiments, a smaller temperature range from 1050°C to 1150°C was used. Results from these tests are shown in Figure 41 in the same manner as above. Similar to the above specimens, no activity was recorded during the high temperature exposure. AE activity began when the samples were cooled followed by an increase in rate as room temperature was approached. A trend of increasing exposure temperature resulting in increasing the total AE energy was established for this set of experiments. Over this temperature range, the only oxide to form was alumina and no large spallations were evident, Figure 42. SEM investigation reveals wedge cracks are apparent in Figures 43, 44 and 45 for Pt-Al specimens exposed to 1050, 1100 and 1150°C, respectively. The location of these cracks coincides with the grain boundaries of the aluminide coatings. A micrograph of an as-produced aluminide coating is shown in Figure 46 for reference to the aluminide grain boundary network. These SEM micrographs did not reveal any increase in the number, size or distribution of these cracks to account for the increase in total AE energy that was measured. Accounting for the increase in AE energy required the use of polarized light micrographs to reveal the separation of the oxide scale from the underlying metallic substrate. Figure 47 shows the increase in debonded scale with exposure temperature and the debonding appears to coincide with the existing grain boundaries of the Pt-Al coating. This type of buckling results from an interfacial fracture without scale spallation and can contribute to the increase in total AE energy associated with exposures at higher temperatures.

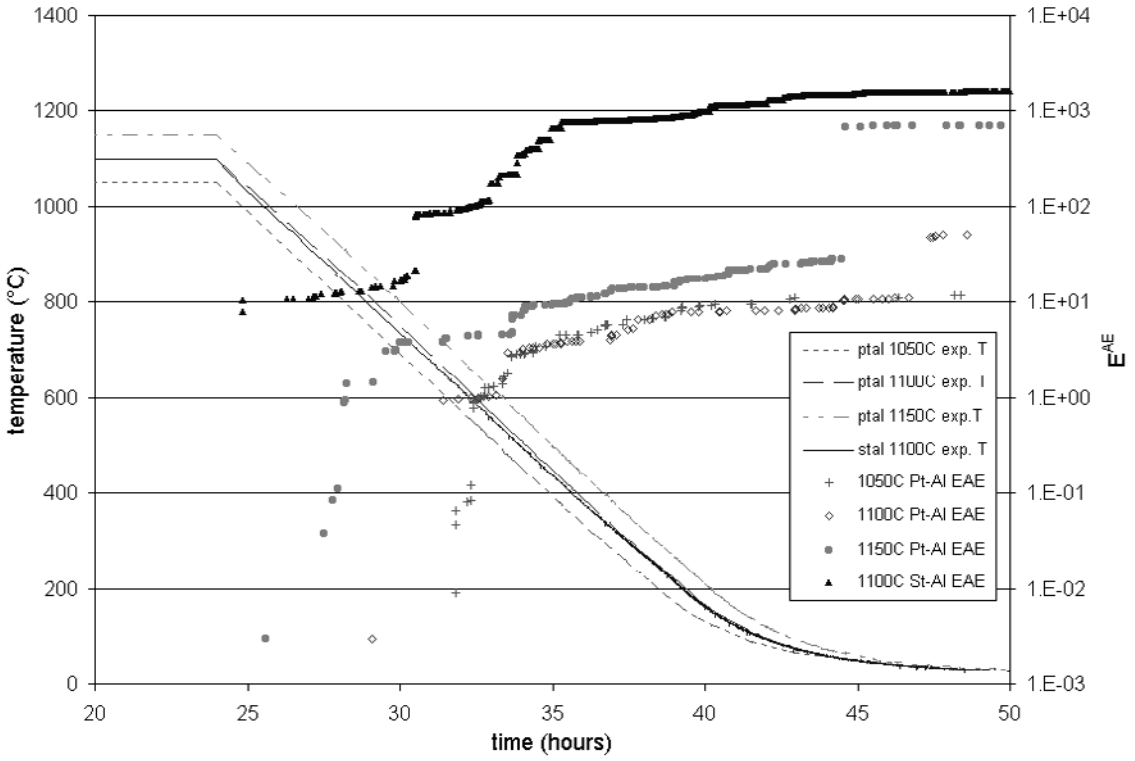

Figure 41. Plot of temperature and cumulative E^{AE} versus time for Pt and straight aluminide coatings on N5 superalloy for 24 hour isothermal exposures followed by a 1°C/min cooling rate. Pt-Al specimens were exposed to a temperature range of 1050°C to 1150°C.

a)

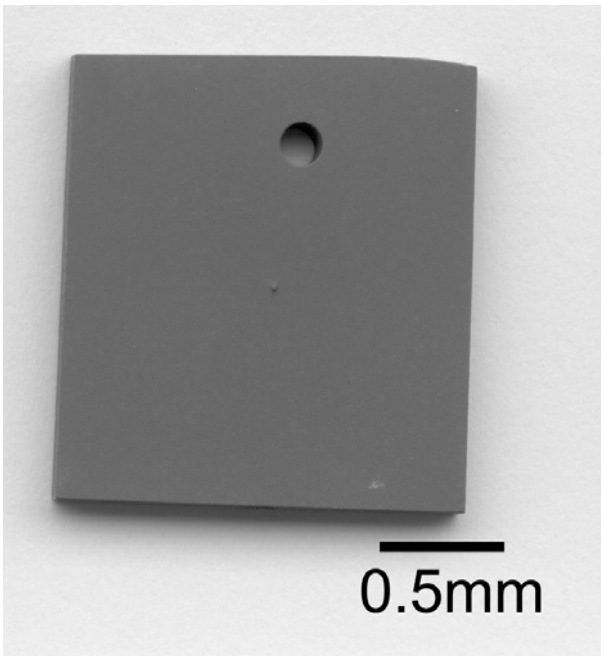

b)

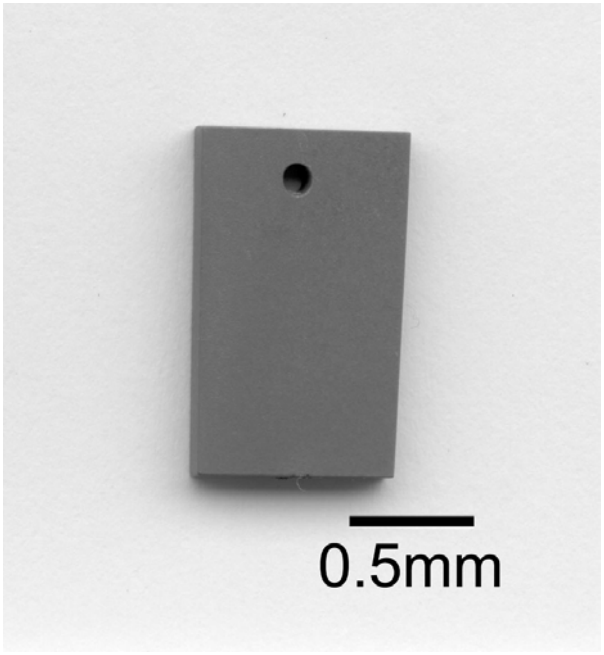

Figure 42. Optical macrograph of a) Pt-Al and b) St-Al coatings used in AE experiments. These coatings were exposed at 1100°C for 24 hours.

a)

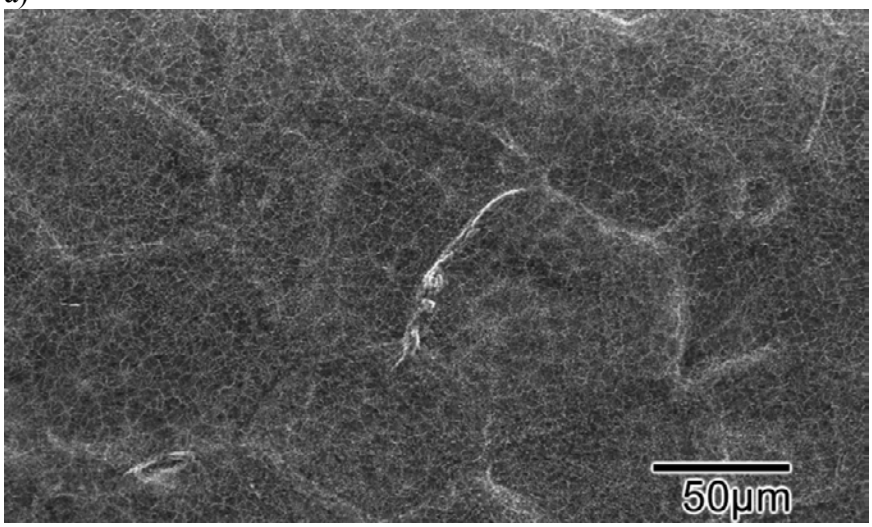

b)

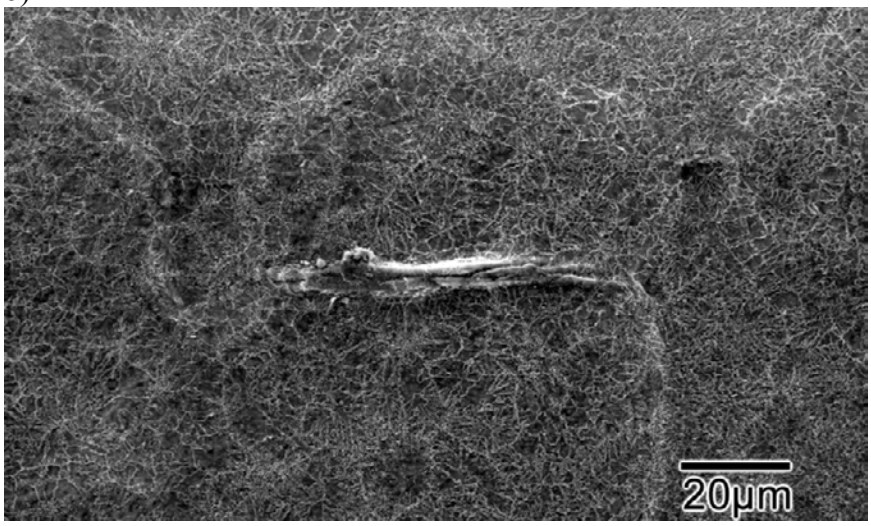

Figure 43. SEM micrographs of the surface of the sample exposed at 1050°C for 24 hours where a) and b) are low and high magnification respectively. Wedge cracking is associated with the underlying aluminide grain boundaries.

a)

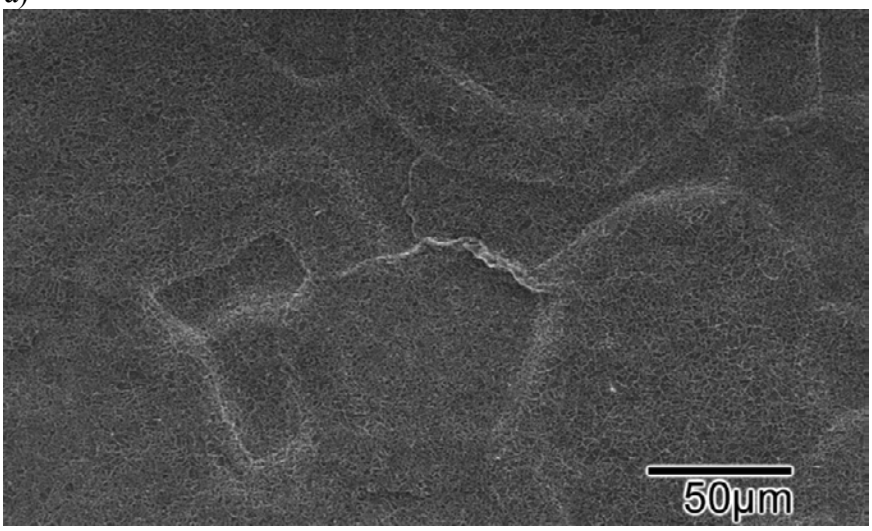

b)

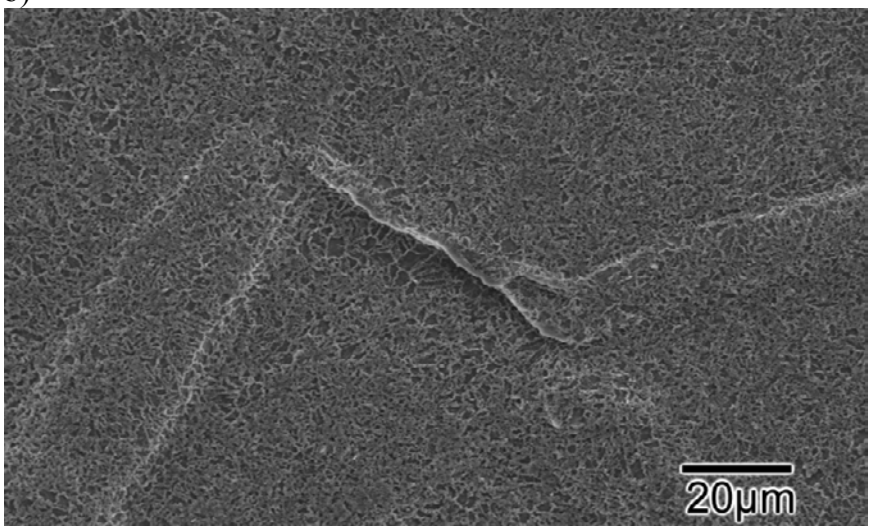

Figure 44. SEM micrographs of the surface of the sample exposed at 1100°C for 24 hours where a) and b) are low and high magnification respectively. Wedge cracking is associated with the underlying aluminide grain boundaries.

a)

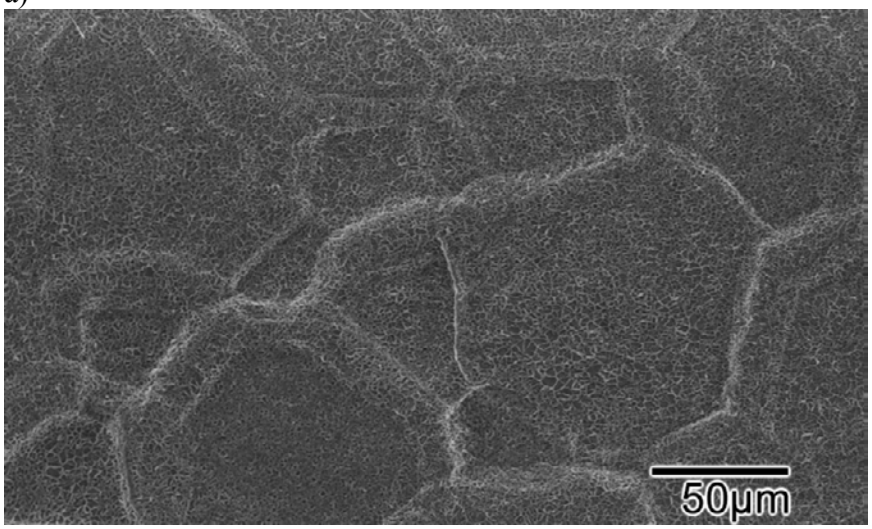

b)

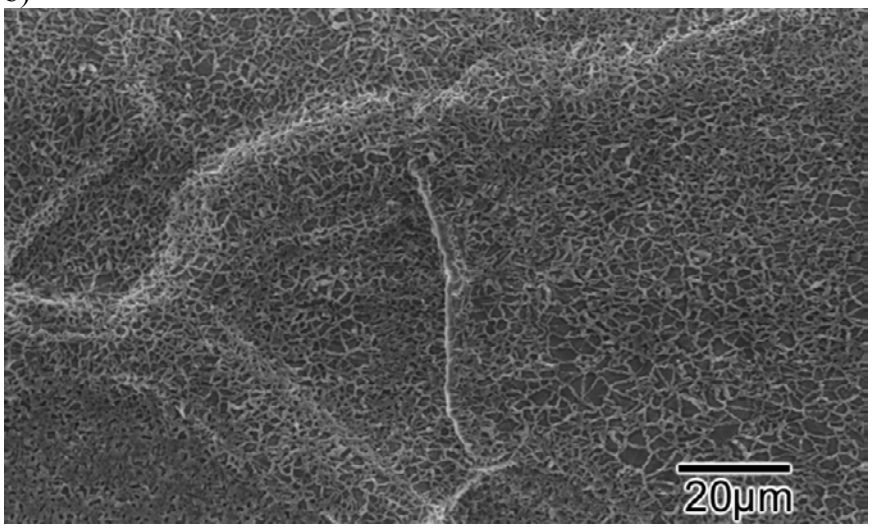

Figure 45. SEM micrographs of the surface of the sample exposed at 1150°C for 24 hours where a) and b) are low and high magnification respectively. Wedge cracking is associated with the underlying aluminide grain boundaries.

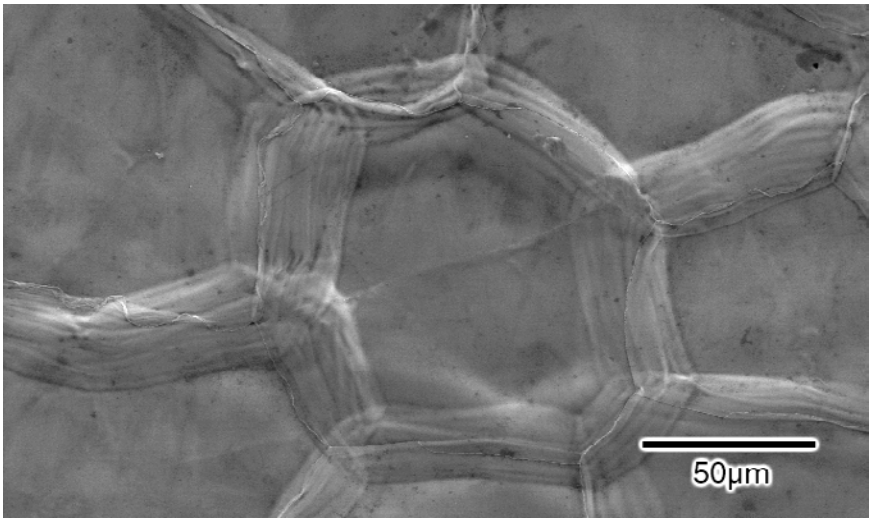

Figure 46. SEM micrograph of the surface of an as-coated Pt-Al coating. Note the grain boundary network and the ridges associated with it.

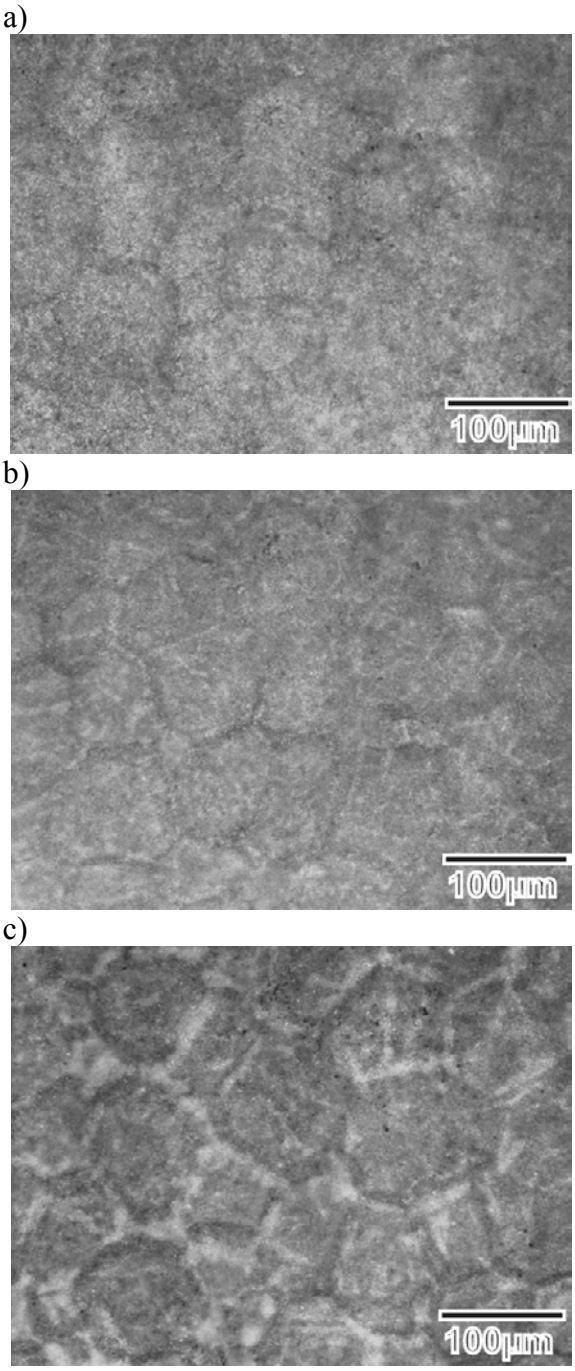

Figure 47. Polarized light micrographs of the surface of the Pt-aluminides exposed at a) 1050°C, b) 1100°C and c) 1150°C. Lighter regions are areas where the oxide scale has separated from the aluminide coating.

Only 1100°C was used for AE testing of the Ni aluminide (St-Al) coating on N5 superalloy. This temperature was used to compare with the 1100°C Pt-Al coating and results of these AE tests are shown in Figure 41. The St-Al exhibited an order of magnitude more total AE energy than exhibited by the Pt-Al coating during the 1100°C experiment. In agreement with this result, SEM analysis shows considerable spallation of the oxide scale in Figure 48a and polarized light microscopy reveals a considerable amount of buckling in the regions where the scale did not spall, Figure 48b. Spallation and buckling of the scale correlate with the ridges at the grain boundaries of the aluminide coating.

a)

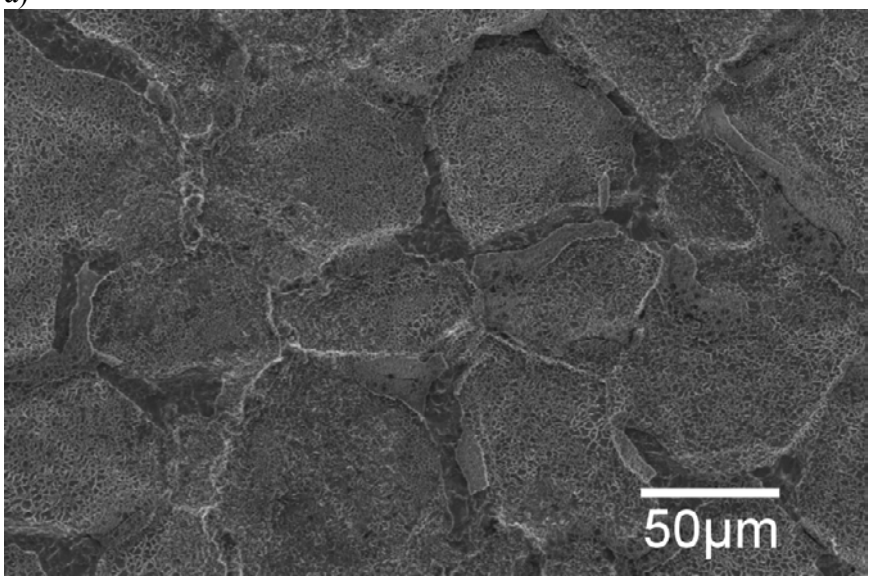

b)

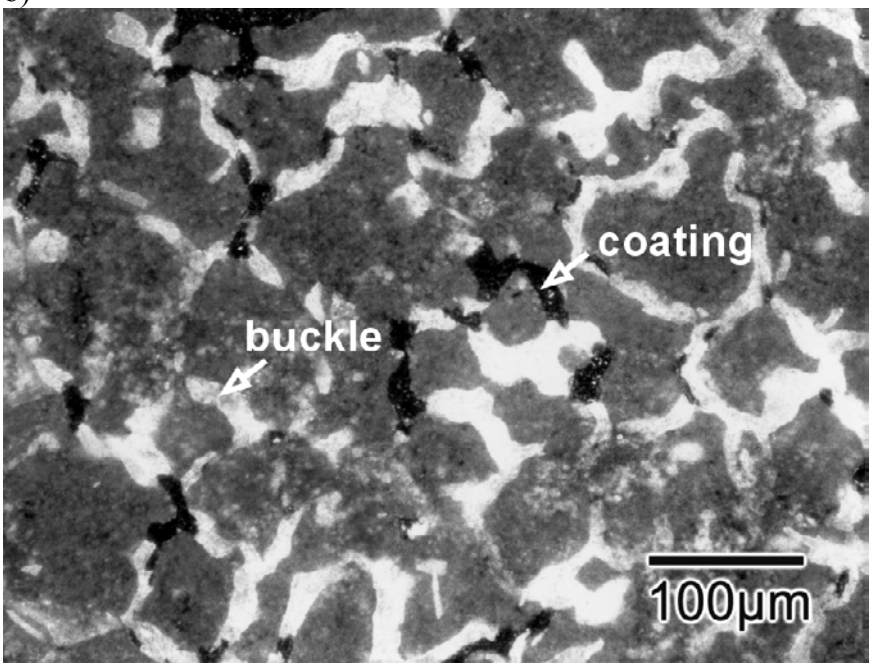

Figure 48. Micrographs of the straight-aluminide exposed at 1100°C for 24 hours where a) is the SEM image and b) is the polarized light image. For the polarized light micrograph, the light areas are separated oxide, darker areas are exposed coating.

A number of FeCrAlY Specimens were exposed to 1100°C with a slow cool of 1C/min to ambient laboratory temperature and acoustic energy results are plotted in Figure 49. No transient mixed oxides were present on the surface, as expected from isothermal TGA experiments and cross section micrographs, and no large spalls of oxide are present in the specimen macrograph in Figure 50. Furthermore, SEM analysis revealed only small isolated mixed oxides on the surface of the oxidized specimen. These oxides were determined by EDS to be either yttrium or nickel oxides and Figure 51 shows the particle distribution. Yttria particles dispersed in the alumina scale are accounted for since the alloy contains yttrium. Since FeCrAlY has no designated nickel content, any nickel in the alloy or on the surface is considered an impurity. It is the nickel particles that are associated with wedge cracks found in the alumina as shown in Figure 51b. This extrinsic failure mode by Ni contamination as NiO in the alumina scale contributes to a variation in the AE data.

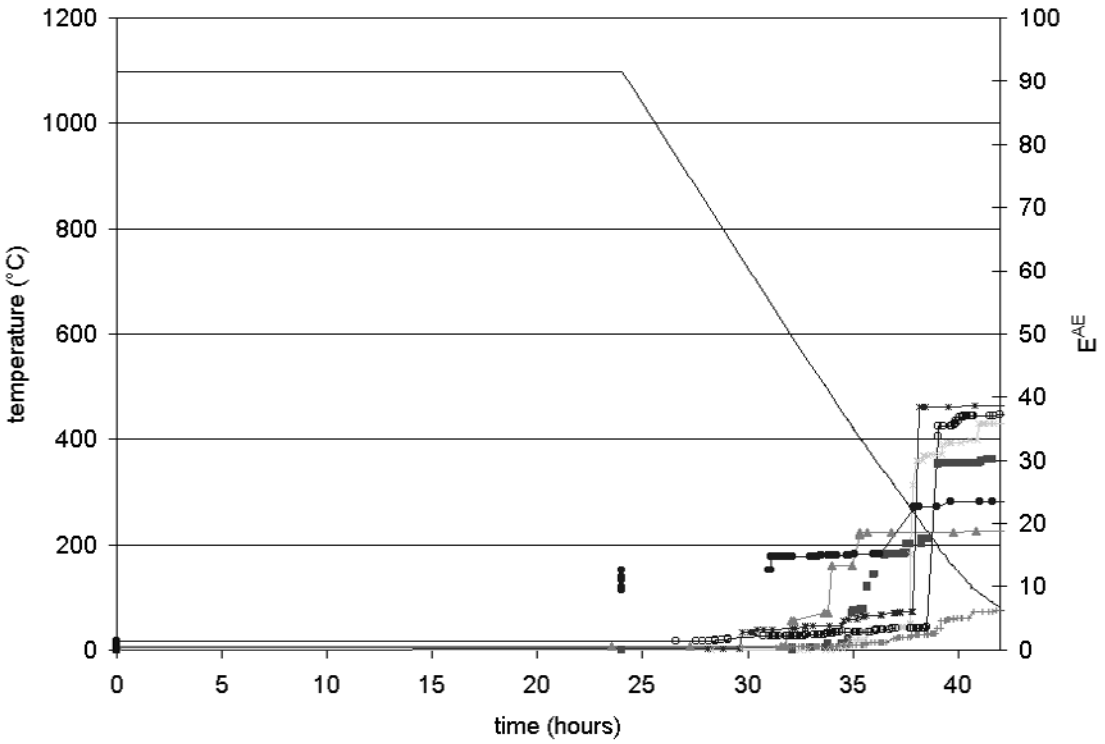

Figure 49. Plot of temperature and cumulative AE-energy versus time for FeCrAlY for 24 hour isothermal exposures at 1100°C followed by a 1°C/min cooling rate. Seven FeCrAlY specimens were exposed to gain insight in AE test reproducibility.

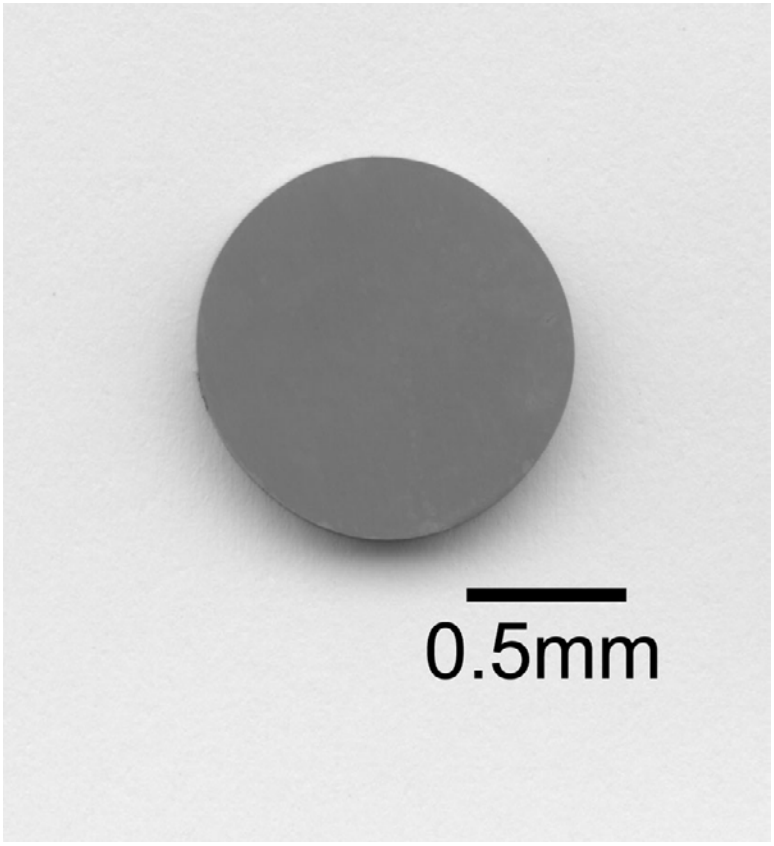

Figure 50. Optical macrograph of FeCrAlY specimen exposed at 1100°C for 24 hours.

a)

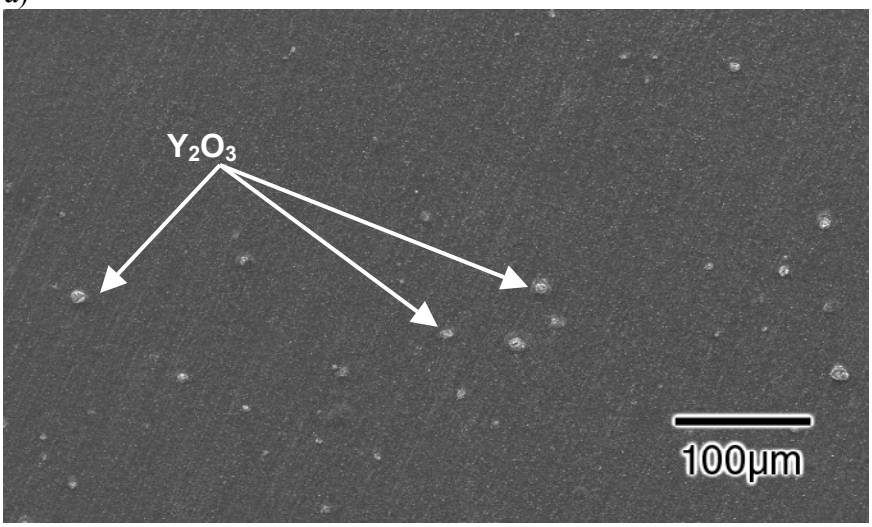

b)

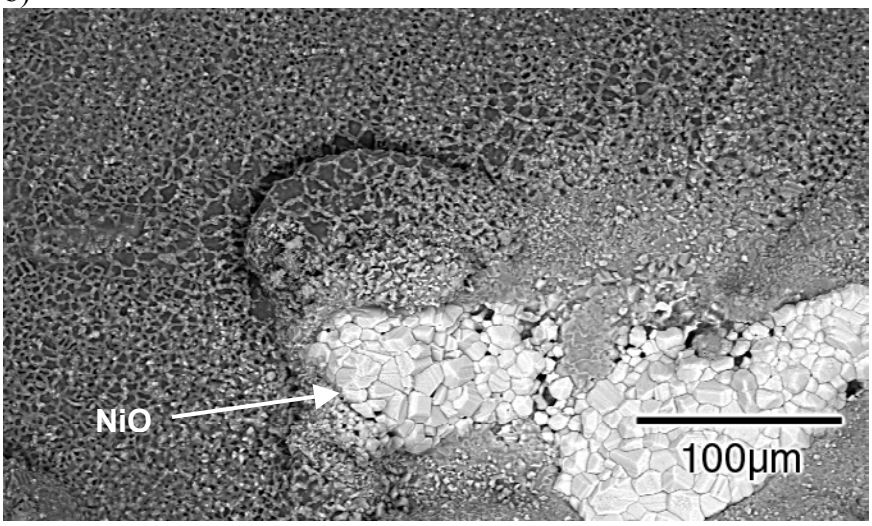

Figure 51. SEM micrographs of the surface of FeCrAlY exposed at 1100°C for 24 hours. Low magnification image a) shows yttria particles on the surface and high magnification image b) shows NiO and associated wedge cracks.

Ni specimens were also monitored by AE and results for a 24 hour exposure at 1100°C and this data is presented in Figure 52. The Ni specimens with the thickest scale are one of the more acoustically active systems tested during cooling and the only system to emit any activity during scale growth during the isothermal high temperature soak. A macrograph of the specimen in Figure 53 shows that no spallation has occurred and a uniform adherent NiO scale is present. Furthermore, SEM analysis in Figure 54 shows the only apparent damage to the NiO scale are transgranular cracks. The low magnification SEM backscatter electron image in Figure 54a exhibits channeling contrast. Channeling contrast is an electron diffraction imaging technique and the contrast is a function of crystal orientation. If the crystal or grain is oriented to create the Bragg angle with respect to the electron beam source and detector, the detected signal will results in a higher intensity than that for a grain orientation not satisfying the Bragg condition. Therefore, the contrast is a result of crystal orientation and each grain of the NiO scale is readily imaged. Another feature in these images to delineate each grain is the grooving of grain boundaries that are apparent in Figure 54b. A few grains in this micrograph contain the transgranular cracks. It is unlikely that one crack could release enough elastic energy to create a detectable acoustic event, but it is conceivable that a number of simultaneous cracks could be detected. This is especially possible with the significant fraction of grains exhibiting these transgranular cracks.

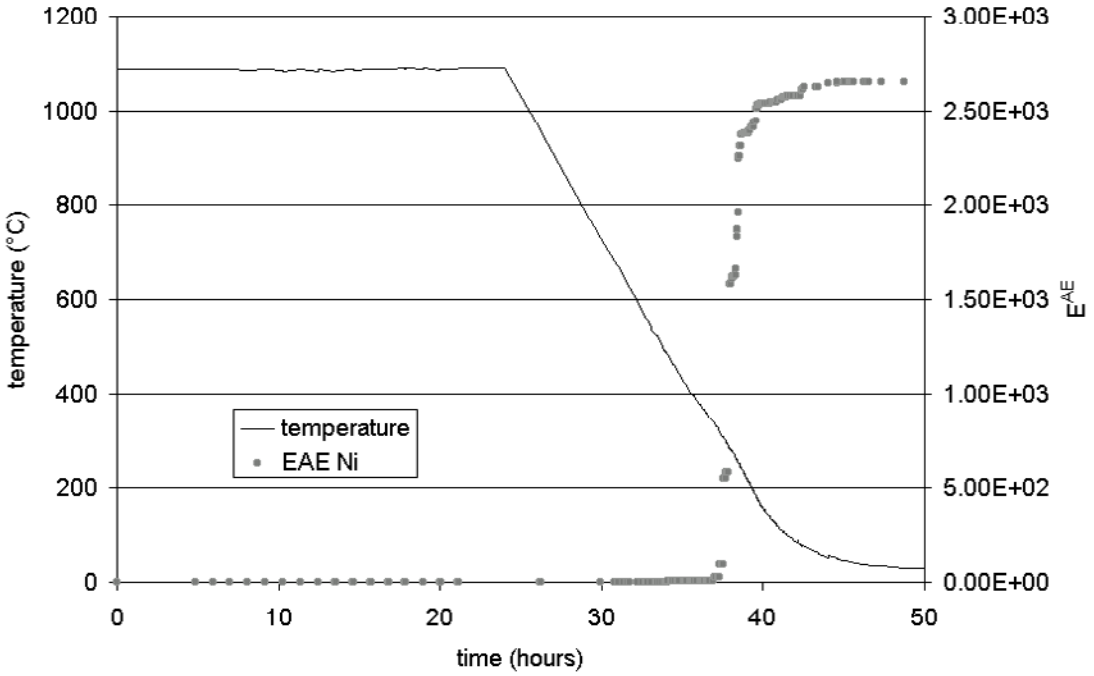

Figure 52. Plot of temperature and cumulative AE-energy versus time for nickel for 24 hour isothermal exposures at 1100°C followed by a 1°C/min cooling rate.

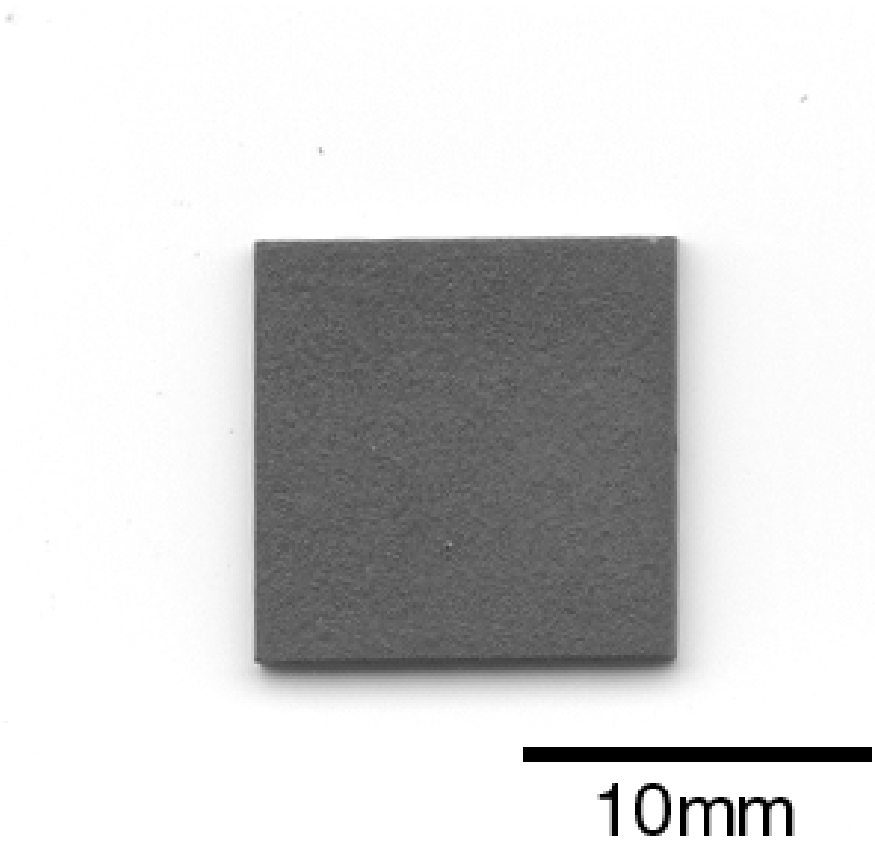

Figure 53. Optical macrograph of Ni after exposure at 1100°C for 24 hours.

a)

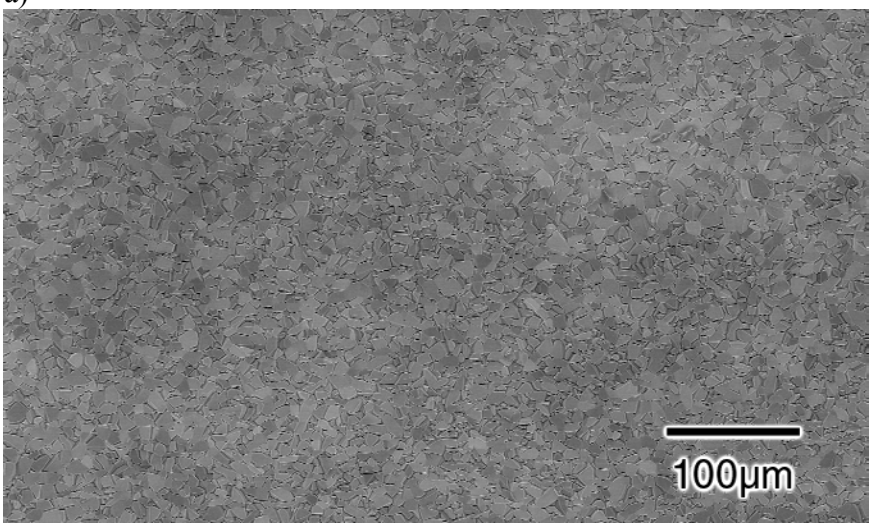

b)

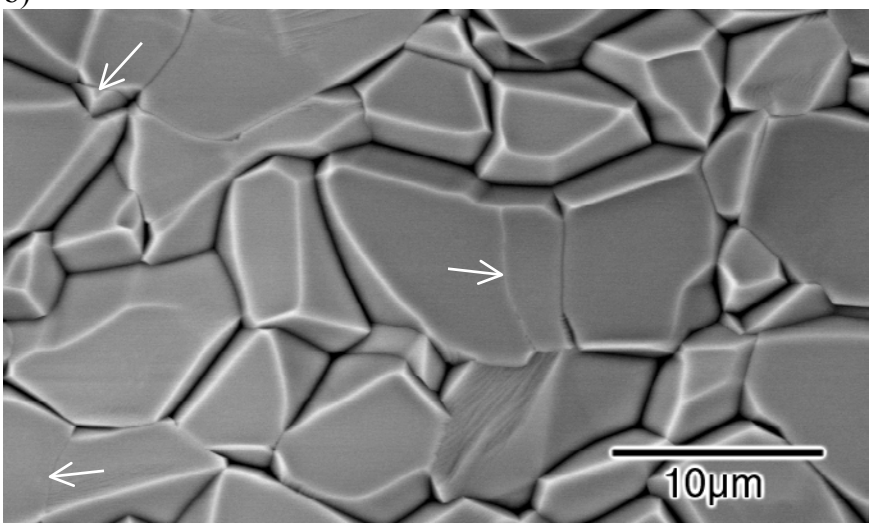

Figure 54. SEM surface micrograph of Ni exposed at 1100°C for 24 hour where in a) NiO grains are imaged by channeling contrast and b) transgranular cracks are evident. The oxide scale exhibits grooves at the grain boundaries, but the arrows in b) indicate cracks.

The compilation of AE data versus time is shown in Figure 55 for all alloys and coatings exposed to 1100°C except for 1484. 1484 was the most acoustically active material at 1100°C with an E^{AE}/mm^2 of 87000 which is almost two orders of magnitude higher than the other alloys and coatings. All data is normalized with respect to surface area for a direct comparison. A generalization about the performance of these materials can be drawn from this data and long-term cyclic oxidation results. The low acoustically active materials, Pt-Al and FeCrAlY, exhibit the longest cyclic oxidation behavior and the highly active 1484 has the shortest cyclic oxidation life of 24 cycles. Intermediate cyclic oxidation behavior materials like St-Al and LS N5 produce intermediate acoustic activity. This trend of increased acoustic activity is important, but if total E^{AE} is to determine the volume of the spalled oxide, the stored elastic strain energy must be known.

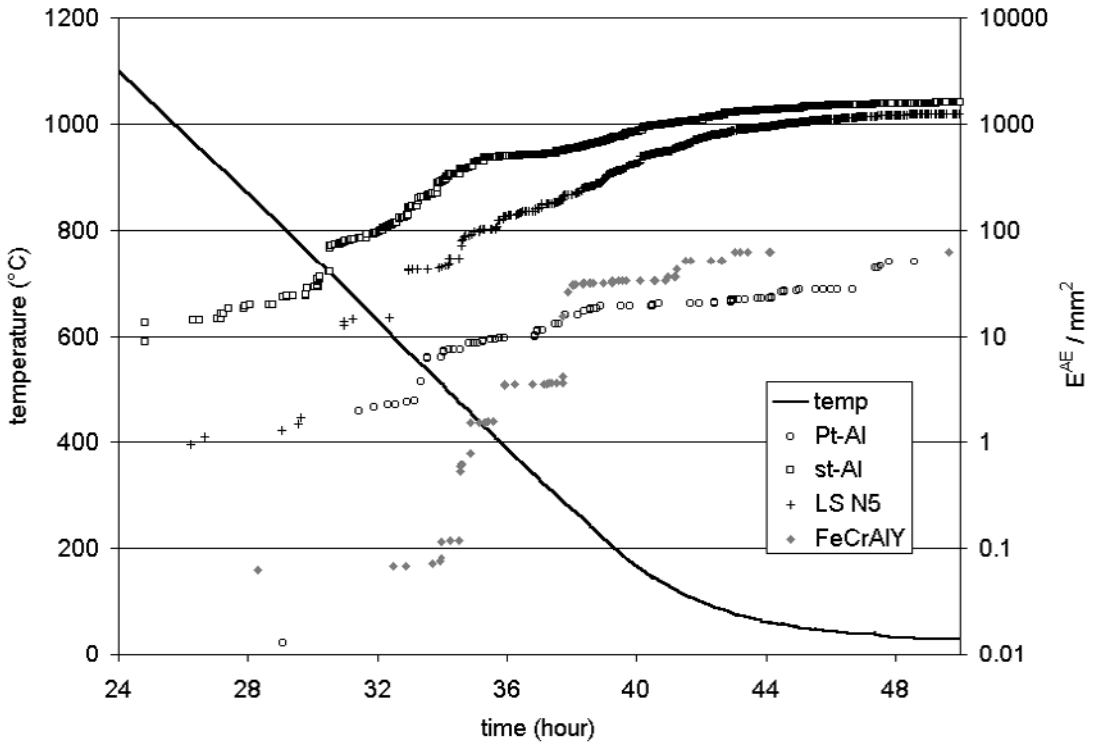

Figure 55. Plot of the compilation of AE data during cooling to ambient temperature. All materials were exposed at 1100°C and EAE was normalized to surface area for direct comparison.

The major concern with the acoustic emission tests is the reproducibility of measurements. Several specimens of each alloy were exposed to identical conditions to obtain a range of data expected from this type of test. Only the alloys 1484, LS N5 and FeCrAlY were involved with the multiple exposures due to specimen availability. This group of alloys also provided a range of acoustically active materials (low, medium, and high) to determine a relation of AE reproducibility on acoustic activity. A plot of error for an 80% confidence level is displayed in Figure 56 for each alloy where average values of E^{AE}/mm^2 are shown in parenthesis. The high and low acoustically active systems produce the largest error in the measurement. A significant contribution to the range of results found with 1484 was from variation in sample performance as discussed above, but some error could result from data recording limits with this much activity. Spallation variation was evident from the NiO contamination in the FeCrAlY (low acoustic activity), but some spallation events might not be large enough for detection resulting in erroneously low E^{AE}. Fortunately, the best performance came from the LS N5 producing the intermediate level of AEs with a relative error of 18%. Enough spallation occurred in this system that any variation from contamination was minor and equipment detection limits were not approached. Furthermore, the LS N5 samples used in the reproducibility test had a range of specimen thickness from 1 to 4mm demonstrating that small variations in coupon size are not an issue.

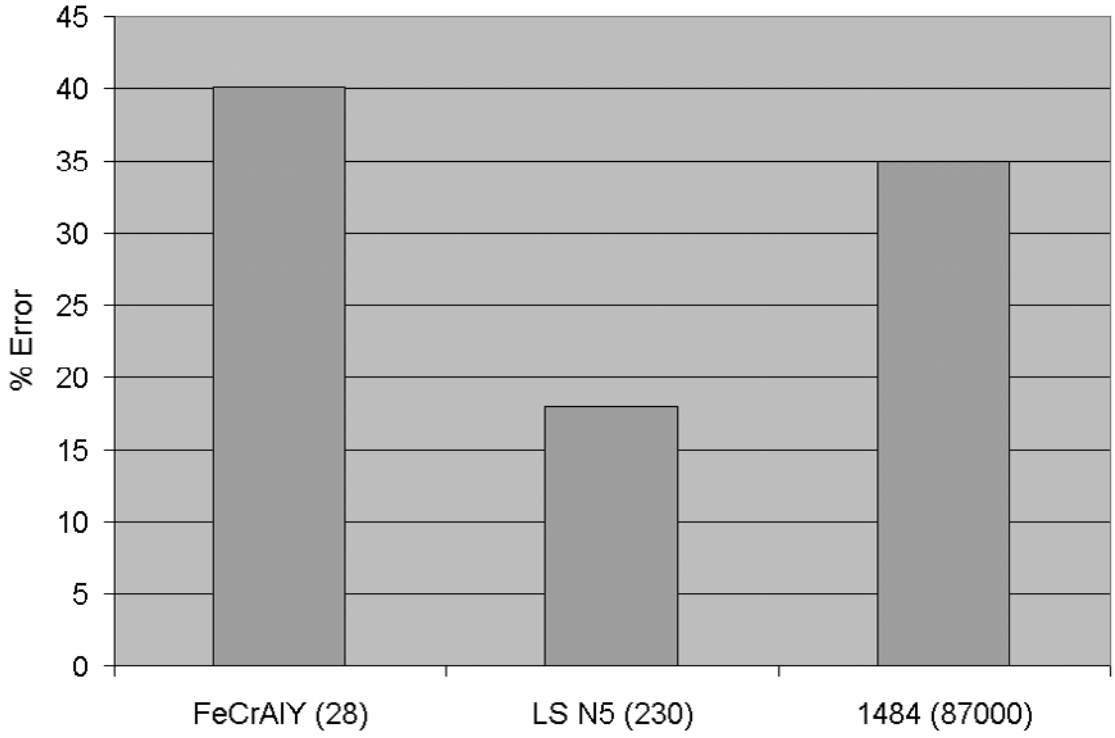

Figure 56. Plot of relative error in measured E^{AE} for alloys in the reproducibility study. Numbers in parenthesis are the average E^{AE} (mV^2s/mm^2)for that material.

5.5 STRESS MEASUREMENTS

The known stress state of the oxide is critical to determine Q_o in Equation 50 for cyclic oxidation life-time prediction. The biaxial stress state is necessary for calculating the stored elastic strain energy in the oxide scale. Thermal stress in the oxide scale can be readily calculated form CTE data of both the oxide scale and the substrate, but this calculated approach does not consider contributions to the residual stress state from oxide growth stresses or any relaxation. The directly measured residual stress state of the oxide scale will include these effects to provide an accurate stress value ultimately used for strain energy density calculations and the results are summarized in the following. The techniques used were the symmetrical tilting and FIT (fixed incident tilting) for room temperature residual stress measurements and the rocking technique for high temperature growth stress measurements.

XRD stress measurements were made on the alumina scale formed on FeCrAlY after 24 hours at 1100°C. The cooling rate after this exposure was the same as that of an AE experiment of 1°C/min. FeCrAlY exhibits one of the largest mass gains after 24 hours when compared to other alumina forming alloys and coatings and the lack of any mixed transient oxide forming on top of the alumina scale facilitated the use of the symmetrical tilting technique. Experimental 2θ plot of a θ-2θ scan are displayed in Figure 57 for the (146) peak where the diffraction peaks shift to higher 2θ with an increase in tilt angle resulting from a compressive stress. There is a uniform increase in peak intensity as the specimen is tilted as a result of defocusing the x-ray beam over the specimen increasing the diffracting volume of the thin oxide layer and a lack of texture of the

alumina grains[72]. These scans were performed at a 10° intervals from $\psi = 10°$ to $\psi = 90°$. A d-spacing versus $\sin^2\psi$ plot is presented in Figure 58 for the (146) with good linear relationship suggesting a biaxial stress state with no stress gradients. The additional (226) and (1.0.10) were utilized to further elucidate the stress state model which this alumina follows in the measurement since each plane has a unique x-ray elastic constant according to the Reuss model. Since the macroscopic stress measured by XRD should be the same for any crystallographic plane, agreement of stress values from using the (146), (226) and (1.0.10) can only satisfy one of the elastic models. Results for the three planes are listed in Table 5 for the Reuss and Voigt models. It is apparent that this scale exhibits the Voigt behavior with a residual biaxial stress and error of –3.33GPa +/- 90MPa, respectively.

Table 5. Residual stress measurement results for alumina scale on FeCrAlY exposed to 1100°C for 24 hours

	Stress (GPa)	
Peak	Voigt	Reuss
146	-3.28 ± 0.07	-3.20 ± 0.08
226	-3.41 ± 0.08	-2.92 ± 0.07
1.0.10	-3.31 ± 0.09	-3.60 ± 0.09

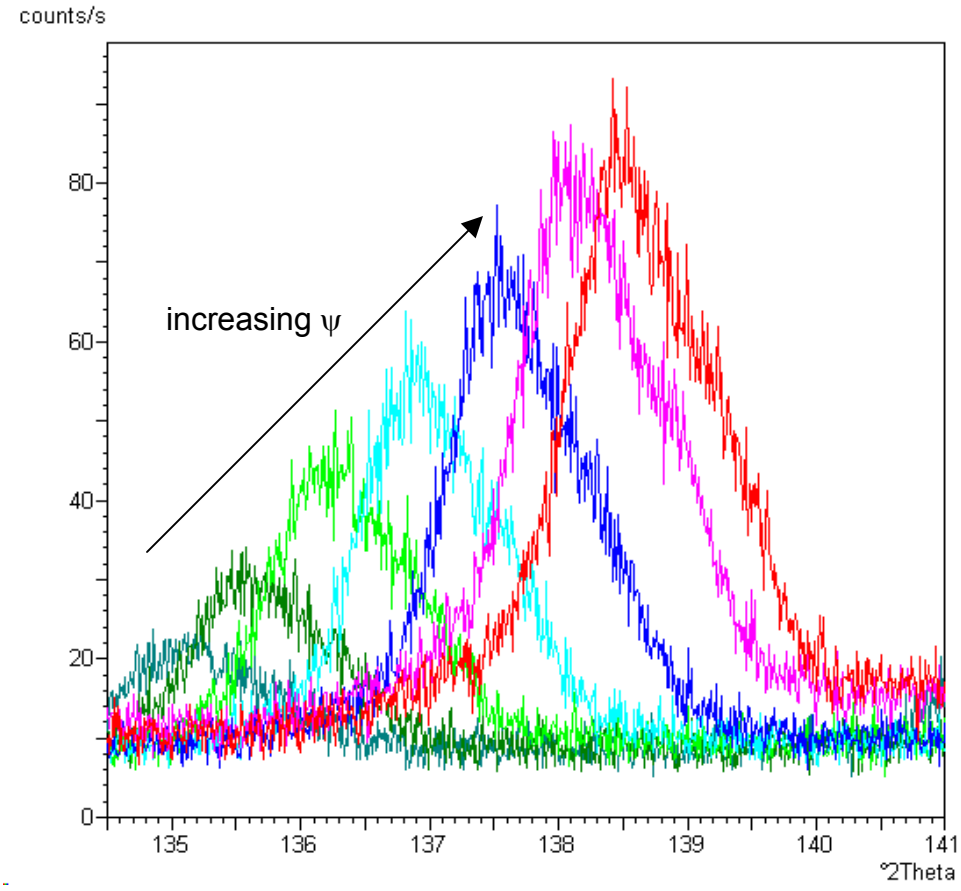

Figure 57. Plot of stress measurement 2θ scans (by tilting) using the (146) peak of α-alumina formed on FeCrAlY. The specimen was exposed at 1100° for 24 hours followed by a 1°C/min cool to ambient temperature.

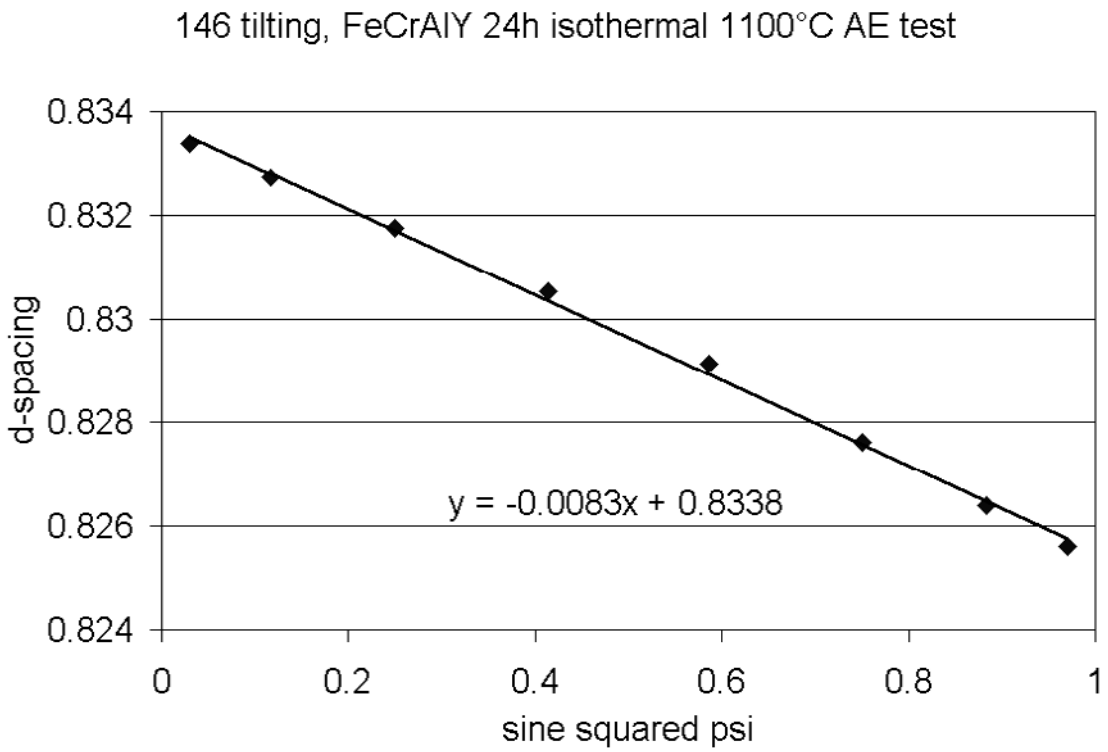

Figure 58. Plot of d-spacing versus $\sin^2\psi$ for the (146) obtained by symmetrical tilting method. The slope of this line is used for stress calculation. The linear equation shown in the plot was fitted to the data and the slope is used for stress calculations.

The calculated thermal biaxial stress state of alumina formed on FeCrAlY is –3.5GPa with the elastic properties of alumina as E_{ox} = 400GPa[73] and ν_{ox} = 0.24[74], and CTEs of $8.8x10^{-6}K^{-1}$ and $15x10^{-6}K^{-1}$ for α-alumina[75] and FeCrAlY[76,77] respectively. Although this calculated thermal stress agrees well with the measured residual stress, previous high temperature experiments at 1100°C on this material have produced a measured –1.3GPa growth stress[78]. This measurement was performed using the same equipment as this investigation, but utilized the fixed incident multiplane (FIM) technique. Although the large measured growth stress introduces a discrepancy with the results from this investigation, the cooling rate needs to be considered and any stress relaxation may explain the difference. This effect of cooling rate is apparent when the measured residual stress values between the investigations are compared. Sarioglu et. al. measured a –4.4Gpa[42] stress in the alumina scale on a specimen that was air quenched form 1100°C. As a result of the rapid cooling, most of the growth and thermal strains were retained, but when the specimen is cooled 1°C /min a significant amount of the stress is relaxed since only -3.33GPa was measured. The cooling rate is an important parameter that needs consideration when measuring oxide stress on FeCrAlY alloys

Measuring stresses in the oxide scale that is thermally grown on a Pt-Al coating was more difficult than that of the FeCrAlY scale. The FIT technique was required because of the thin scale evident from TGA data. Adding to this difficulty is the surface roughness of the as-processed aluminide coating shown in Figure 46. Two effects from this surface morphology complicate the stress measurement. First, the variation in the surface normal vector introduces an error in the tilt angle (ψ). Second, tensile stress can be found on the tops of these ridges in the

scale. Ridges associated with this grain boundary network are a significant surface fraction that is convex and tensile stresses can develop in the oxide scale during cooling on these non-planar surfaces. Furthermore, this tensile stress would not be uniform through the thickness of the scale, but a gradient from tensile at the gas-oxide interface to compressive at the oxide-substrate interface would be present. Contributions from this tensile stress will be averaged with compressive stress and the result will be broader diffraction peaks and an erroneously low average compressive stress. As mentioned above, a low incident angle of 2° is used to increase the diffracted beam intensity. Only the top portion of the 5μm ridges will be diffracting in this geometry and not the oxide formed on the planar Pt-Al grain interiors because of incident x-ray beam shadowing increasing the ratio of curved to planar surface in the diffracting volume. Therefore, grain boundary ridges were polished to produce a smooth planar surface for XRD stress measurements and a micrograph of the polished surface is shown in Figure 59.

A polished Pt-Al coating was exposed for 120 hours at 1100°C. Following a slow cool to room temperature, a stress measurement was performed using (146) and a fixed low incident 2θ scan. The 2θ plot and results are shown in Figure 60. A smaller range of tilt angles was used because of the fixed incident geometry and as a result a smaller shift is apparent in the peaks as compared to those from the FeCrAlY. Another difference between the Pt-Al and FeCrAlY 2θ plots, is the reduction of peak intensity as the tilt angle increases. This is a result of beam spreading , defocusing, over the edge of the smaller Pt-Al sample as the specimen tilts. This spreading reduces the intensity of the incident x-ray beam and ultimately reduces diffracted beam intensities. This phenomenon could be seen in the FeCrAlY plot if the sample was tilted further than 80°.

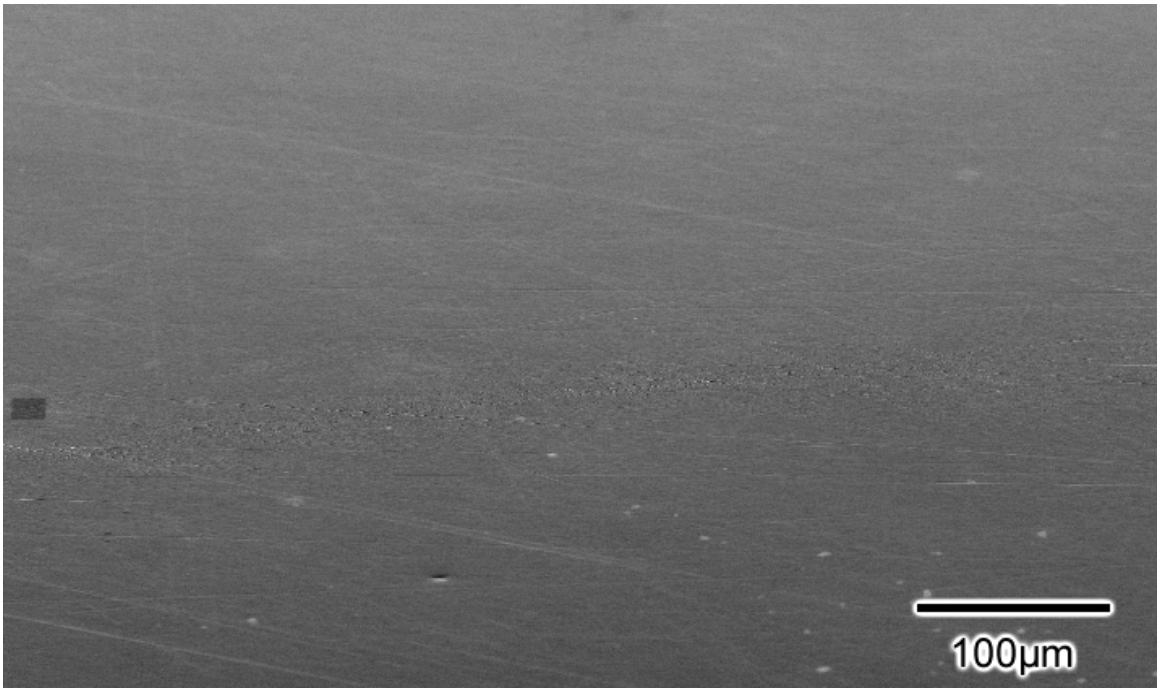

Figure 59. SEM micrograph of a polished Pt-Al surface used to grow a scale for stress measurement. The ridges present in the as-coated condition associated with aluminide grain boundaries have been ground off.

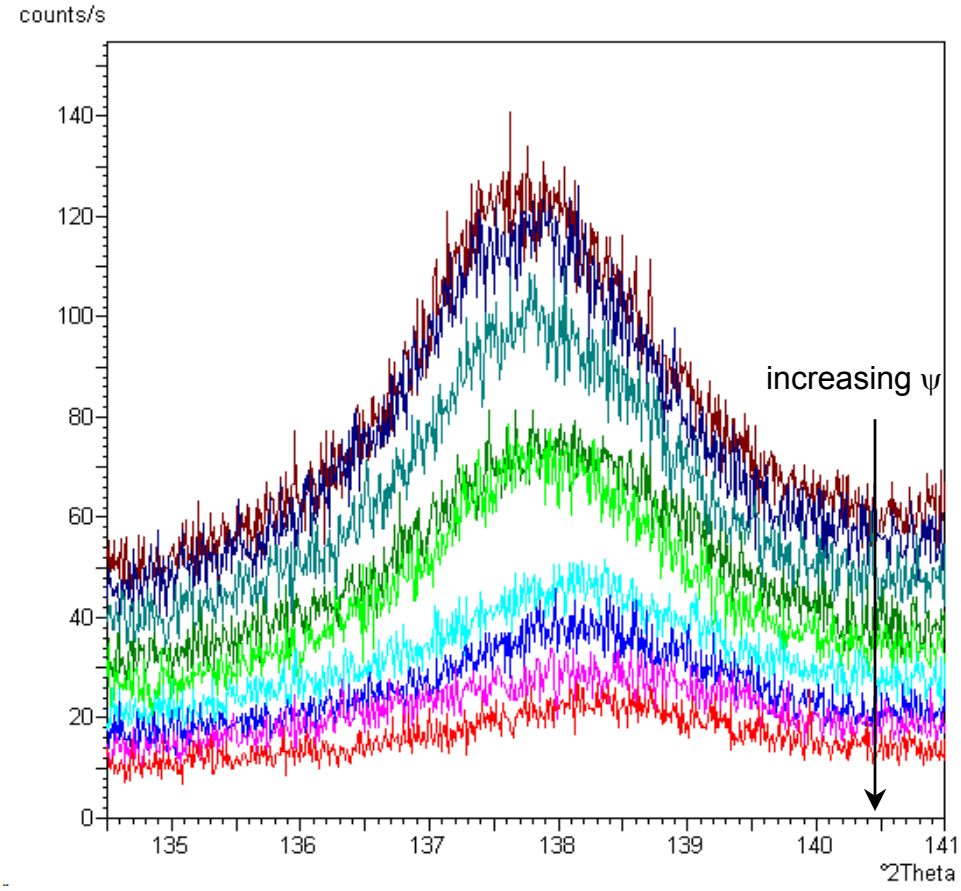

Figure 60. Plot of stress measurement 2θ scans (by fixed incident tilting) using the (146) peak of α-alumina formed on Pt-Al. The coating was exposed at 1100°C for 120 hours followed by a 1°C/min cool to ambient temperature

Results from the residual stress measurement are displayed in Figure 61 as a d-spacing versus $\sin^2\psi$ plot for the alumina formed on Pt-Al. A few peaks were not used in this plot and the curve fitting because of substrate peak interference, yet a linear relation was established for the (146). Stress values for (146), (226) and (1.0.10) are listed in Table 6 for both Voigt and Reuss models. This oxide scale exhibits the Voigt behavior with a stress value of -3.18GPa (average of stress values measured for (146), (226) and (1.0.10) peaks). The errors for associated with each measurement are larger than those from the FeCrAlY in the previous table as expected for the fewer peaks used and the narrower tilt range. Furthermore, a texture measurement was performed on this scale for validation of the use of this XRD technique and the necessary equations. Pole figures for the (012) and (110) peaks are presented in Figure 62 demonstrating a random orientation of alumina grains confirming this approach for XRD stress measurements.

Table 6. Residual stress measurement results for alumina scale on Pt-Al exposed to 1100°C for 120 hours slow cooled.

	Stress (GPa)	
Peak	Voigt	Reuss
146	-3.25 ± 0.16	-3.18 ± 0.16
226	-3.20 ± 0.31	-2.50 ± 0.26
1.0.10	-3.08 ± 0.42	-3.35 ± 0.45

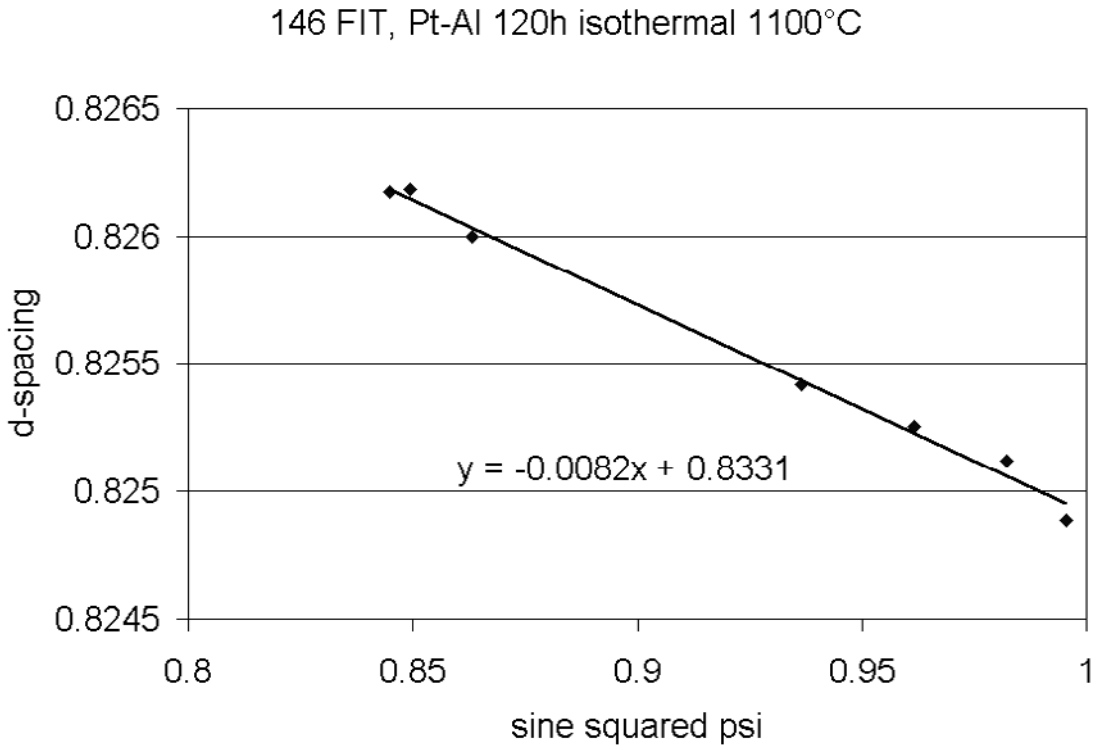

Figure 61. Plot of d-spacing versus $\sin^2\psi$ for the (146) obtained by fixed incident tilting method. Note the small range of tilt angles used in this measurement. The linear equation shown in the plot was fitted to the data and the slope is used for stress calculations.

(012)

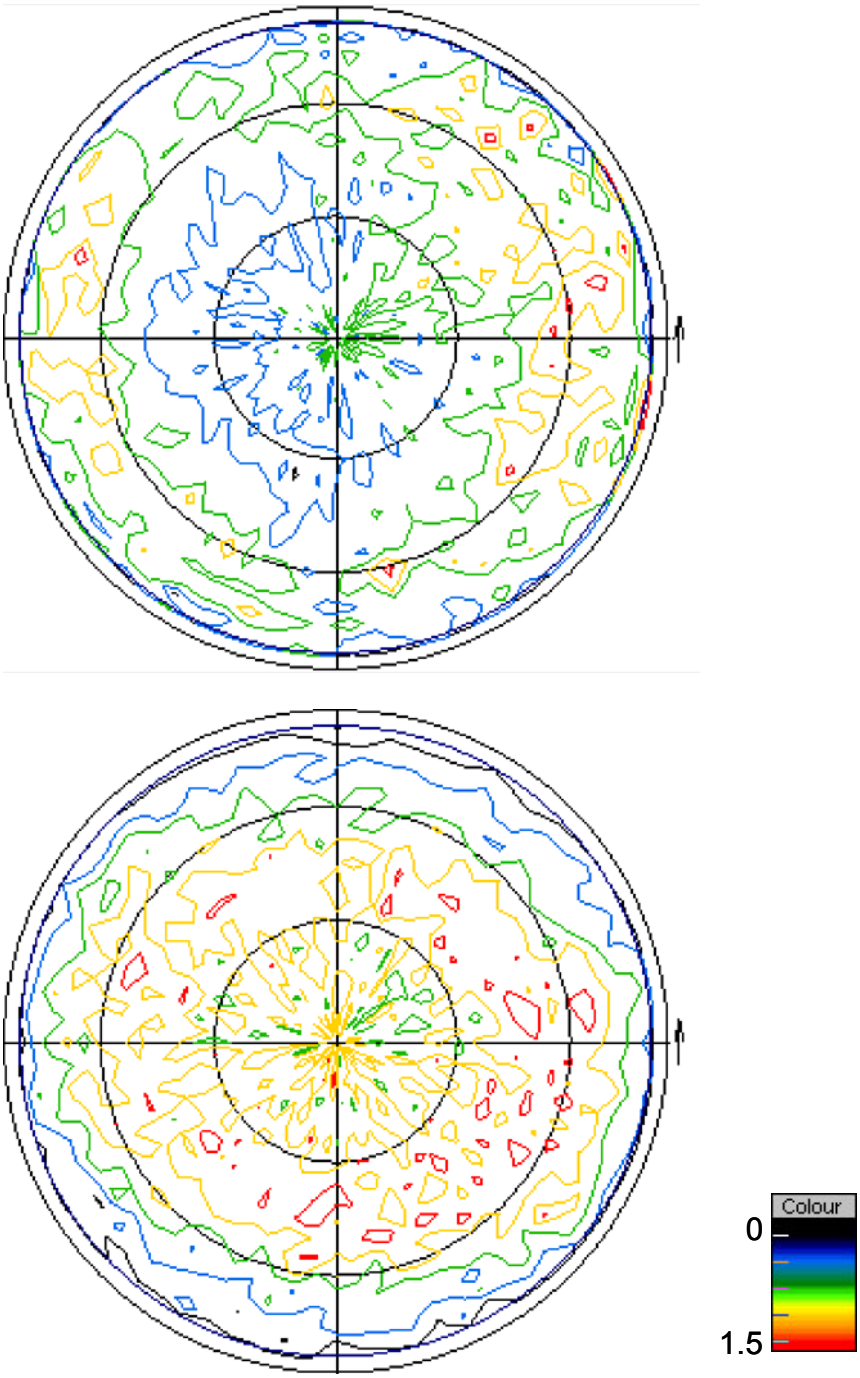

(110)

Figure 62. Pole figures for (012) and (110) alumina peaks of the scale formed on Pt-Al coating after 120 hour exposure at 1100°C. Intensities are normalized with respect to the average intensity.

Since the Pt-Al was a 50μm thick coating on an N5 substrate, the contraction that is induced into the alumina scale during cooling is not from CTE mismatch with the Pt-Al but the thermal strain caused by the mismatch with the thicker substrate. Therefore, the average CTE for a superalloy (16.6 x10^{-6}mm/mm/K[79]) is used in calculating the thermal stress in the alumina and this stress is –4.0GPa. This value is 800MPa larger than that of the measured residual stress in the alumina after a slow cool suggesting some stress relaxation. A stress measurement was performed on the same coating exposed to 1100°C for 124 hours with an air quench rather than a slow cool to reduce the effects of any stress relaxation. Results from measurements using (146) and (226) are listed in Table 7 for the Voigt and Reuss model. Like the slow cooled specimen, this scale also exhibits the Voigt behavior of constant strain, but this sample has an average stress of –4.08GPa. It appears that rapidly cooling the specimen eliminates any significant stress relaxation since this measured stress value agrees with the calculated thermal stress.

Table 7. Residual stress measurement results for alumina scale on Pt-Al exposed to 1100°C for 120 hours air quenched.

	Stress (GPa)	
Peak	Voigt	Reuss
146	-4.12 ± 0.54	-4.02 ± 0.53
226	-4.04 ± 0.46	-3.46 ± 0.39

This agreement between measured and calculated stresses for the rapidly cooled specimen suggests that an oxide scale growth stress in the alumina scale on Pt-Al is much smaller than that of the Fe-base alloy or nonexistent. Any relaxation not completely eliminated by rapid cooling could mask the existence of a growth stress. Therefore a high temperature stress measurement

was performed to clarify this problem. A Pt-Al sample was exposed for 100 hours at 1100°C in a laboratory furnace to grow an oxide layer thick enough for XRD eliminating unnecessary exposure on the hot stage. The specimen was air quenched and then fixed to the hot stage followed by specimen reheating. The rocking technique was used for measuring the change of d-spacing versus tilt angle and results for the (226) are listed in Table 8 for both elastic models. Within the errors of this measurement, a small growth stress exists, but the value is not large enough to dismiss that rapid cooling the specimen nearly eliminates stress relaxation in the Pt-Al system. Furthermore, the temperature history for this sample is shown in Figure 63 with results from residual stress measurements performed before and after the high temperature exposure with stress values of –3.93 and –3.99GPa respectively.

Table 8. High temperature stress measurement results for alumina scale on Pt-Al exposed to 1100°C for 124.

	Stress (GPa)	
Peak	Voigt	Reuss
226	-0.32 ± 0.15	-0.27 ± 0.13

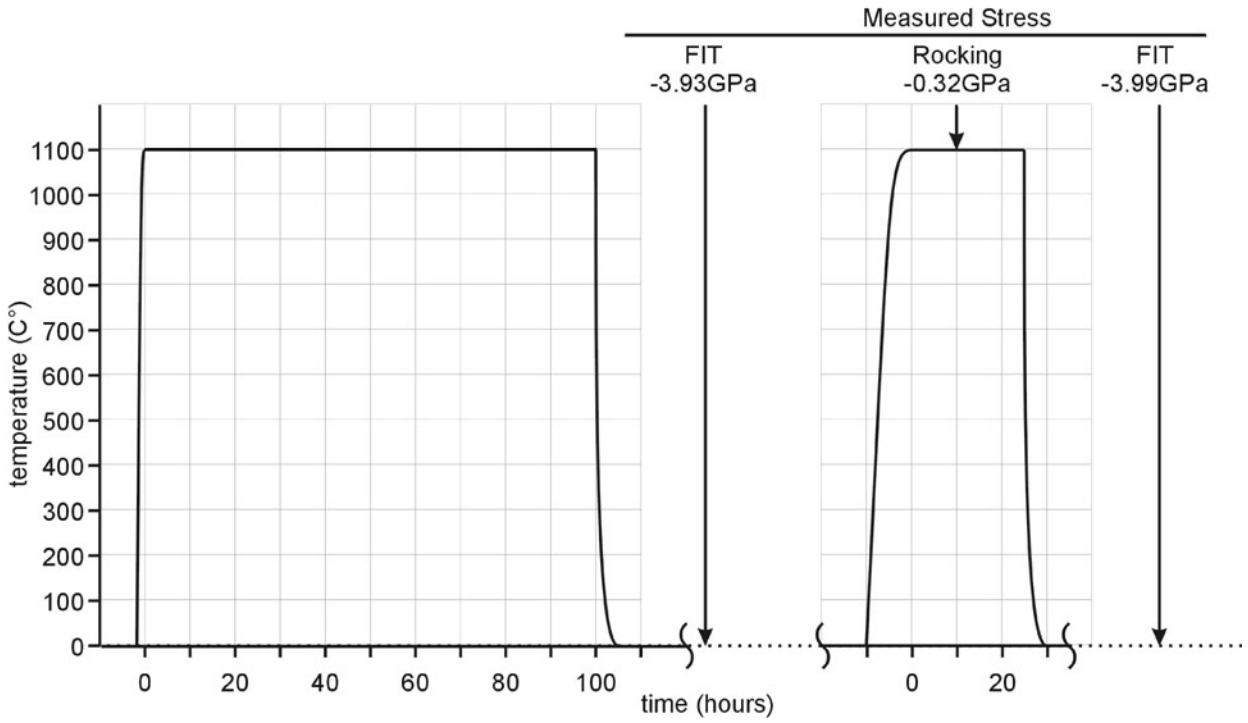

Figure 63. Temperature and stress history of Pt-aluminide coating.

Figure 64 is a SEM surface micrograph of the Pt-Al specimen after the 120 hour exposure at 1100°C with slow cooling. Although the sample was polished smooth for stress measurements, some surface modification is apparent as deformation along grain boundaries of the underlying aluminide coating. It appears that small growth stress and the thermal stress development as the sample cooled was large enough to result in either yielding or creep. Two Pt-Al specimens were thermally cycled at 1100°C to elucidate the mechanism. One specimen was polished like those used in stress measurement experiments and the other was exposed in the as-coated condition. Figure 65 presents surface micrographs of each specimen after 400 cycles. Figure 65a shows the deformation of the polished surface as valleys existing on the grain boundaries of the aluminide coating. A cross section micrograph of the same specimen in Figure 66 shows that the valleys are associated with the Pt-Al grain boundaries. The non-polished surface also exhibited deformation but instead of valleys, aluminide grain boundary ridges were heightened as shown in Figure 65b. Since it is evident that thermal cycling increases the amount of deformation of the Pt-Al surface and alumina scale, the thermal stress has more effect on this deformation than the high temperature growth stress.

a)

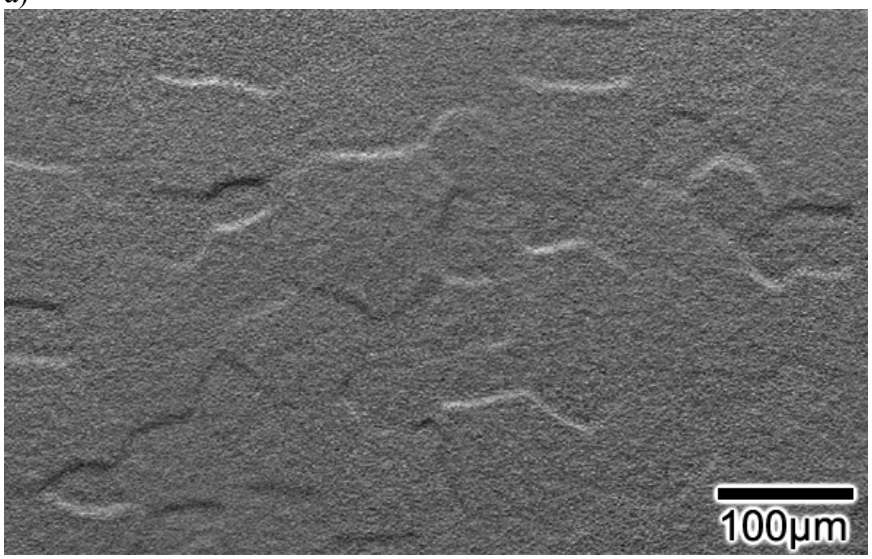

b)

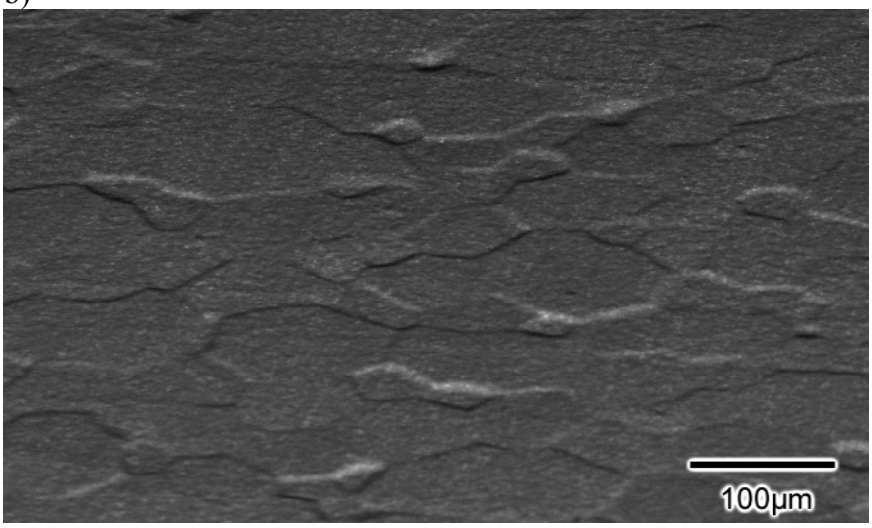

Figure 64. SEM Micrographs of the surface of the Pt-Al coating with the ridges removed after exposure at 1100°C for 120h a) normal view and b) low angle view

a)

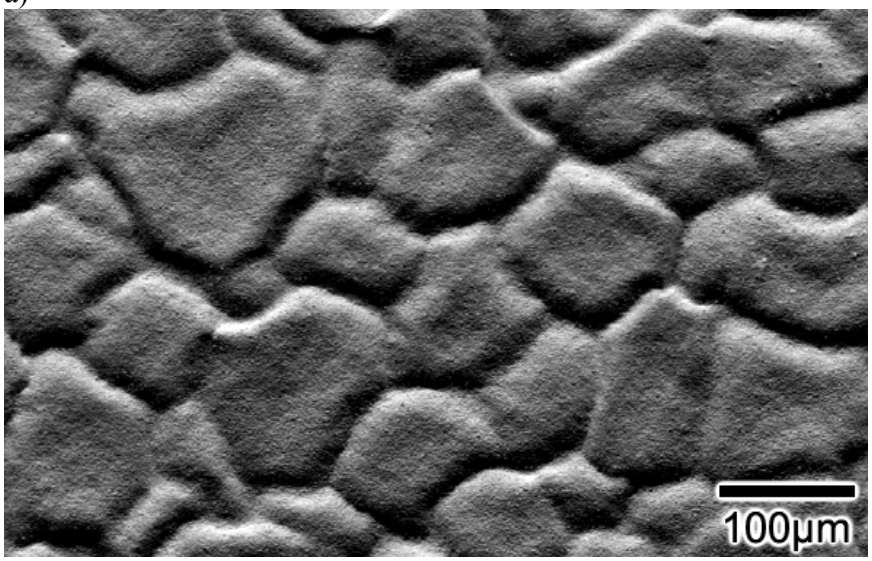

b)

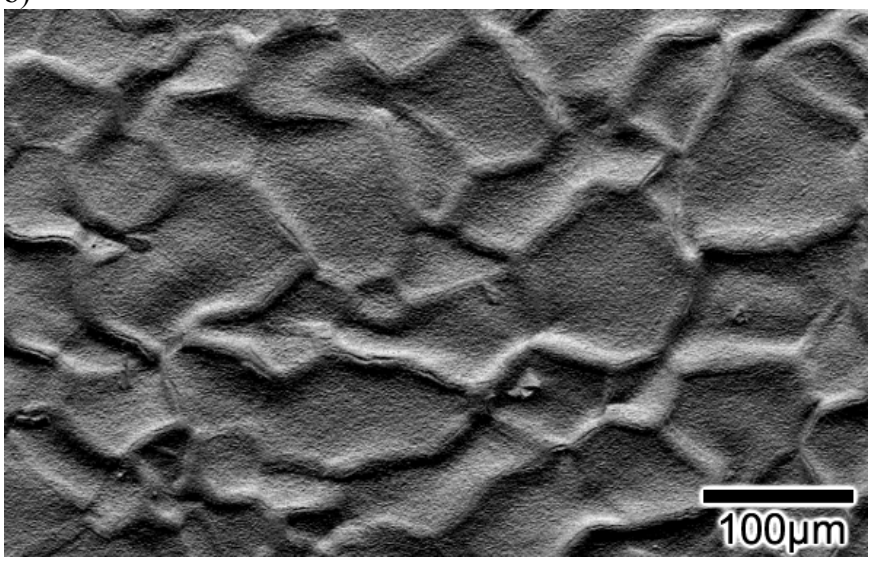

Figure 65. SEM surface micrographs of Pt-Al coatings after 400 cycles at 1100°C where a) the ridges were polished off and valleys formed at the aluminide grain boundaries and b) was not polished and larger peaks developed at the aluminide grain boundary ridges.

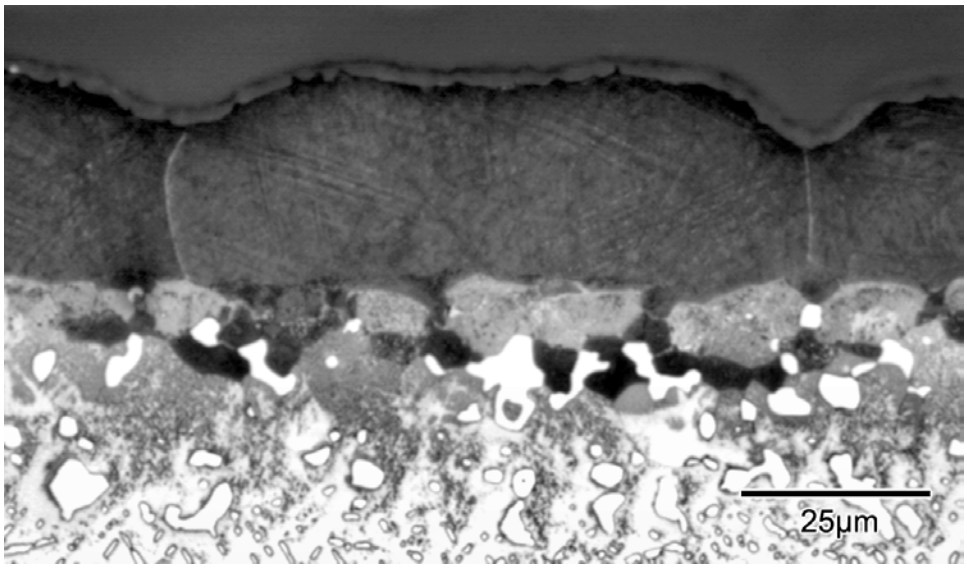

Figure 66. Optical cross section micrograph of a Pt-Al coating after 400 cycles at 1100°C. This specimen had a polished surface and aluminide grain boundaries are evident at the valleys.

Accompanying this scale deformation is a significant drop in the stress of the alumina scale determined by a residual stress measurement. Although grooves formed at the aluminide grain boundaries, a plateau was maintained on the interior portions of the substrate grains. The diffracting geometry of the FIT technique would not average the complicated stress state within these grooves, from incident beam shadowing, into the stress measurements of the scale on the plateaus. Results from this measurement are listed in Table 9 for the (146), (226) and (1.0.10) with an average stress of –1.84GPa. This was the only scale to exhibit the Reuss behavior and the least stressed oxide scale in this investigation. The oxide stress was also measured by piezospectroscopic analysis with a value of –2.1GPa with a standard deviation of 81MPa[80]. Since the spatial resolution of this technique (approximately the diameter of the laser) is much higher than that of XRD, the stress value is averaged over the plateaus and valleys of the sample and agrees well with XRD data. The low stress state and the amount of deformation has allowed the alumina grains more freedom to approach a uniform stress state rather than the confined grains of other exposure conditions where the Voigt behavior is observed[81].

Table 9. Residual stress measurement results for alumina scale on Pt-Al exposed to 400 cycles at 1100°C.

	Stress (GPa)	
Peak	Voigt	Reuss
146	-1.89 ± 0.26	-1.85 ± 0.25
226	-2.10 ± 0.32	-1.80 ± 0.25
1.0.10	-1.73 ± 0.24	-1.88 ± 0.26

Stress measurements on the oxides formed on superalloys has proven to be difficult with the thin transient layer the forms on top of the alumina scale. Fortunately, colleagues at UCSB have been

able to produce alumina scales on 1484 where transient oxides would completely spall during cooling[82]. The alloy was exposed to 1200°C for 16 hours. Although this temperature was higher than the temperature of interest of 1100°C, there was an opportunity to measure the stresses in the alumina layer thermally grown on a superalloy by XRD. Results for residual stress measurements are listed in Table 10 for the (146) and (226) for two orientations in the diffractometer. The first measurement was during the original placement of the specimen in the diffractometer ($\phi = 0°$) and the second was performed after the specimen was rotated 30° about the surface normal ($\phi = 30°$). These results, listed in Table 10, cannot be used to determine whether the scale exhibits Reuss or Voigt behavior and these results do not agree with each other for a given model within the errors of each measurement. Further review of the 2θ scans shows anomalous maxima and minima in peak intensities with respect to the tilt angle, as shown in Figure 67, suggesting a preferred orientation of alumina grains. Another result indicating a possible texture is the non-linear or curvature shown in the d-spacing versus $\sin^2\psi$ plot of Figure 68. A conclusive texture analysis revealed a preferred orientation of alumina grains evident in the (012) and (110) pole figures for the alumina scale in Figure 69. Applying the linear relation into the d-spacing versus $\sin^2\psi$ relationship and the calculation of the XEC from single crystal elastic data outlined in Equations 35-37 can only be used for a scale with a random grain orientation distribution. Forcing this approach on the alumina scale formed on 1484 is inaccurate, hence the discrepancies in stress values reported in Table 10. Using XRD for stress measurements on textured materials requires a known grain orientation distribution and unique x-ray elastic constants based on this distribution for an accurate stress calculation.

Table 10. Residual stress measurement results for alumina scale on 1484 exposed to1200°C for 16 hours.

	Stress (GPa)	
ϕ=0°		
Peak	Voigt	Reuss
146	-4.75 ± 0.37	-4.64 ± 0.36
226	-5.25 ± 0.25	-4.49 ± 0.22
ϕ=30°		
Peak	Voigt	Reuss
146	-4.41 ± 0.31	-4.31 ± 0.30
226	-6.00 ± 0.19	-5.14 ± 0.16

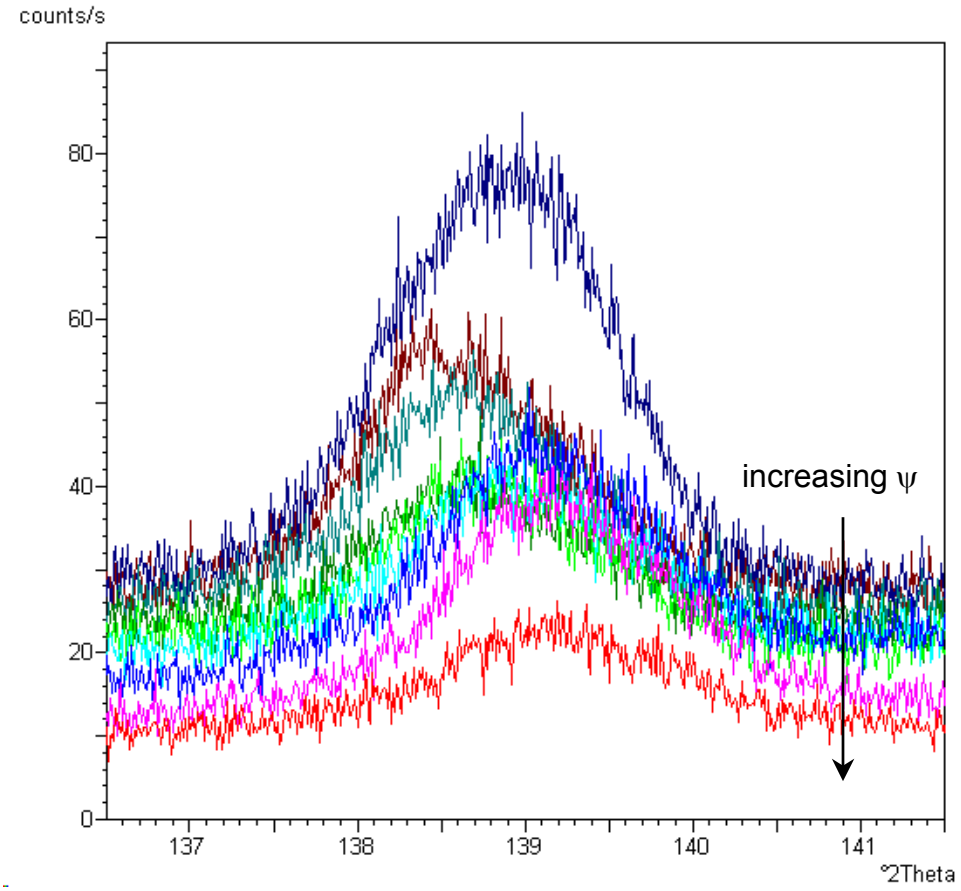

Figure 67. Plot of stress measurement 2θ scans (by fixed incident tilting) using the (146) peak of α-alumina formed on PWA 1484. The specimen was exposed at 1200° for 16 hours and the transient oxide spalled uncovering an intact alumina.

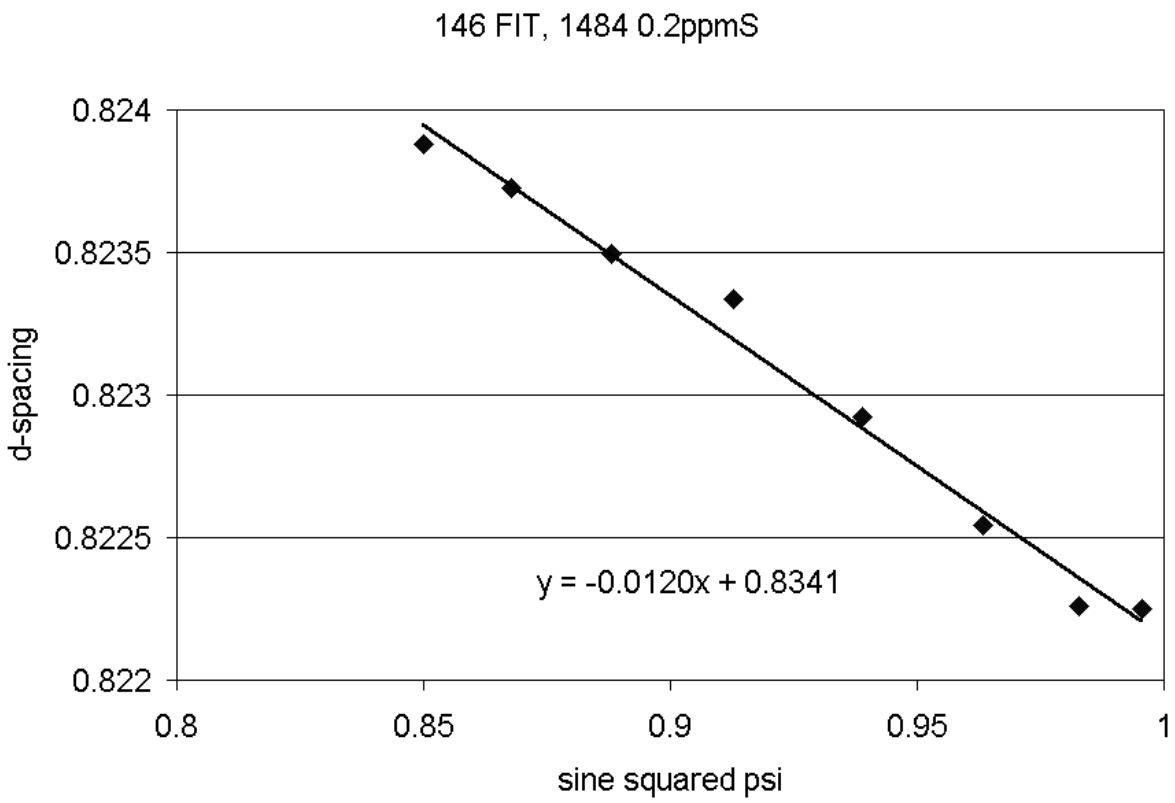

Figure 68. Plot of d-spacing versus $\sin^2\psi$ for the (146) obtained by fixed incident tilting method. Note the small range of tilt angles used in this measurement. The linear equation shown in the plot was fitted to the data and the slope is used for stress calculations.

(012)

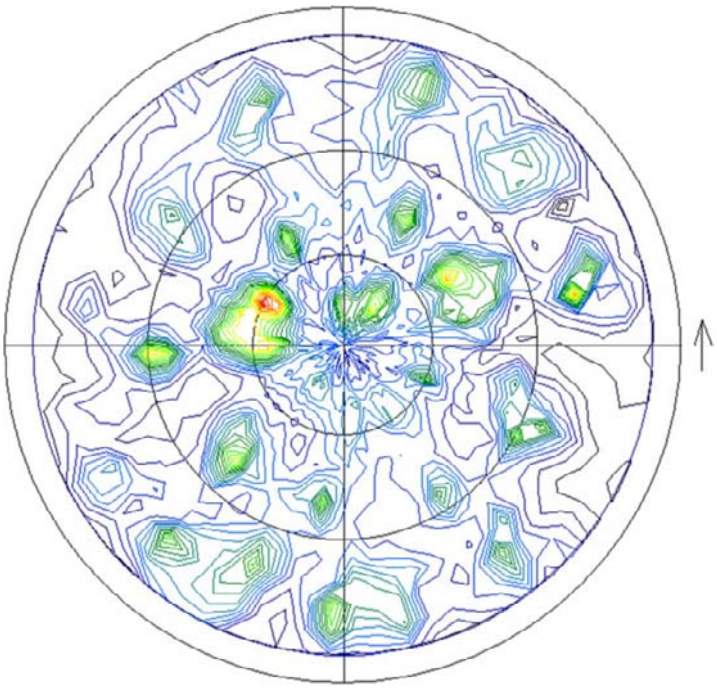

(110)

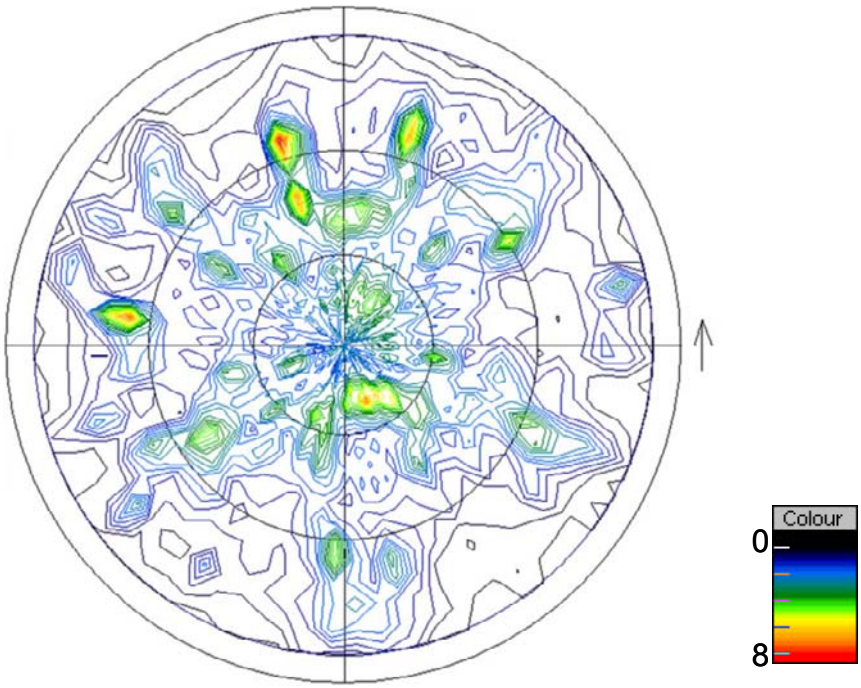

Figure 69. Pole figures for (012) and (110) alumina peaks of the scale formed on 1484 alloy after 16 hour exposure to 1200°C. Intensities are normalized with respect to the average intensity.

Stress measurements have been performed on the alumina scale formed on a polycrystalline alloy referred to as PolyXL that has the same composition as the single crystal 1484[64]. The material was exposed at 1100°C, the temperature of interest for this work, and a residual stress of –3.9GPa was measured. Also, high temperature stress measurements could not detect a growth stress in the scale which adds support to the residual stress agreeing well with a calculated thermal stress of –4.0GPa. A compilation of stress values are listed in Table 11 summarizing results and lists the stress values used for calculating Q_o.

Table 11. Compilation of oxide stress after scale growth at 1100°C and slow cooling.

Materials	Calculated Thermal Stress(GPa)	Measured Growth Stress (GPa)	Measured Residual Stress (GPa)
Pt-Al	-4.04	~-0.25	-3.18
Ni-Al (St-Al)		~0†	-3.18‡
PolyXL (superalloys)	-4.0	~0†	-3.9†
FeCrAly	-2.5	~-1.3†	-3.33

† Measured by Sarioglu et.al.[68]
‡With negligible growth stress, St-Al value is assumed to be the same as that of Pt-Al

5.6 DETERMINATION OF B

Monitoring a spallation event with a known fracture energy by the acoustic emission technique would provide a direct means to determine B, the ratio of acoustic energy to fracture energy. Since this fracture energy or size of each spallation event is unknown, an indirect method to determine B is discussed in the following. The variables in Equation 50 can be measured by short-term testing, as described above, or are readily available in the literature. These include E^{AE}, W'_r, ρ, A, and stored elastic strain energy (via stress measurements and elastic constants).

The two unknown parameters are Q_o and B and by obtaining the spall parameter used in the COSP, B can be calculated.

Using the model, Q_o is obtained from longer-term cyclic oxidation results and isothermal TGA experiments by utilizing the model in reverse. Instead of entering inputs into the model to generate the cyclic oxidation curve, the long-term data is used to obtain Qo. The dependence of cyclic oxidation life (cycles to negative weight change) is plotted in Figure 33 where only the growth kinetics of the scale are required for construction. Long-term cyclic oxidation lives for 1484, LS N5 and the St-Al coating have been experimentally obtained and cycles to failure are marked in a similar life-time plot in Figure 70. Intersection of modeled life-time curves and the experimentally determined cycles to failure (horizontal dashed lines) mark the value of Q_o for the particular material. These Q_os are listed in Table 12 for these three materials and each Q_o is used in Equation 50 with the other experimental parameters to determine B for each material. Since B is assumed to be a constant (only a function of the experimental apparatus), the average value of $B = 5.99\text{x}10^{13}\text{mV}^2\text{s/J}$ is obtained. This average value is used as the experimental constant in for Q_o calculations for all materials and coatings.

Table 12. Spall factor obtained from long-term cyclic oxidation experiments

Alloy/Coating	Life-Time from Long-Term Test (n)	Q_o (cm^2/mg)	B ($\text{mV}^2\text{s/J}$)
1484	24	0.067	1.83E+13
LS N5	600	0.0017	4.27E+13
St-Al	1000	0.0027	1.19E+14

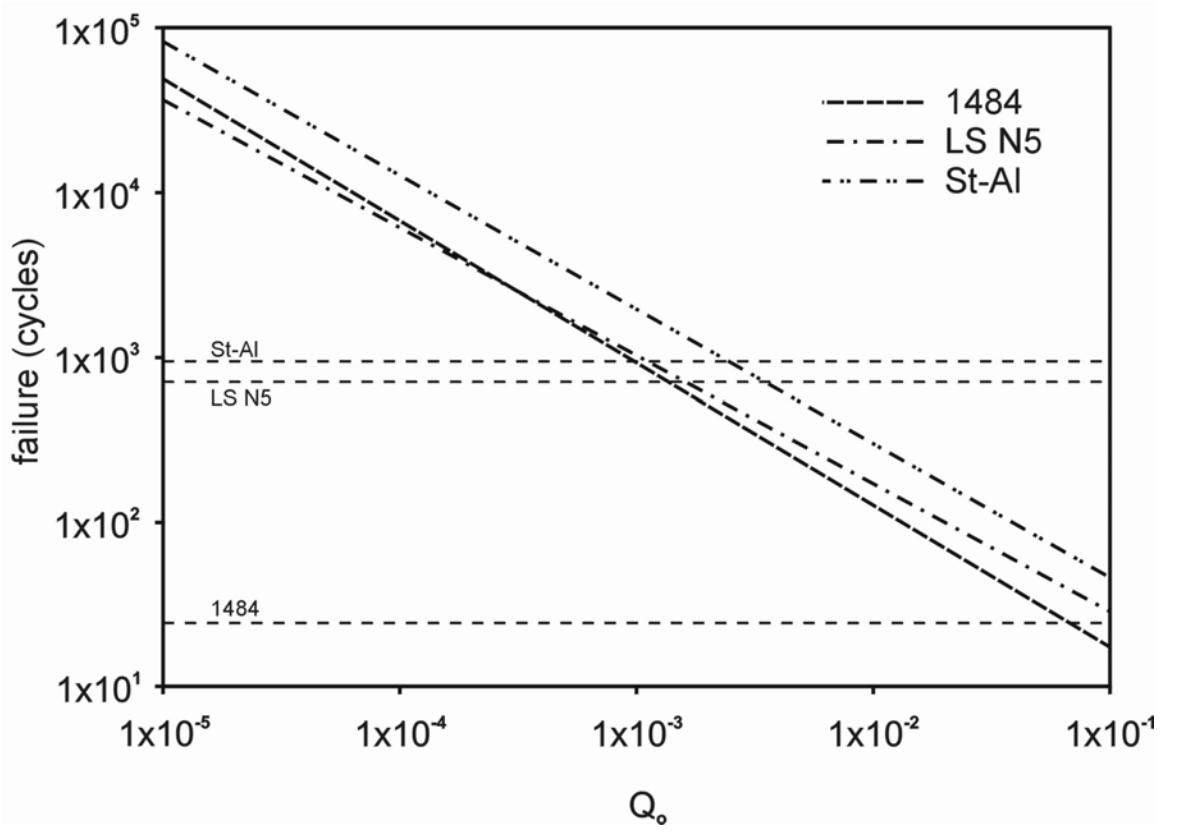

Figure 70. Plot of cyclic oxidation life-time versus Q_o with life-time curves for 1484, LS N5 and St-Al. Long-term cyclic oxidation life for each material is represented as a horizontal dashed line. Intersection of life-time curve and the horizontal line for each material represents the Q_o for each material.

5.7 CORRELATION OF RESULTS

Finally, all of the necessary variables have been attained for calculation of Q_o for use in the COSP. Stresses have been measured to determine the elastic strain energy stored in the alumina scale. TGA provides the data to calculate *W'r* (and isothermal growth kinetics) and a novel acoustic emission experiment has been developed to measure the amount of oxide spallation. This data and a known scale density are used to calculate Q_o, an input into COSP. Figure 71 is a life-time plot demonstrating the modeled life-time curves with data points on each material curve marking the expected cycles to failure according to the calculated Q_o. Table 13 compares the long-term data to the data obtained form the short-term tests and model. Although *B* was obtained from longer-term cyclic oxidation data from 1484, LS N5 and St-Al data, the agreement of projected lives with the limits of this technique is remarkable. Furthermore, taking this experimental data and extrapolating it to materials exhibiting longer cyclic oxidation lives, namely Pt-Al coating and FeCrAlY, adds support to the validity of this approach to life-time prediction for cyclic oxidation experiments.

Table 13. Comparison of long-term and predicted cyclic oxidation lives

Alloy/Coating	Cycles to Failure (n)	
	Long-Term Test	Short-Term Tests and Model
1484	24	64
LS-N5	600	950
St-Al	1000	560
FeCrAlY	>2000	3850
Pt-Al	>4000	10000

In addition to exposures at 1100°C, the Pt-Al coatings were oxidized for 24hours during AE experiments at exposure temperatures of 1050°C and 1150°C. This series of experiments provides data to show the effect of temperature on the calculated life-time from short-term test data. The cyclic oxidation life can be calculated for each exposure temperature from this AE data and with approximations of the other model inputs used in equation 50 to calculate Q_o. TGA experiments, to obtain isothermal growth kinetics, and XRD residual stress measurements were not performed on the Pt-Al coating specimens exposed at 1050°C and 1150°C. Therefore, these values were approximated with the following assumptions. First, the scale growth rate at each temperature was determined from the Arrhenius behavior of the growth rate coefficient with an activation energy of –360kJ/mole[83]. Second, the measured residual stress in the alumina scale formed at 1100°C with a slow cool of -3.18GPa was applied to the other exposure temperatures. This constant stress value was used rather then prorating the residual stress for each exposure temperature since prorating would imply the scale stress forming and stress relaxation mechanisms are constant over the entire temperature range. This is not the case since the propensity of stress relaxation by creep or yielding is greater at the higher temperatures resulting in relaxation of thermal stress that develop at the start of cooling. Finally, the experimental parameter B is also held constant for each temperature since the majority of the AE data is emitted near room temperature and any of the high temperature cracking is insignificant. Since most of the data is collected near room temperature, any effect of temperature on the acoustic detection efficiency can be neglected. All experimental variables necessary to determined Q_o and the results from the model (Q_o and ultimately cycles to failure) are presented in Table 14. Although no long-term cyclic oxidation data is presented to support these short-term tests and modeled lives over this temperature range, the trend of decreasing cycles to failure

with increasing exposure temperature is established. As expected, the longest cyclic oxidation life occurs with exposure to 1050°C, but associated with this long life is the largest Q_o, suggesting that Q_o is sensitive to temperature. This approach was not applied to the LS-N5 alloy since the differences were apparent in the types of oxide that formed at the higher and lower temperatures negated similar approximations to determine the growth rate and residual stress of the oxide scale.

Table 14. Pt-Al modeled cyclic oxidation input parameters and life.

Exposure T	E^{AE}	Residual Stress	Scale Growth Coefficient	Q_o	Cylces to Failure
1050°C	12	-3.18GPa	0.0262	5.29×10^{-4}	12000
1100°C	53	-3.18GPa	0.0857	2.19×10^{-4}	10000
1150°C	693	-3.18Gpa	0.2596	3.11×10^{-4}	2400

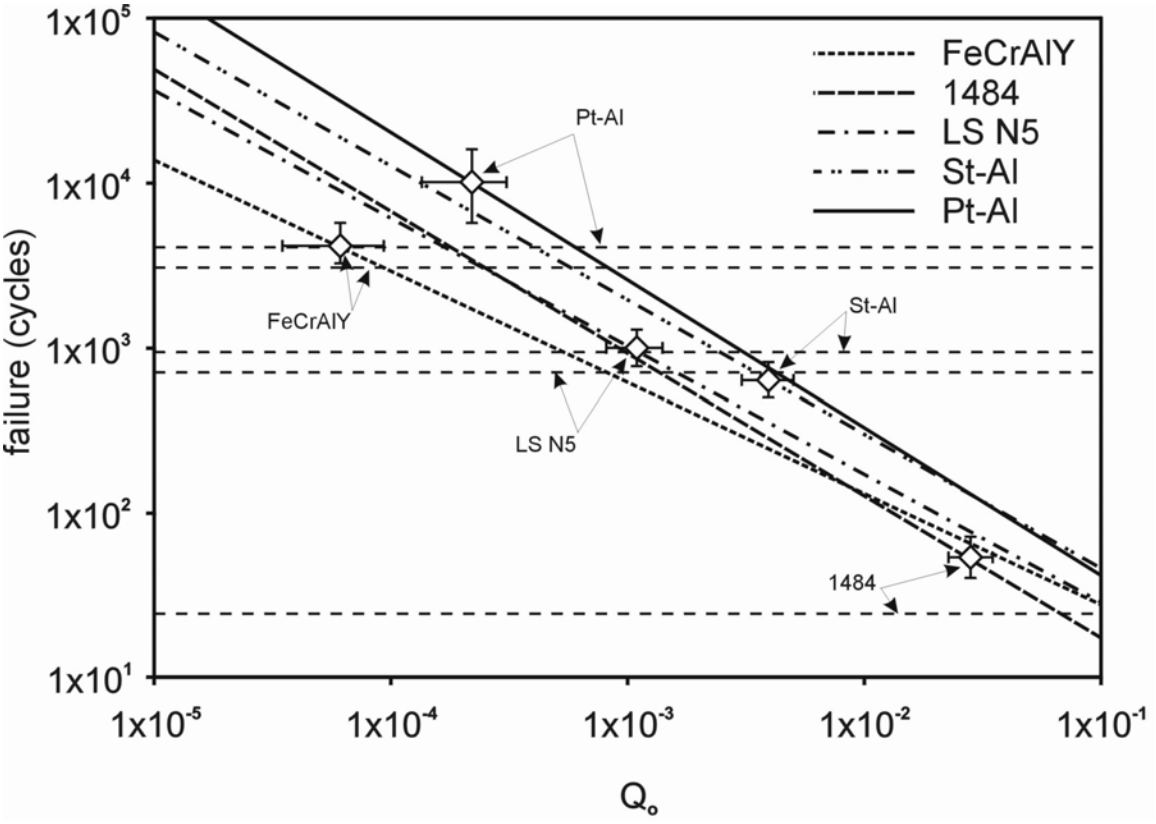

Figure 71. Plot of cyclic oxidation life-time versus Q_o with life-time curves for 1484, LS N5 St-Al, FeCrAlY and Pt-Al. Long-term cyclic oxidation life for each material is represented as a horizontal dashed line. Data points mark the position on the curve determined by the Qo obtained by short-term testing. Error bars were determined from AE reproducibility experiments. Horizontal lines represent cyclic oxidation life-times obtained from long-term testing.

6.0 CONCLUDING REMARKS

This investigation produced a short-term testing protocol for cyclic oxidation life-time prediction. The method utilizes an existing cyclic oxidation model, COSP, with inputs of oxide type (in this study, only alumina formers where used with the model), thermal cycle of interest, isothermal scale growth kinetics and scale spallation behavior during cooling. The model calculates oxide formation and spallation for each cycle and records the progress of variables such as metal consumption and retained oxide to generate mass change curves similar to those obtained by long-term cyclic oxidation tests. This type of curve generation is then used to compare modeled results with long-term cyclic oxidation experimental data. Rather than statistically fit long-term cyclic oxidation data to the model to determine the inputs as proposed by the original authors, short-term experiments were designed to quantify these inputs. The oxide growth kinetics were measured by classical TGA experiments where oxygen uptake during oxidizing exposures was monitored, but a novel approach was developed to quantify the scale spallation behavior. COSP utilizes one value, Q_o, to quantify the amount of oxide that spalls during cooling in each cycle. Reversing the approach in the model, Q_o was defined as a function of the amount of scale that spalls. By applying physical significance to this parameter, it can be quantified from acoustic emission experiments, XRD stress measurements and isothermal TGA results. Measured scale growth and spallation parameters are then used to generate modeled long-term cyclic oxidation behavior.

The results from the short-term testing and modeled cyclic oxidation lives have been compared to long-term data with good agreement. The largest discrepancy between modeled and actual performance is apparent with the Pt-Al coated superalloys where the estimated cyclic oxidation life of 4000 cycles is much less than the 10000 cycles predicted by the model with inputs form short-term testing. Although the 4000 cycles to failure was extrapolated from cyclic oxidation data of only 2200 cycles, where no net mass loss was evident, the ability of the coating to last for 10000 cycles is improbable due to the following. There is a minimum concentration of aluminum in the coating required to maintain the growth of an alumina scale. This aluminum in the coating is consumed during the cyclic oxidation process of scale growth, scale spallation and scale reformation reducing the aluminum concentration. Aluminum also diffuses into the substrate, which has a lower aluminum content than the coating, further reducing the aluminum content of the coating. Since the Pt-Al is utilized as a thin 50μm coating, the aluminum reservoir is not as stable or long lasting as that of a bulk alloy, so the loss of aluminum by selective oxidation and diffusion into the substrate suggests that coating conditions will not be constant throughout the lifespan of the coating. Furthermore, these changing conditions will alter the scale growth kinetics and spall behavior reducing the validity of the modeled life-times. This type of phenomenon is not an issue with the other alloys and coating. The aluminum reservoir for the bulk alloys were large enough to keep the conditions relatively constant at the metal-oxide interface and the short failure time of 690 cycles for the St-Al coating might have reached failure prior to any large composition change by selective oxidation and diffusion of aluminum.

Through the development of this procedure for cyclic oxidation life prediction, the limitations of this approach have been identified. These limitations will be discussed in the following. This

short-term testing and modeling technique is only valid for materials exhibiting mechanical failure, not the type of chemical failure expected for the Pt-Al. This chemical failure ensues after selective oxidation has altered the substrate whereby the degradation mode has changed. In contrast, mechanical failure is the loss of specimen mass by the cracking and spallation of the oxide scale. The validity of the model is based on a constant mechanical failure mode through the modeled life span for the material.

Another aspect of concern for this testing method is with detection of oxide loss with the acoustic emission (AE) equipment. AEs are elastic waves generated by the fracture event and this event of interest in this investigation is the cracking and spallation of the oxide scale. The quantification of the amount of oxide loss requires that the spallation occurs by a fracture event where a significant amount of energy is released. Any scale loss as a result of slow crack propagation might not be detected due to the slow release of acoustic energy or by a mechanism where a reduction in stored elastic strain energy prior to spallation would produce low acoustic activity. Such a process reducing the stored elastic strain energy could be void formation at the metal-oxide interface or plastic deformation preceding the fracture. This limits the application of the developed test to oxide scales that spall by a fracture process for accurate interpretation. Therefore, of the alloys and coatings used in this investigation were those which generally form adherent alumina scales with little void formation at the interface.

It has been shown that interfacial void formation is significant between the alumina scale and NiAl alloy. Bulk specimens of stoichiometric NiAl which have been exposed to 1100°C for 56 hours exhibit this behavior[84]. Although the St-Al coating is basically NiAl, interfacial void

formation is not significant enough to interfere with the stress state of the oxide or AE data in this investigation.

The above issue dealt with reduction in fracture energy prior to spallation, yet another scenario was made apparent by the nickel specimens that showed no signs of spallation during thermal cycling, yet cracking was detected during cooling. Since the mass change from cyclic exposures was larger than those of isothermal experiments, the cracking reduced the protectiveness by allowing rapid oxidation apparent from the higher mass gain of cyclic exposure as compared to isothermal exposure. This type of cracking without spallation is not applicable to this developed testing and modeling technique. Furthermore, microstructural observations are required to correlate AE data to cracking and spallation for validation of this approach.

The experimental constant B is the ratio of measured acoustic energy to the fracture energy of the event. Since the measured acoustic energy is dependent on the elastic wave transmitted to the transducer and the sensitivity of that transducer, the acoustic energy recorded is a function of the experimental apparatus. Therefore, B is sensitive to the setup and is dependent on the physical aspects of the transducer, wave-guide and the attachment of the specimen to the wave-guide. A fundamental study of the effects of the experimental apparatus on B or the E^{AE} was not performed since all parameters were held constant in this investigation. However, one needs to be aware of the variation of B when comparing results from one apparatus to another.

Finally, a framework has been constructed for cyclic oxidation life-time prediction. Unfortunately, the variability of oxidation behavior from sample to sample and the error in AE

data limits this approach, in the current state, to ranking the cyclic oxidation behavior for materials not directly studied in this investigation. Although caution should be used for applying this method to other materials, the original work presented in this paper provides a basis for future studies concerned with the high temperature oxidation resistance of alloys and coatings. The major contributions are summarized in the following:

- modification of an existing model by applying physical significance to input parameters
- developing a testing method to determine the model inputs
- refinement of XRD stress measurement technique by development of a multiplane technique to determine the elastic behavior of the material for accurate results
- development of AE testing technique and associated operating practice for *in. situ*. monitoring and quantification of scale damage during scale growth and thermal cycling.

7.0 FUTURE WORK

A protocol for short-term testing to obtain input parameters into a cyclic oxidation model has been developed in this investigation. During the development of this short-term testing technique, a number of aspects considered for additional study have been identified. Such information would provide further support to this methodology as a viable means of cyclic oxidation life prediction. This future work could include, but not be limited to the following:

- Application of this method to an elemental metal that only formed one type of oxide. This would eliminate any change in the oxidation kinetics and possibly maintain a constant degradation mode. This approach was attempted with pure Ni but the lack of scale spallation, which is required for quantification of scale loss by AE techniques, rendered it unsuitable.

- Another improvement would be the development of an independent experiment to determine B. Since B is the ratio of the measured E^{AE} to fracture energy of any fracture event, it would be possible to obtain B from a similar fracture event of known magnitude with the experimental apparatus.

- The model in the form used to predict cyclic oxidation behavior could be modified to include the consumption of the oxide forming element. The depletion of this element

could then be calculated via scale loss to a critical value. Although the critical concentration must be predefined, this could provide a criterion to determine lives of coatings where the reservoir of scale forming element is limited as compared to a bulk alloy.

- The error analysis employed in this work does not completely describe this complex problem with the spread of cyclic oxidation lives from both the short-term and long-term data. With the variation in the AE data and that of material performance from sample to sample may warrant a complete statistical analysis to generate probability of failure rather than an averaged value of cycles to failure with the associated variance to describe cyclic oxidation life.

- Using this short term testing approach in a range of exposure conditions. All of the results presented in this paper pertain to cyclic oxidation where the cycle is 45 minutes at 1100°C and 15 minutes at room temperature. Testing at different temperatures and cycle frequencies would show the range in which this approach is valid.

BIBLIOGRAPHY

[1] Schilke P. W., "Advanced Gas Turbine Materials and Coatings," GE publication GER-3569F, (1996).

[2] Birks N. and Meier G. H., "Introduction to High Temperature Oxidation of Metals," Edward Arnold Publishers, London, (1983).

[3] Wagner C., "Theoretical Analysis of the Diffusion Processes Determining the Oxidation Rate of Alloys," Journal of the Electrochemical Society, 99(10), 369–380, (1952).

[4] Evans H. E., Donaldson A. T. and Gilmour T. C., "Mechanisms of Breakaway oxidation and Application to a Chromia-Forming Steel," Oxidation of Metals, 52, 379-402, (1999).

[5] Adam N. K., "Physics and Chemistry of Surfaces", Oxford University Press, London (1941).

[6] McDonald J. E. and Eberhart J. G., "Adhesion of Aluminum Oxide-Metal System," Trans of Met. Soc. Of AIME, 233, 512 (1965).

[7] Fromhold Jr. A. T., "Stress and Dielectric Contact Layer on Metal," Surface Science, 22, 396-410 (1972).

[8] Smialek J. L., "The Effect of Sulfur Content on Al2O3 Scale Adhesion," Microscopy of Oxidation, Cambridge, UK, March 1990,(London, The Institute of Metals), 258-270 (1991).

[9] Grabke H. J., Wiemer D. and Viefhaus H., "Segregation of Sulfur During Growth of Oxide Scales," Applied Surface Science, 47, 243-250, (1991).

[10] Grabke H. J., Kurbatov G. and Schmutsler H. J., "Segregation Beneath Oxide Scales," Oxidation of Metals, 43, 97-114, (1995).

[11] Smeggil J. G., Funkenbusch A. W. and Bornstein N. S., "A Relationship between Indigenous Impurity Elements and Protective Oxide Scale Adherence Characteristics," Metallurgical Transactions, 17A, 923-932, (1986).

[12] Luthra K. L. and Briant C. L., "Mechanism of Adhesion of Alumina on McrAlY Alloys," Oxidation of Metals, 26, 396-416, (1986).

[13] Hou P. Y. and Stringer J., " Oxide Scale Adhesion and Impurity Segregation at the Scale/Metal Interface," Oxidation of Metals, 38, 323-345, (1992).

[14] Fox P., Lees D. G. and Lorimer G. W., " Sulfur Segregation During the High-Temperature Oxidation of Chromium," Oxidation of Metals, 36, 491-503, (1991).

[15] Briant C. L. and Mulford R. A., "Surface Segregation in Austenitic Stainless Steel," Metallurgical Transactions A, 13, 745-752, (1982).

[16] Whittle D. P. and Stringer J., "Improvements in High Temperature Oxidation Resistance by Addition of reactive Elements or Oxide Dispersions," Philosophical Transactions of the Royal Society, A295, 309-329, (1980).

[17] Funkenbusch A. W., and Smeggil J. G. and Bornstein N. S., "Reactive Element-Sulfer Interaction and Oxide Scale Adherence," Metallurgical Transactions, 16A, 1164-1166, (1985)

[18] Felten E. J., Electrochem. Soc, 108, 490-502, (1961)

[19] Tien J. K. and Pettit F. S., Metallurgical Transactions, 3, 1587-1596 (1972).

[20] Golightly F. A., Stott F. H. and Wood, G. C., Oxidation of Metals, 10, 163-175, (1976)

[21] Schumann E., Yang J. C., Ruhle M. and Graham M. J., " High-Resolution SIMS and Analytical TEM Evaluation of Alumina Scales on B-NiAl Containing Zr or Y," Oxidation of Metals, 46, 37-49, (1996)

[22] Antill J. E. and Peakall K. A., "Infuence of an Alloy Addition of Yttrium on the Oxidation Behavior of an Austenitic and a Ferritic Stainless Steel in Carbon Dioxide," Journal of the Iron and Steel Institute, 205, 1136-1142, (1967)

[23] McDonald J. E. and Eberhart J. G., "Adhesion of Aluminum Oxide-Metal System," Trans of Met. Soc. AIME, 233, 512 (1965).

[24] Smeggil J. G., Funkenbusch A. W. and Bornstein N. S., "A Relationship between Indigenous Impurity Elements and Protective Oxide Scale Adherence Characteristics," Metallurgical Transactions, 17A, 923-932, (1986).

[25] Pilling N. B. and Bedworth R. E., "The Oxidation of Metals at High Temperatures," J. Inst. Met., 29, 529-591, (1923).

[26] Horibe S. and Nakayama T., "Initial Formation of Oxide Nodules Due to the Grain Growth of Fe-18Cr Alloy," Corrossion Science, 15, 589-590, (1975).

[27] Tolpygo V. K. and Clarke D. R., "Surface Rumpling of a (Ni,Pt)Al Bond Coat Induced by Cyclic Oxidation," Acta Materialia, 48, 3283-3293, (2000)

[28] Caplan D. and Sproule G. I., "Effect of Oxide Grain Structure on the High-Temperature Oxidation of Cr," Oxidation of Metals, 9, 459-472, (1975).

[29] Hancock P. and Hurst R. C., "The Mechanical Properties and Breakdown of Surface Oxide Films at Elevated Temperatures," Eds. Staehle, R. W. and Fontana, M. G., Plenum Press, New York, (1974).

[30] Oxx G. D., Prod. Eng., 29, 61, (1958).

[31] Sarioglu C., Ph.D. Thesis, University of Pittsburgh, (1998).

[32] Tolpygo V. K. and Clarke D. R., "Tensile cracking during thermal cycling of alumina films formed by high-temperature oxidation, "Acta Materialia, 47, 3589-3605, (1999)

[33] Ashary A. A., Ph.D. Thesis, University of Pittsburgh, (1985).

[34] Johnson C. A., Rudd J. A., Bruce R. and Wortman D., "Relationship between Residual Stress, Microstructure and Mechanical Properties of Electron Beam-Physical Vapor Deposition Thermal Barrier Coatings," Surface and Coating Technologies, 108-109, 80-85, (1998).

[35] Schutze M., "Mechanical Properties of Oxide Scales," Oxidation of Metals, 44, 29-61, (1995).

[36] Nagle M. M., Evans W. T., Saunders S. R. J., and Hall D. J., "Investigation of Failure of Brittle Layers under Compressive Stresses using Acoustic Emission," Materials Science and Technology, 8, 1043-1049, (1992).

[37] Drory M. D. and Hutchinson J. W., "Measurement of the Adhesion of a Brittle Film on a Ductile Substrate by Indetation," Proc. R. Soc. Lond., 452, 2319-2341, (1996).

[38] Handoko R. A., Beuth J. L., Meier G. H., Pettit F. S. and Stiger M. J., "Mechanisms for Interfacial Toughness Loss in Thermal Barrier Coating Systems," Key Engineering Materials, 197, 165-183, (2001).

[39] Lipkin D. M. and Clarke D. R., “Measurement of the Stress IN Oxide Scales Formed by Oxidation of Alumina Forming Alloys,” Oxidation of Metals, 45, 267-281, (1996).

[40] Delaunay D., Huntz A. M. and Lacombe P., "Mechanical stresses Developed in High Temperature Resistant Alloys During Isothermal and Cyclic Oxidation Treatments: the Influence of Yttrium Additions on Oxide Scale Adherence," Corrosion Science, 20, 1109-1117, (1980).

[41] Saunders S. R. J., Evans H. E., Li M.,Gohil D. D. and Osgerby S., "Oxidation Growth Stresses in an Alumina-Forming Ferritic Steel Measured by Creep Deflection," Oxidation of Metals, 48, 189-200, (1997).

[42] Sarioglu C., Blachere J. R., Pettit F. S. and Meier G. H., “Room Temperature and In-Situ High Temperature Strain or Stress Measurements by XRD Techniques,” Microscopy of Oxidation, 3, 41-51, (1997).

[43] Messoudi K., Huntz A.M. and Di Menza L., “Residual Stresses in Alumina Scales. Experiments, Modeling and Stress-Relaxation Phenomena,” Oxidation of Metals, 53, 49-75, (2000).

[44] Lowell E. L. and Smialek J. L. and Barrett, C. A., “Cyclic Oxidation of Superalloys High Temperature Corrosion Proceedings 1981, Ed. Rapp R. A., NACE, 219-226, (1983).

[45] Lowell C. E., Barrett C. A., Palmer R. W., Auping J. V. and Probst H. B., “COSP: A Computer Model of Cyclic Oxidation,” Oxidation of Metals, 36, 81-112, (1991).

[46] Smialek J. L. and Auping J. V., “COSP for Windows:Strategies for a Rapid Analysis of Cyclic Oxidation Behavior,” Oxidation of Metals, 57, 559-581, (2002).

[47] Smialek J. L., “A Deterministic Interfacial Cyclic Oxidation Spalling Model,” Acta Materialia, 51, 469-483, (2003).

[48] Poquillon D. and Monceau D., “Applicaiton of a Simple Statistical Spalling Model for the Analysis of High Temperature, Cyclic Oxidation Kinetics Data,” Oxidation of Metals, 59, 409-431, (2003).

[49] Nesbett A. N. and Lowell C. E., "Prediction of the High Temperature Oxidative Life of Intermetallics," Mat. Res. Soc. Symp. Proc., 288, 107-119, (1993).

[50] Smialek J L., "Oxide Morphology and Spalling Model for NiAl," Metallurgical Transactions, 9A, 309-320, (1978).

[51] Barret C. A., "The Effect of 0.1 Atomic Percent Zirconium on the Cyclic Oxidation Behavior of b-NiAl for 3000 hours at 1200°C," Oxidation of High Temperature Intermetallics, Eds. Grobstein T. and Doychak J., TMS, 67-81, (1989).

[52] Goedjen J. G. and Shores D. A., " The Effect of Alloy Grain Size on the transient Oxidation Behavior of an Alumina-Forming Alloy," Oxidation of Metals, 37, 125-142, (1992).

[53] Harper M. A. and Gleeson B., "Long-Term, Cyclic Oxidation Behavior of Three Chromia-Forming Alloys Exposed to Air at 982°C, Cyclic Oxidation of High Temperature Materials, Eds. Schutze M. and Quadakkers W. J., 273-286, (1999).

[54] Zhang Y. and Shores D. A., "Study of Cracking and Spalling of Cr2O3 Scale Formed on Ni-30Cr Alloy," Oxidation of Metals, 40, 529-553, (1993).

[55] Schmutzler H. J. and Grabke H. J., "Application of an Acoustic-Emission Technique to the High-Temperature Oxidation of Fe-Cr-Al Alloys," Oxidation of Metals, 39, 15-29, (1993).

[56] Smialek, J. l. and Morscher G. N., "Delayed Alumina Scale Spallation on Rene N5+Y: Moisture Effects and Acoustic Emission," Mat. Sci. and Eng. A, A332, 11-24, (2001).

[57] Udias, A, "Principles of Seismology," New York, Cambridge University Press, (1999).

[58] Nye J. F., "Physical Properties of Crystals, Their Representation by Tensors and Matrices," Clarendon Press, Oxford, (1985).

[59] Heiple C. R., Carpenter S. H. and Christiansen S. S., "A Calibration Source for Acoustic Emission Analysis," Acoustic Emission: Current Practice and Future Directions, ASTM STP, Eds. Sachse W., Roget J. and Yamaguchi K., Am. Soc. for Testing and Materials, Philadelphia, 1077, 77-85, (1991).

[60] Landis E. N. And Baillon L., "Experiments to Relate Acoustic Emission Energy to Fracture Energy of Concrete," J. of Engineering Mechanics, 128, 698-702, (2001).

[61] Noyan I. C. and Cohen J.B., "Residual Stress, Measurement by Diffraction and Interpretation,"Springer-Verlag, Berlin, (1987).

[62] Evenschor P. D., Frohlich W. and Hauk V., "Berechnung der rontgenographischen Elastizitatskonstanten aus den Einkristallkoeffizienten hexagonal kristallisierender Metalle," Z. Metallde., 62, 38-42, (1971).

[63] Goto T. and Anderson O. L., "Elastic Constants of Corundum up to 1825K," J. of Geophysical Research, 94, 7588-7602, (1989).

[64] Messaoudi K., Huntz A. M. and Di Menza L., "Residual Stresses in Alumina Scales. Experiments, Modeling, and Stress-Relaxation Phenomena," Oxidation of Metals, 53, 49-75, (2000).

[65] Brinksmeier E. and Siemer H., "Calculation of X-ray Elastic Constants of Alumina Oxide Ceramic," 2nd International Conference on Residual Stress, Narcy, 335-340, (1988).

[66] Kocks U. F., Tome, C. N. and Wenk H. R., "Texture and Anisotropy: Preferred Orientations in Polycrystals and Their Effects on Materials Properties," Cambridge University Press, Cambridge, (1998).

[67] Schulz L. G., " A Direct Method of Determining Preferred Orientation if a Flat Reflection Sample Using a Geiger Counter X-ray Spectrometer," Journal of Applied Physics, 20, 1030-1033, (1949).

[68] C. Sarioglu, M. J. Stiger, J. R. Blacher, R. Janakiraman, E. Schumann, A. Ashary, F. S. Pettit and G. H. Meier, "The Adhesion of Alumina Films to Metallic Alloys and Coatings," Materials and Corrosion, 51, 1-15, (2000).

[69] Stasik M. C., Pettit F. S. and Meier G. H., "Effects of Reactive Element Additions and Sulfur Removal on the Oxidation Behavior of FeCrAl Alloys," Scripta Metallurgica et Materialia, 31, 1645-1650, (1994).

[70] Giggins C. S. and Pettit F. S., "Oxidation of Ni-Cr-Al Alloys Between 1000° and 1200°C," J. Electrochem. Soc., 118, 1782-1790, (1971).

[71] Grabke H. J., "Oxidation of NiAl and FeAl," Intermetallics, 7, 1153-1158, (1999).

[72] Blachere J. R.; Schumann E.; Meier G. H.; and Pettit F. S., "Textures of alumina scales on FeCrAl alloys," Scripta Materialia, 49, 909-912, (2003).

[73] Watchman J. B. and Lam D. G., "Young's Modulus of Various Refractory Materials as a Function of Temperature," J. of American Ceramic Society, 42, 254-260, (1959).

[74] Schutze M., "Mechanical Properties of Oxide Scales," Oxidation of Metals, 44, 29-61, (1995).

[75] Touloukia Y. S., Kirby R. K., Taylor R. E. and Lee T. Y. R., Eds., "Thermophysical Properties of Matter Volume 13: Thermal Expansion Nonmetallic Solids," Plenum Press, New York, 176-177, (1977).

[76] Bull S. J., "Modeling of Residual Stress in Oxide Scales," Oxidation of Metals, 49, 1-17, (1998).

[77] Tedmond C. S., "Oxidation of Fe-Cr Alloys," J. of Electrochemical Society, 114, No. 8, 788-795, (1967).

[78] C. Sarioglu, E. Schumnn, J. R. Blachere, F. S. Pettit and G. H. Meier, "X-ray Determination of Stresses in Alumina Scales on High Temperature Alloys," Materials at High Temperatures, 17, 109-115, (2000).

[79] Cheng J., Jordan E. H., Barber B. and Gell M., " Thermal/Residual Stress in an Electron Beam Physical Vapor Deposited Thermal Barrier Coating System," Acta Materialia, 46, 5839-5850, (1998).

[80] Lance M., Oak Ridge National Laboratory, Private Communication, (2003).

[81] Serruys W., Langouche F., Van Houtte P. and Aernoudt, E., " Calculation of X-ray Elastic Constants in Isotropic nad Textured Materials," International Conference on Residual Stresses, Eds. Beck G., Denis S. and Simon A., Elsevier Applied Science, London, 166-171, (1989).

[82] Nychka J., Univesity of California Santa Barbara, Private Communication, (2002).

[83] Felten E. J. and Pettit F. S., "Developmet, Gowth, and Adhesion of Al2O3 on Platinum-Aluminum Alloys," Oxidation of Metals, 10, 189-223, (1976).

[84] Schumann E., Sarioglu C., Blachere J. R., Pettit F. S. and Meier G. H., "High-Temperature Stress Measurements During the Oxidation of NiAl," Oxidation of Metals, 53, 259-272, (2000).